Flower/FLWR-1 regulates neuronal activity *via* the plasma membrane Ca^{2+}-ATPase to promote recycling of synaptic vesicles

Marius Seidenthal[1,2], Jasmina Redzovic[1,2,3,4], Jana F. Liewald[1,2,4], Dennis Rentsch[1,2], Stepan Shapiguzov[1,2], Noah Schuh[1,2], Nils Rosenkranz[1,2], Stefan Eimer[3], Alexander Gottschalk[*,1,2]

1 Buchmann Institute for Molecular Life Sciences, Goethe-University, Max-von-Laue-Strasse 15, 60438 Frankfurt am Main, Germany
2 Institute for Biophysical Chemistry, Department of Biochemistry, Chemistry, and Pharmacy, Goethe-University, Max-von-Laue-Strasse 9, 60438 Frankfurt am Main, Germany
3 Institute of Cell Biology and Neuroscience, Goethe-University, Max-von-Laue-Strasse 13, 60438 Frankfurt am Main, Germany
4 Contributed equally
* to whom correspondence should be addressed: a.gottschalk@em.uni-frankfurt.de

Keywords: neurotransmission, synaptic vesicles, exo-endocytosis coupling, *Caenorhabditis elegans*, synaptic plasticity, excitation-inhibition imbalance, plasma membrane Ca^{2+}-ATPase

Abstract

The Flower protein was suggested to couple the fusion of synaptic vesicles (SVs) to their recycling in different model organisms. It is supposed to trigger activity-dependent bulk endocytosis by conducting Ca^{2+} at endocytic sites. However, this mode of action is debated. Here, we investigated the role of the *Caenorhabditis elegans* homolog FLWR-1 in neurotransmission. Our results confirm that FLWR-1 facilitates the recycling of SVs at the neuromuscular junction (NMJ). Ultrastructural analysis of synaptic boutons after hyperstimulation revealed an accumulation of large endocytic structures in *flwr-1* mutants. These findings do not support a role of FLWR-1 in the formation of bulk endosomes but rather a function in their breakdown. Unexpectedly, loss of FLWR-1 led to increased neuronal Ca^{2+} levels in axon terminals during stimulation, particularly in GABAergic motor neurons, causing excitation-inhibition imbalance. We found that this increased NMJ transmission might be caused by deregulation of MCA-3, the nematode orthologue of the plasma membrane Ca^{2+} ATPase (PMCA). *In vivo* molecular interactions indicated that FLWR-1 may be a positive regulator of the PMCA and might influence its recycling through modification of plasma membrane levels of $PI(4,5)P_2$.

Introduction

Chemical synaptic transmission involves a cycle of biogenesis of synaptic vesicles (SVs), their fusion with the plasma membrane (PM), as well as their recycling by endocytosis and de novo formation in the endosome (Alabi and Tsien, 2012; Chanaday et al., 2019; Kononenko and Haucke, 2015; Rizzoli, 2014; Saheki and De Camilli, 2012). Coupling of SV exocytosis and endocytosis must be tightly controlled to avoid depletion of the reserve pool of SVs and to enable sustained neurotransmission (Haucke et al., 2011; Lou, 2018). Different hypotheses have been formulated as to how this is achieved within neurons. One hypothesis suggests that an SV-integral transmembrane protein called Flower could form ion channels that get inserted into the PM during SV fusion (Yao et al., 2009). Subsequently, Flower may facilitate endocytosis by conducting Ca^{2+} into the cytoplasm, thus contributing to defining endocytic sites (Yao et al., 2017). In *Drosophila melanogaster*, Flower was proposed to increase phosphatidylinositol-4,5-bisphosphate ($PI(4,5)P_2$) levels through Ca^{2+} microdomains, which was suggested to drive activity-dependent bulk endocytosis (ADBE) and formation of new SVs after prolonged, intense neurotransmission (Li et al., 2020). The hypothesis that Flower may have Ca^{2+} channel activity was further proposed based on sequence similarities between Flower and the Ca^{2+} selectivity filter of voltage-gated Ca^{2+} channels (VGCCs; Yao et al. (2009). Additional evidence from *Drosophila* suggests that Flower may regulate clathrin-mediated endocytosis (CME) in a Ca^{2+} independent fashion (Yao et al., 2017). However, while a facilitatory

role of Flower in endocytosis appears to be evolutionarily conserved, and was observed in different organisms and tissues, including non-neuronal cells (Chang et al., 2018; Rudd et al., 2023; Yao et al., 2017), its Ca^{2+} channel activity and its influence on SV recycling is debated (Coelho and Moreno, 2020; Lou, 2018). The kinetics of Ca^{2+} influx mediated by Flower appear to be too slow and the amount conducted too low to have a major impact (Xue et al., 2012). Moreover, the function of Flower appears to depend on the cell type and the extent of synaptic activity (Chang et al., 2018; Yao et al., 2017). Apart from its role in endocytosis, Flower is involved in cell survival mechanisms during development (Coelho and Moreno, 2020; Costa-Rodrigues et al., 2021). Intriguingly, loss of the mammalian homolog of Flower can reduce tumor growth, suggesting an important function in tumor cell survival and indicating possible options for cancer treatment (Madan et al., 2019; Petrova et al., 2012). However, more research is needed to determine the exact signaling pathways by means of which Flower mediates cell survival (Costa-Rodrigues et al., 2021).

Early studies of the Flower protein proposed a two- or three-transmembrane helical organization in which the C-terminus is exposed to the extracellular space and may thus mediate intercellular communication (Costa-Rodrigues et al., 2021; Rhiner et al., 2010). However, more recent research has shown that both N- and C-termini of Flower are likely cytosolic, and that the longest mammalian isoform consists of four transmembrane helices which are connected by short loops (Chang et al., 2018; Rudd et al., 2023). The genome of the nematode *Caenorhabditis elegans* is predicted to contain only a single isoform of Flower (FLWR-1; *wormbase.org*). *C. elegans* therefore may serve as an excellent model organism to further investigate the evolutionarily conserved role of Flower in neurotransmission and endocytosis. Here, we studied the function of *C. elegans* FLWR-1. We find that FLWR-1 localizes to SVs and to the PM and is involved in neurotransmission. We further show that FLWR-1 has a facilitatory but not essential role in endocytosis, confirming previous research in *Drosophila* and mammalian cells. Loss of FLWR-1 surprisingly conveys increased Ca^{2+} influx in optogenetically depolarized motor neurons. Yet, this is accompanied by reduced neurotransmitter release based on pharmacological assays and following optogentic stimulation, thus suggesting a deregulation of Ca^{2+} signaling in the presynapse. This is associated with defective SV recycling at the level of the endosome and thus reduced SV numbers upon sustained stimulation. The increased Ca^{2+} influx is more pronounced in γ-aminobutyric acid (GABA) releasing neurons and leads to an excitation-inhibition (E/I) imbalance at the neuromuscular junction (NMJ) through increased release of the neurotransmitter GABA. A function of FLWR-1 in endocytosis appears to affect also the plasma membrane Ca^{2+}-ATPase MCA-3, required for extrusion of Ca^{2+} from the cytosol. This may explain the increased Ca^{2+} levels during stimulation in *flwr-1* mutant neurons. Last, our findings suggest a possible direct molecular interaction between FLWR-1 and MCA-3.

Materials and methods

Molecular biology

For Plasmids used in this paper and details of their generation, see **Table S1**. **pZIM902** [punc-17b::GCaMP6fOpt] was a gift from Manuel Zimmer. **p1676** [punc-17(short)::TagRFP::ELKS-1] was kindly provided by the lab of Zhao-Wen Wang. **pJH2523** [punc-25::GCaMP3::UrSL2::wCherry] was a gift from Mei Zhen (Addgene plasmid # 191358 ; http://n2t.net/addgene:191358 ; RRID:Addgene_191358) (Lu et al., 2022).

Cultivation of *C. elegans*

Animals were kept at 20 °C on nematode growth medium (NGM) plates seeded with OP50-1 bacteria (Brenner, 1974). For optogenetic experiments, OP50-1 was supplemented with 200 µM all-*trans* retinal (ATR) prior to seeding and animals were kept in darkness. Transgenic animals carrying extrachromosomal arrays were generated by microinjection into the gonads (Fire, 1986). L4 staged larvae were picked ~18 h before experiments and tested on at least three separate

days with animals picked from different populations. Transgenic animals were selected by fluorescent markers using a Leica MZ16F dissection stereo microscope. Integration of the *sybIs8965* transgenic array (PHX8965 strain) was performed by SunyBiotech. The RB2305 strain containing the *flwr-1(ok3128)* allele was outcrossed three times to N2 wild type. For an overview of strains, genotypes and transgenes, see **Table S2**.

Counting live progeny

To count living progeny per animal, five L4 larvae were singled onto NGM plates seeded with 50 µl OP50-1. Animals were then picked onto fresh plates after two days and on each of the following two days and removed on day five. Living progeny per animal were counted after reaching adulthood and summed up over the three plates on which each parental animal laid eggs, respectively. Experiments were performed blinded to the genotype.

Pharmacological assays

1.5 mM aldicarb and 0.25 mM levamisole plates were prepared by adding the compounds to liquid NGM prior to plate pouring (Mahoney et al., 2006). Aldicarb (Sigma Aldrich, USA) was kept as a 100 mM stock solution in 70 % ethanol. Levamisole (Sigma Aldrich, USA) was stored as a 200 mM solution dissolved in ddH_2O. 12 - 30 young adult animals were transferred to each plate and tested every 15 (levamisole) or 30 (aldicarb) minutes. Assays were performed blinded to the genotype and control groups (wild type and *flwr-1* mutants), measured in parallel on the same day. Animals that did not respond after being prodded three times with a hair pick were counted as paralyzed. Worms that crawled of the plate were disregarded from analysis.

Measurement of swimming cycles and crawling speed using the multi-worm-tracker (MWT)

Swimming cycles were measured as described previously (Vettkotter et al., 2022). In short, worms were washed three times with M9 buffer to remove OP50 and transferred onto 3.5 cm NGM plates with 800 µl M9. Animals were visualized using the multiworm tracker (MWT) platform (Swierczek et al., 2011) equipped with a Falcon 4M30 camera (DALSA). Channelrhodopsin-2 (ChR2) was stimulated with 470 nm light at 1 mW/mm^2 intensity for 90 s. 30 s videos were captured and thrashing was analyzed using the "wrmTrck" plugin for ImageJ (Nussbaum-Krammer et al., 2015). The automatically generated tracks were validated using a custom written Python script (https://github.com/dvettkoe/SwimmingTracksProcessing). Crawling speed was measured with the same setup and as described before (Vettkotter et al., 2022) yet animals were transferred to empty, unseeded NGM plates after washing. Prior to the measurement, animals were incubated in darkness for 15 min which is necessary for a switch from local to global search for food and thus a constant crawling speed (Calhoun et al., 2014). The crawling speed was recorded with the "Multi-Worm Tracker" software and extracted using the "Choreography" software (Swierczek et al., 2011). A custom-written Python script was used to summarize the measured tracks (https://github.com/dvettkoe/MWT_Analysis).

For manual counting of swimming cycles (**Figure 9 – Figure supplement 1**), animals were transferred on an NGM plate in M9 buffer, and filmed with a Canon Powershot G11 camera, for 30 sec. Swimming cycles were counted manually during replay of the video.

Measurement of body length

Body length was measured as described previously (Liewald et al., 2008; Seidenthal et al., 2022). In short, single animals were transferred onto unseeded NGM plates and illuminated with light from a 50 W HBO lamp which was filtered with a 450 - 490 nm bandpass excitation filter. ChR2 was stimulated with 100 $\mu W/mm^2$ light intensity. A 665 - 715 nm filter was used to avoid unwanted activation by brightfield light. Body length was analyzed using the "WormRuler" software (version 1.3.0) and normalized for the average skeleton length before stimulation (Seidenthal et al., 2022). Values deviating more than 20 % from the initial body length were discarded as they result from artifacts in the background correction (and are biomechanically impossible). Basal body length was calculated from the skeleton length in pixels which is generated by the WormRuler software. This was converted to mm and averaged for each animal over a duration of five seconds.

Light microscopy and fluorescence quantification

Animals were placed upon 7 % agarose pads in M9 buffer. Worms were immobilized by either using 20 mM levamisole in M9 or Polybead polystyrene microspheres (Polysciences) for experiments involving GABAergic stimulation. For optogenetic experiments, single animals were placed upon pads to avoid unwanted pre-activation of channelrhodopsins.

Imaging was performed using a Axio Observer Z1 microscope (Zeiss, Germany). Proteins were excited using 460 nm and 590 nm LEDs (Lumen 100, Prior Scientific, UK) coupled via a beamsplitter. Background correction was conducted by placing a region of interest (ROI) within the animal yet avoiding autofluorescence.

GCaMP and pHluorin imaging and ChrimsonSA stimulation was performed using a 605 nm beamsplitter (AHF Analysentechnik, Germany) which was combined with a double band pass filter (460 - 500 and 570 - 600 nm). A single bandpass emission filter was used (502.5 - 537.5 nm). pOpsicle assays were performed as described previously using a 100x objective (Seidenthal et al., 2023). We extended the ChrimsonSA stimulation light pulse to 30 s to be consistent with the stimulus length of electron microscopy (EM) and electrophysiology experiments. Moreover, 2 x 2 binning was applied. Image sequences with 200 ms light exposure (5 frames per second) were acquired with an sCMOS camera (Kinetix 22, Teledyne Photometrics, USA). Video acquisition was controlled using the µManager v.1.4.22 software (Edelstein et al., 2014). The timing of LED activation was managed using a *Autohotkey* script. Dorsal nerve cord (DNC) fluorescence was quantified with ImageJ by placing a ROI with the *Segmented Line* tool. XY-drift was corrected using the *Template Matching* plugin if necessary. Animals showing excessive z-drift were discarded. A custom written python script was used to summarize background subtraction and normalization to the average fluorescence before pulse start (https://github.com/MariusSeidenthal/pHluorin_Imaging_Analysis).

GCaMP imaging was conducted similarly with the same setup and light intensity for ChrimsonSA stimulation (40 $\mu W/mm^2$) yet without binning. GCaMP fluorescence was quantified by placing ROIs around four synaptic puncta. Puncta fluorescence was averaged prior to background correction and normalization. Moreover, the bleach correction function of the python script was used which corrects fluorescence traces with strong bleaching. Strong bleaching is defined as the fluorescence intensity of the mean of the last second of measurement being less than 85% of the first second. The script performs linear regression analysis for DNC fluorescent traces and background ROI and corrects values prior to background correction. The increase in GCaMP fluorescence during stimulation was highly dependent on basal fluorescence values before stimulation and transient Ca^{2+} signals. This caused some measurements to show very strong increases in fluorescence. To avoid distortion of statistical analyses, we performed outlier detection for the increase during stimulation on all datasets with the Graphpad Prism 9.4.1 Iterative Grubb's method. The alpha value (false discovery rate) was set to 0.01.

For pOpsicle assays, animals were assessed for whether they exhibited a significant increase in fluorescence during stimulation, which was necessary for analysis of fluorescence decay after stimulation. A strong signal was determined as the maximum background corrected fluorescence during the light pulse (moving average of 5 frames) being larger than the average before stimulation plus 3x the standard deviation of the background corrected fluorescence before stimulation. Regression analysis of pHluorin fluorescence decay was performed as described previously by using Graphpad Prism 9.4.1 and fitting a "Plateau followed one-phase exponential decay" fit beginning with the first time point after stimulation to single measurements (Seidenthal et al., 2023). Animals that displayed no increase during stimulation as well as animals showing no decay or spontaneous signals after stimulation were discarded from analysis.

Comparison of dorsal and ventral (VNC) nerve cord fluorescence of GFP::FLWR-1 and mCherry::SNB-1 was conducted by imaging the posterior part of the animal where an abundance of synapses can be found. Images were acquired using the same beamsplitter and excitation filter as used for pOpsicle experiments but equipped with a 500 – 540 nm/600 – 665 nm double bandpass emission filter (AHF Analysentechnik, Germany) and 2 x 2 binning. The Arduino script "AOTFcontroller" was used to control synchronized 2-color illumination (Aoki et al., 2024). VNC and DNC fluorescence were analyzed by choosing single frames from acquired z-stacks in which nerve cords were well focused. Fluorescence intensities were quantified by placing a *Segmented Line* ROI. Kymographs were generated with the ImageJ *Multi Kymograph* function.

Confocal laser scanning microscopy was performed on a LSM 780 microscope (Zeiss, Germany) equipped with a Plan-Apochromat 63-x oil objective. The Zeiss Zen (blue edition) *Tile Scan* and *Z-Stack* functions were used to generate overview images of animals expressing GFP::FLWR-1. Images were processed and maximum z-projection performed using ImageJ. Colocalization analysis was performed by placing a *Segmented Line* ROI onto the DNC and plotting the fluorescence profile along the selected ROI for both color channels. Correlation of fluorescence intensities was then conducted using the GraphPad Prism 9.4.1 Pearson correlation function.

Fluorescence of GFP within coelomocytes (CCs) was visualized with a 100-x objective. An eGFP filter cube (AHF Analysentechnik, Germany) was used and fluorescence was excited with the 460 nm LED. Images were acquired using 2 x 2 binning and 50 ms exposure for ssGFP and 200 ms for GFP fused to the PH-domain. Endocytosed ssGFP fluorescence was quantified by drawing a ROI around all CCs found within any worm imaged using the *Freehand*

selections tool and performing background correction. CC fluorescence was then normalized to the average fluorescence in wild type animals on the respective measurement day and CC location (anterior/middle/posterior). This was necessary since anterior CCs generally had a higher fluorescence than those in other locations. Membrane localization of PH-domain GFP was determined by drawing a *Segmented Line* ROI around the perimeter of the cell and drawing a rough outline of the cell interior using the *Freehand selections* tool. Membrane fluorescence was then corrected by subtracting the measured interior fluorescence for each cell.

In BiFC experiments, split mVenus was imaged with a 100x objective, the eGFP filter cube and 500 ms exposure. Fluorescence was excited with 460 nm.

MCA-3b::YFP was imaged with a 40-x objective, the eGFP filter cube and 200 ms exposure. Fluorescence was excited with 460 nm. Synaptic puncta towards the posterior part of the animal were imaged and quantified by drawing a *Freehand selections* ROI around all visible and well-focused synaptic puncta in an animal before averaging. Similarly, interpuncta fluorescence was quantified by drawing a ROI around several locations inbetween the examined puncta.

Primary neuronal cell culture

Primary neuronal cell cultures were generated from embryos of SNG-1::pHluorin expressing animals as described before (Seidenthal et al., 2023) yet seeded into perfusion chambers (0.4 mm channel height, ibidi). pHluorin fluorescence was excited with 460 nm and imaged using the eGFP filter cube and 1000 ms exposure time. The buffers used to quench surface and dequench intracellular pHluorin were adapted from Dittman and Kaplan (2006). Cells were washed three times with the respective buffer prior to imaging by pipetting 1 ml into the reservoir wells of the perfusion chamber and removing the same amount of liquid from the other side. Individual cells were analyzed by placing a *Segmented Line* ROI onto extending neurites and performing background correction. The fraction of SNG-1::pHluorin which resides in SVs was then estimated by dividing the fluorescence originating from vesicular pHluorin by the total fluorescence originating in unquenched pHluorin:

$$Vesicle\ fraction = \frac{F_{NH4Cl} - F_0}{F_{NH4Cl} - F_{pH=5.6}}$$

F_0 → the basal neurite fluorescence in control saline buffer

F_{NH4Cl} → neurite fluorescence during addition of a buffer containing NH_4Cl which unquenches intravesicular pHluorin

$F_{pH=5.6}$ → neurite fluorescence with surface quenched pHluorin by low pH

Electrophysiology

Electrophysiological recordings of body wall muscle cells (BWMs) were performed in dissected adult worms as previously described (Liewald et al., 2008). Animals were immobilized with Histoacryl L glue (B. Braun Surgical, Spain) and a lateral incision was made to access NMJs along the anterior VNC. The basement membrane overlying BWMs was enzymatically removed by 0.5 mg/ml collagenase for 10 s (C5138, Sigma-Aldrich, Germany). Integrity of BWMs and nerve cord was visually examined via DIC microscopy.

Recordings from BWMs were acquired in whole-cell patch-clamp mode at 20-22 °C using an EPC-10 amplifier equipped with Patchmaster software (HEKA, Germany). The head stage was connected to a standard HEKA pipette holder for fire-polished borosilicate pipettes (1B100F-4, Worcester Polytechnic Institute, USA) of 4–10 MΩ resistance. The extracellular bath solution consisted of 150 mM NaCl, 5 mM KCl, 5 mM $CaCl_2$,1 mM $MgCl_2$,10 mM glucose, 5 mM sucrose, and 15 mM HEPES, pH 7.3, with NaOH, ~330 mOsm. The internal/patch pipette solution consisted of 115 mM K-gluconate, 25 mM KCl, 0.1 mM $CaCl_2$, 5 mM $MgCl_2$, 1 mM BAPTA, 10 mM HEPES, 5 mM Na_2ATP, 0.5 mM Na_2GTP, 0.5 mM cAMP, and 0.5 mM cGMP, pH 7.2, with KOH, ~320 mOsm.

Voltage clamp experiments were conducted at a holding potential of −60 mV. Light activation was performed using an LED lamp (KSL-70, Rapp OptoElectronic, Hamburg, Germany; 470 nm, 8 mW/mm²) and controlled by the Patchmaster software. Subsequent analysis was performed using Patchmaster and Origin (Originlabs). Analysis of mPSCs was conducted with MiniAnalysis (Synaptosoft, Decatur, GA, USA, version 6.0.7) and rate and amplitude of mPSCs were

analyzed in 1 s bins. Exponential decay of mPSCs during stimulation was calculated with Graphpad Prism 9.4.1 by fitting a one-phase exponential decay beginning with the first time point during stimulation.

Transmission electron microscopy

Prior to high-pressure freezing (HPF), L4 animals were transferred to freshly seeded *E. coli* OP50-1 dishes supplemented with or without 0.1 mM ATR. HPF fixation was performed on young adult animals as described previously (Kittelmann et al., 2013b; Weimer, 2006). Briefly, 20 - 40 animals were transferred into a 100 µm deep aluminum planchette (Microscopy Services) filled with *E. coli* (supplemented with or without ATR, respectively), covered with a sapphire disk (0.16 mm) and a spacer ring (0.4 mm; engineering office M. Wohlwend) for photostimulation. To prevent pre-activation of ChR2, all preparations were carried out under red light. Animals were continuously illuminated for 30 s with a laser (470 nm, ~20 mW/mm²) followed 5 s later by HPF at -180 °C under 2100 bar pressure in an HPM100 (Leica Microsystems). Frozen specimens were transferred under liquid nitrogen into a Reichert AFS machine (Leica Microsystems) for freeze substitution.

Samples were incubated with tannic acid (0.1% in dry acetone) fixative at -90 °C for 100 h. Afterward, a process of washing was performed for substitution with acetone, followed by incubation of the samples in 2% OsO_4 (in dry acetone) for 39.5 h while the temperature was slowly increased up to room temperature. Subsequently, samples were embedded in epoxy resin (Agar Scientific, AGAR 100 Premix kit – hard) by increasing epoxy resin concentrations from 50% to 90% at room temperature and 100% at 60 °C for 48 h.

Electron micrographs of 2 – 5 individual animals, and from 12 – 22 synapses per treatment, were acquired by cutting cross sections at a thickness of 40 nm, transferring cross sections to formvar- or pioloform covered copper slot grids. Specimens were counterstained in 2.5% aqueous uranyl acetate for 4 min, followed by washing with distilled water, and incubation in Reynolds lead citrate solution for 2 min in a CO_2-free chamber with subsequent washing steps in distilled water.

VNC regions were then imaged with a Zeiss 900 TEM, operated at 80 kV, with a Troendle 2K camera. Images were scored and tagged blind in ImageJ (version 1.53c, National Institute of Health) as described previously, and analyzed using SynapsEM (Vettkotter et al., 2022; Watanabe et al., 2020). Since the number of synaptic organelles varied between synapses of different sizes, their counts were normalized to the average synaptic profile area of 145,253 nm^2. Large vesicles (LVs) are defined by their size larger than 50 nm and empty lumen as described by (Kittelmann et al., 2013b), endosomes are defined as structures larger than 100 nm and located more than 50 nm away from the dense projection, as described by (Watanabe et al., 2014); however, by an alternative definition of endosome, structures with sizes larger than SVs and DCVs, with an electron dense lumen were also included (Kittelmann et al., 2013b).

Protein alignment and structure prediction

Protein alignment was performed with ClustalX (Larkin et al., 2007) and shading of conserved residues created with Boxshade (*https://junli.netlify.app/apps/boxshade/*). Transmembrane domains as well as membrane orientation were predicted by entering the predicted amino acid sequence to DeepTMHMM (Hallgren et al., 2022). FLWR-1 structure was modeled and visualized with Alphafold3 (AF3) (Abramson et al., 2024). FLWR-1 tetramers have been modeled using AlphafoldMultimer or AF3 (Evans et al., 2022). Protein structures were analyzed and edited using PyMol v2.5.2. Docking of $PI(4,5)P_2$ to the FLWR-1 AF3 model was conducted in PyMol using the DockingPie plugin running the Autodock/Vina analysis (Eberhardt et al., 2021; Rosignoli and Paiardini, 2022).

Statistical Analysis and generation of graphs

Graphs were created and statistical analyses were performed using GraphPad Prism 9.4.1. Data was displayed as mean ± standard error of the mean (SEM) unless noted otherwise. Unpaired t-tests were used to compare two datasets and one-way ANOVAs or two-way ANOVAs if three or more datasets were assessed, according to the number of tested conditions. Fitting of a mixed-effects model was used instead of two-way ANOVA if the number of data points was not constant between different datasets for example if the number of animals differed between time points. Mann-Whitney tests were performed if two datasets were compared that were not normally distributed and datasets were depicted as median with interquartile range (IQR) in statistical analyses. Kruskal-Wallis tests were conducted if not normally distributed datasets were assessed. Iterative Grubb's outlier detection was used when required and as indicated. The alpha value (false discovery rate) was set to 0.01. Representations of the exon-intron structures of genes were created using the "Exon-Intron Graphic Maker" (Bhatla, 2012).

Results

FLWR-1 is involved in neurotransmission

The amino acid sequence of *C. elegans* FLWR-1 is conserved with its *D. melanogaster* (Fwe-Ubi) and *Homo sapiens* (hFwe4) homologues (**Fig. 1A**). Fwe-Ubi was shown to facilitate recovery of neurons following intense synaptic activity (Yao et al., 2009; Yao et al., 2017). To investigate whether this involvement of Flower in neurotransmission is evolutionarily conserved, we studied a mutant lacking most of the *flwr-1* coding region (*ok3128*, **Fig. 1B**) (Consortium, 2012). Animals lacking FLWR-1 did not display severe phenotypes. Basal locomotion in liquid (**Fig. 1C, D** seconds 0 – 30) and body length of young adults (**Figure 1 – Figure supplement 1A**) were not significantly different from the respective values of wild type animals. However, fertility appeared slightly reduced (**Figure 1 – Figure supplement 1B**). Basal crawling speed, on average, was not different between wild type, *flwr-1* mutants and rescued animals (genomic sequence and 2kB promoter; **Figure 1 – Figure supplement 1C**).

These findings indicate that FLWR-1 is unlikely to have an essential function in neurotransmission, at least not during basal *in vivo* activity, but rather a regulatory or facilitatory one. Previously we showed that mutations which only weakly affect basal locomotion can severely affect recovery of swimming speed after strong optogenetic stimulation of cholinergic neurons (Yu et al., 2018). We therefore subjected *flwr-1(ok3128)* mutants expressing channelrhodopsin-2 (ChR2; variant H134R), which were treated with the chromophore all-*trans* retinal (ATR), to blue light during swimming (Liewald et al., 2008; Nagel et al., 2005). Photostimulation resulted in a stop of all swimming during the light pulse, followed by a slow recovery in the dark. Indeed, loss of FLWR-1 led to a significantly slowed recovery of swimming locomotion (**Fig. 1C, D**). This could be fully rescued by transgenic expression of genomic *flwr-1* including a two kilobase sequence upstream of the putative start codon, hereafter called *pflwr-1* (as the promoter of *flwr-1*). To further evaluate the involvement of FLWR-1 in neurotransmission, we exposed *flwr-1* mutants to aldicarb. This acetylcholine esterase (AChE) inhibitor induces paralysis due to accumulation of ACh in the synaptic cleft (Blazie and Jin, 2018; Mahoney et al., 2006). Resistance to aldicarb indicates either reduced release or detection of ACh or, alternatively, increased inhibitory signaling (Janosi et al., 2024; Vashlishan et al., 2008). Loss of FLWR-1 led to a significant delay in paralysis indicating an involvement in transmission at the NMJ (**Fig. 1E**). Full rescue of the *flwr-1* mutant phenotypes suggests that expression from the 2 kB fragment of the endogenous promoter fully recapitulates the native expression in the context of NMJ function.

FLWR-1 is expressed in excitable cells and localizes to synaptic vesicles

Invertebrate and vertebrate homologues of FLWR-1 are predicted to be membrane proteins containing four transmembrane helices with both C- and N-termini located in the cytosol (Chang et al., 2018; Rudd et al., 2023; Yao et al., 2009). *In silico* predictions using the FLWR-1 sequence of 166 amino acids suggest evolutionary conservation of the tetraspan structure (**Figure 1 – Figure supplement 2A**) (Hallgren et al., 2022). Accordingly, Alphafold3 predicts a protein structure of FLWR-1 that implies a four helical configuration, with helix lengths that could span biological membranes, and three additional, shorter α-helices (**Figure 1 – Figure supplement 2B**) (Abramson et al., 2024). We sought to determine the cellular as well as subcellular localizations of FLWR-1 by tagging its C-terminus with GFP and expressing the construct using the endogenous promoter (**Fig. 2A – C**). Green fluorescence could be observed in developing embryos in the uterus, as well as in

various tissues including neurons, body wall and pharyngeal muscles (**Fig. 2A**). FLWR-1 localized to neurites and cell bodies of nerve ring neurons, representing the central nervous system of the nematode (**Fig. 2B**) (Ward et al., 1975). These results are in agreement with single-cell RNA-sequencing data obtained from *C. elegans* which show near ubiquitous expression of *flwr-1/F20D1.1* (**Figure 1 – Figure supplement 2C**, **Table S3**; Taylor et al. (2021)). The GFP::FLWR-1 fusion protein was functional as demonstrated by rescue of the swimming phenotype (recovery from cholinergic neuron photostimulation) observed in the *flwr-1* mutant background (**Figure 1 – Figure supplement 2D, E**).

Within muscle cells, FLWR-1 was primarily targeted to the PM (**Fig. 2C**). As its *D. melanogaster* homolog was localized to synaptic vesicles (SVs) (Yao et al., 2009), we wondered whether FLWR-1 would co-localize with known SV markers such as SNB-1 synaptobrevin-1 (Calahorro and Izquierdo, 2018; Nonet, 1999). Indeed, GFP::FLWR-1 fluorescence largely overlapped with co-expressed mCherry::SNB-1 in the dorsal nerve cord (DNC; **Fig. 2D, E**). FLWR-1 further seemed to be enriched in fluorescent puncta in DNC and sublateral nerve cords indicating synaptic localization (**Fig. 2D - F**), however it was not restricted to synaptic regions only, meaning it is likely present also in the PM. Furthermore, we observed moving particles, probably SV precursors, which contained SNB-1 and FLWR-1, travelling along commissures between ventral nerve cord (VNC) and DNC (**Fig. 2F, G** and **Movie S1**). Anterograde transport of these precursors towards synapses depends on kinesin-3/UNC-104 (Hall and Hedgecock, 1991; Klopfenstein and Vale, 2004). We used a reduction-of-function allele (*e1265*) affecting interaction of UNC-104 with its cargo to investigate whether FLWR-1 is actively transported towards synapses (Cong et al., 2021). Indeed, animals lacking functional UNC-104 showed a reduced amount of axonal GFP fluorescence in the nerve ring and DNC while cell bodies were clearly visible (**Figure 1 – Figure supplement 2F**). The ratio of DNC to VNC fluorescence was significantly decreased in *unc-104* mutants suggesting defective anterograde transport (**Fig. 2H**). Distribution of SNB-1 was similarly affected (Cuentas-Condori et al., 2023; Gally and Bessereau, 2003). Together, these results argue that FLWR-1 is expressed in neurons (as well as in muscles and other cell types) and is actively transported towards synapses.

GABAergic signaling is increased in *flwr-1* knockout mutants

Since FLWR-1 is also expressed in body wall muscles (BWMs), we wondered whether the observed aldicarb resistance originates from reduced ACh reception by ACh receptors (AChRs) (Mahoney et al., 2006). To test this, we exposed animals lacking FLWR-1 to levamisole, an AChR agonist which induces paralysis by hyperexcitation and body contraction, similar to aldicarb (Gottschalk et al., 2005; Sattelle et al., 2002). We found no significant differences in the rate of paralysis between wild type and mutant animals (**Figure 1 – Figure supplement 3A**). However, transgenic expression of FLWR-1 in BWMs partially rescued the aldicarb resistance (**Figure 1 – Figure supplement 3B**). Therefore, loss of FLWR-1 might decrease the ACh response of muscle cells, which may contribute to the aldicarb resistance of *flwr-1* mutants. However as muscles can also affect motor neurons by inhibitory retrograde signaling (Hu et al., 2012; Simon et al., 2008; Tong et al., 2017), we wanted to assess if the loss of FLWR-1 in muscle may also have effects on motor neurons. Thus, we rescued FLWR-1 in muscle and either cholinergic or GABergic neurons (**Figure 1 – Figure supplement 3B**). This did not show any additive effects to the pure neuronal rescues, thus FLWR-1 effects on muscle cell responses to cholinergic agonists must be cell-autonomous. Since muscles are activated by ACh via two different AChRs, the levamisole receptor and the nicotine-sensitive receptor (N-AChR), a homopentamer of ACR-16 subunits (Almedom et al. 2009; Richmond and Jorgensen, 1999), we addressed the possibility that FLWR-1 may regulate expression or function of N-AChRs in muscle, to affect phenotypes of aldicarb resistance. We performed aldicarb assay in the absence of

the ACR-16 (**Figure 1 – Figure supplement 3C**), which showed that the two mutations, *flwr-1(ok3128)* and *acr-16*(*ok789)*, had additive effects. Thus, FLWR-1 does not affect aldicarb resistance through downregulation of nAChRs, as otherwise the double mutant would not be more resistant than the *flwr-1* single mutant.

In addition to muscle expression, we also observed enrichment of FLWR-1 in fluorescent puncta indicating presynaptic localization (**Fig. 3A, B**). Moreover, FLWR-1 partially co-localized with the dense projection marker ELKS-1 in cholinergic, as well as in GABAergic neurons (**Fig. 3A-C**; **Figure 3 – Figure supplement 1A-C**; Dai et al. (2006); Kittelmann et al. (2013a)). Unlike ELKS-1, FLWR-1 could also be found in intersynaptic regions, though to a lesser extent than in synapses. This indicates that FLWR-1 might be involved in neurotransmission at both cholinergic and GABAergic NMJs, yet is not exclusively localized to active zones. The expression of FLWR-1 relative to ELKS-1 in either neuron type was not obviously biased to GABAergic or cholinergic neurons (**Figure 3 – Figure supplement 1A-C**). Thus, to determine whether the site of action of FLWR-1 in NMJ signaling is also evenly located to cholinergic and GABAergic neurons, we rescued FLWR-1 in each cell type of *flwr-1* mutants, using the promoters of the vesicular transporters of ACh (UNC-17) or GABA (UNC-47), respectively. Surprisingly, expression of FLWR-1 in GABAergic, but not in cholinergic neurons, rescued aldicarb resistance (**Fig. 3D**). This was unexpected, since mutations affecting SV recycling commonly lead to a slowed replenishment of SVs and thus reduced ACh release (Salcini et al., 2001; Schuske et al., 2003; Yu et al., 2018). However, our results indicate that loss of FLWR-1 leads to increased release of GABA, which counteracts the aldicarb induced paralysis (Camara et al., 2019). Additional expression of FLWR-1 in BWMs did not change these results, suggesting that its role in neurons is more crucial in affecting aldicarb sensitivity (**Figure 1 – Figure supplement 3B**). To confirm this, we crossed *flwr-1* mutants to animals lacking the vesicular GABA transporter UNC-47. This abolishes GABA release and induces hypersensitivity to aldicarb (Vashlishan et al., 2008). We observed that the additional mutation of *unc-47* led to a complete loss of aldicarb resistance in *flwr-1* mutants (**Fig. 3E**). No difference between *unc-47* and *flwr-1; unc-47* double mutants could be observed. However, as we used a high concentration of aldicarb, possible additional effects of the double mutant may have been masked. Thus, we also tested these animals at a lower concentration of aldicarb. *unc-47; flwr-1* double mutants were hypersensitive to aldicarb compared to *unc-47* single mutants, suggesting that ACh release is also increased by the loss of FLWR-1 (**Figure 1 – Figure supplement 3D**). In the absence of the compensatory increase in GABAergic signaling, this conveys aldicarb hypersensitivity. Jointly, these findings support the notion that it is primarily increased GABA signaling which is the main cause of aldicarb resistance in *flwr-1* mutants, yet neurotransmission in motor neurons may be generally upregulated.

Depolarization-induced neuronal Ca^{2+} is increased in *flwr-1* mutants

Since the release of GABA appeared to be increased in *flwr-1* mutants, we wondered whether the response of GABAergic neurons during activation was increased. To test this, the fluorescent Ca^{2+} indicator GCaMP was expressed in GABAergic neurons, allowing us to estimate relative Ca^{2+} levels at presynaptic sites (Lu et al., 2022; Nakai et al., 2001). To allow optogenetic depolarization of neurons independent of GCaMP excitation light, we co-expressed the red-shifted channelrhodopsin variant ChrimsonSA (Oda et al., 2018; Seidenthal et al., 2022). As expected, optogenetic stimulation caused an increase in GCaMP fluorescence at NMJs in the DNC (**Fig. 4A**). Comparing wild type and *flwr-1* mutants, we found that the gain in fluorescence intensity was significantly higher in animals lacking FLWR-1 (**Fig. 4A, B**), supporting our previous finding of increased neurotransmission in GABAergic neurons. To verify this at the behavioral level, we used a strain expressing

ChR2(H134R) in GABAergic neurons, as it can be used to assess GABA release through measurement of body length (Liewald et al., 2008). Since GABA receptors hyperpolarize muscle cells, optogenetic stimulation of GABAergic motor neurons causes relaxation and thus increased body length (Schultheis et al., 2011; Seidenthal et al., 2022). To augment the effect of ChR2 stimulation on body length and to observe the effect of GABA release independent of cholinergic neurotransmission, the assay was performed in a mutant background lacking the levamisole receptor (*unc-29(e1072)* mutants, affecting an essential subunit; Fleming et al. (1997); Richmond and Jorgensen (1999)). As expected, stimulation with blue light led to increased body length (**Fig. 4C**). In accordance with Ca^{2+} imaging results, *flwr-1; unc-29* double mutants showed a significantly stronger elongation during stimulation than *unc-29* mutants (**Fig. 4C, D**). These results indicate that Ca^{2+} influx into the synapse is increased, likely causing more GABA to be released in animals lacking FLWR-1. The previously observed aldicarb resistance indicates that this change in GABAergic transmission outweighs possible changes in cholinergic transmission (**Fig. 3**).

To investigate whether neuronal responses to depolarization may be generally upregulated in *flwr-1* mutants, we assessed whether evoked Ca^{2+} influx is affected in cholinergic motor neurons as well (**Fig. 4E, F**). Again, we observed increased GCaMP fluorescence levels during optogenetic stimulation. This effect could be rescued in cholinergic neurons. However, since postsynaptic muscle exerts inhibitory retrograde signaling to presynaptic cholinergic neurons (Hu et al., 2012; Simon et al., 2008; Tong et al., 2017), and because FLWR-1 is also expressed in muscle, we tested if the phenotype of the loss of FLWR-1 in cholinergic neurons would be affected by rescuing FLWR-1 in muscle. This was not the case (**Fig. 4E, F**). Together, these results indicate that loss of FLWR-1 conveys an upregulation of neuronal Ca^{2+} influx during continuous stimulation in both classes of motor neurons (**Fig. 4G**). However, the overall E/I balance appears to be shifted towards stronger inhibition of BWMs.

Endocytosis is slowed in *flwr-1* mutants in non-neuronal cells and neurons

Homologues of FLWR-1 were implicated in endocytosis in neurons as well as in non-neuronal cells (Chang et al., 2018; Rudd et al., 2023; Yao et al., 2009). We thus wondered whether this function is evolutionarily conserved in nematodes. One possibility to assess this in *C. elegans* is to observe endocytosis in coelomocytes (CCs; (Fares and Greenwald, 2001). These scavenger cells continuously endocytose fluid from the body cavity and loss of endocytosis-associated factors affects uptake of proteins secreted from other tissues (Fares and Grant, 2002). GFP fused to a secretory signal sequence is discharged from BWMs, and its endocytic uptake by CCs can be quantified by fluorescence microscopy (Bednarek et al., 2007; Fares and Greenwald, 2001). According to single-cell RNAseq data, FLWR-1 is expressed in CCs (**Table S3**; Taylor et al. (2021). Indeed, mutation of *flwr-1* led to strongly reduced GFP fluorescence levels within CCs indicating a reduced uptake by endocytosis (**Fig. 5A, B**). This defect could be cell-autonomously rescued by expressing FLWR-1 in CCs from the *unc-122* promoter. Furthermore, to assess recycling of SVs, we used the pOpsicle (pH-sensitive optogenetic reporter of synaptic vesicle recycling) assay we recently established (Seidenthal et al., 2023) to estimate the amount of SV fusion and the rate of recycling of SV components in cholinergic neurons. This assay combines a pHluorin based probe fused to an SV-associated protein (SNG-1) and optogenetic stimulation of neurotransmitter release; this way, pHluorin fluorescence is unquenched during stimulated exocytosis and quenched during SV endocytosis and recycling (Sankaranarayanan et al., 2000). Since in this assay signals originating from SVs and from the PM contribute to the overall signal, and since FLWR-1 has an effect on endocytosis, we needed to verify that the relative localization of the SNG-1::pHluorin sensor itself was not affected by the *flwr-1* mutation. Basal fluorescence, before stimulation, was unaltered in *flwr-1* mutants, showing that there

is no FLWR-1 dependent alteration of SNG-1::pHluorin in cellular membranes (**Figure 4 – Figure supplement 1A**). In addition, to estimate the amount of the sensor present in the PM vs. in vesicles, we used primary culture of *C. elegans* cells. Cholinergic neurons expressing SNG-1::pHluorin were imaged and exposed to different pH by adding a buffer of pH 5.6, or by adding ammonium chloride buffer of physiological / neutral pH, which can penetrate the cell and thus shows the maximum achievable signal, i.e. all unquenched pHluorin signal present in the cell. This showed that the amount of SNG-1::pHluorin present in SVs was also not affected by the *flwr-1* mutation (**Figure 4 – Figure supplement 1B, C**). *In vivo*, loss of FLWR-1 led to significantly increased fluorescence signals during stimulation which indicates more SV fusion compared to wild type (**Fig. 5C, E**). This is in accordance with the increased responses of cholinergic neurons to depolarization we observed earlier (**Fig. 4E, F**). Moreover, the rate of fluorescence decay after stimulation was significantly reduced in *flwr-1* mutants suggesting slower recycling of SVs, or reduced acidification of endosomal structures or SVs after recycling (**Fig. 5D, F**).

Slowed replenishment of SV pools caused by defective recycling is known to cause synaptic depression, as assessed by electrophysiological measurements of post-synaptic currents (Kittelmann et al., 2013b; Krick et al., 2021a; Wu and Betz, 1998). This is also the case in *Drosophila* for animals lacking Flower (Yao et al., 2009). To address this in *C. elegans*, we measured miniature post-synaptic currents (mPSCs; minis) in BWMs (**Fig. 5G**), which reflect the post-synaptic effects of presynaptic neurotransmitter release (Liewald et al., 2008; Weissenberger et al., 2011). Animals lacking FLWR-1 showed no significant difference in basal mPSC frequency or amplitude (**Fig. 5H, I; Figure 5 – Figure supplement 1A, B**) which is in accordance with FLWR-1 being dispensable in basal swimming locomotion (**Fig. 1C, D**). Similarly, pulsed optogenetic stimulation of cholinergic neurons at different frequencies did not reveal a difference in the measured currents between wild type and mutants (**Figure 5 – Figure supplement 1C, D**), suggesting that FLWR-1 might be needed only during continuous stimulation. Indeed, *flwr-1* mutants showed an accelerated rundown of the mPSC frequency in BWMs during constant illumination (**Fig. 5G, H**). This is in accordance with a role of FLWR-1 in SV recycling. Surprisingly, mPSC amplitudes in *flwr-1* mutants are reduced during 30 s hyperstimulation (**Fig. 5I, J**). This suggests that either the amount of neurotransmitter released from a single SV, or the number of multivesicular fusion events, is decreased (Liu et al., 2005). The absolute mPSC frequency, which represents the number of SVs fusing per time, was also smaller during continuous stimulation in *flwr-1* animals (**Figure 5 – Figure supplement 1E-G**). These results contrast the increased Ca^{2+} responses of cholinergic neurons we observed (**Fig. 4E, F**). Since cholinergic neurons also stimulate GABAergic neurons, and since GABAergic minis are also evaluated here, the dissection of animals, required for electrophysiological recordings, could have damaged neuronal commissures, causing an interruption of physiological signal transmission, which is otherwise observed in intact animals. We further analyzed whether *flwr-1* mutants can recover from strong optogenetic 30 s stimulation by applying a short stimulus after a recovery period (inter-stimulus interval, ISI) of 15 s, and found no significant difference to wild type (**Figure 5 – Figure supplement 1E, H)**. This suggests that a 15 s ISI is sufficient for *flwr-1* mutants to recover to the same extent as wild type synapses. In sum, our results support a facilitatory role of FLWR-1 in SV recycling specifically during continuous stimulation.

Loss of FLWR-1 leads to depleted SV pools and accumulation of endocytic structures post stimulation

Mutants in which endocytosis is affected commonly have fewer SVs because of defective recovery of SV components; this was also found for presynaptic boutons in *Drosophila* mutants lacking Flower

(Schuske et al., 2003; Yao et al., 2009). Such a defect is even more pronounced when samples are conserved immediately following optogenetic stimulation by high-pressure freezing (Kittelmann et al., 2013b; Weimer, 2006; Yu et al., 2018). In nematodes, this optogenetic stimulation can be controlled by comparing animals supplemented with ATR, the ChR2 chromophore (Nagel et al., 2005), to animals without ATR. Ultrastructural analysis using transmission electron microscopy (TEM) indeed revealed fewer SVs in stimulated *flwr-1* mutant synapses compared to wild type (**Fig. 6A, B**). This indicates that *flwr-1* mutants, unlike wild type, are unable to refill SV pools sufficiently fast. At the same time, *Drosophila* Flower mutants were shown to be defective in formation of bulk endosomal structures after strong stimulation (Yao et al., 2017). In contrast to this, we observed an increased, rather than decreased, number of endocytic structures (large vesicles / '100 nm vesicles') in stimulated *flwr-1* mutant synapses (**Fig. 6C)**. This may either be caused by increased SV fusion which triggers bulk endosomal formation (Clayton et al., 2008; Wu et al., 2014) or defective breakdown of these endocytic structures (Gan and Watanabe, 2018; Watanabe et al., 2013; Yu et al., 2018). Previously, we observed the formation of very large endocytic structures in mutants that affect their resolution into SVs, like endophilin or synaptojanin (Kittelmann et al., 2013b), while a dynamin mutant showed unresolved endocytic structures at, and in continuity with, the PM. Our pHluorin imaging data (**Fig. 5C - F**), would support the notion that both, increased SV fusion as well as defective recovery and subsequent acidification of SVs, may cause the higher number of endocytic structures in *flwr-1* mutants. However, we note that our stimulation regime likely resembles a more physiological activation of neurotransmission compared to the intense stimuli previously used (Yao et al., 2017), as wild type synapses only rarely contained endocytic structures (Kittelmann et al., 2013b). Moreover, we observed fewer docked vesicles in *flwr-1* animals which have been treated with ATR, compared to those without (**Fig. 6D**). This might be caused by increased SV fusion and is in line with the increased Ca^{2+}-levels during stimulation we observed before. The number of neuropeptide-containing dense core vesicles (DCVs) was unchanged in animals lacking FLWR-1 (**Figure 6 – Figure supplement 1**).

The increased Ca^{2+}-levels of *flwr-1* neurons may be caused by deregulation of MCA-3

While a facilitating role of Flower in endocytosis appears to be conserved in *C. elegans*, we found no evidence that FLWR-1 conducts Ca^{2+} upon insertion into the PM (Yao et al., 2009). On the contrary, presynaptic Ca^{2+} levels were increased during photostimulation of neurons in animals lacking FLWR-1. We thus wondered whether clearance of Ca^{2+} which has entered the synapse via VGCCs, might be defective in *flwr-1* mutants. In neurons and muscles, the plasma membrane Ca^{2+} ATPase (PMCA) is involved in extruding Ca^{2+} from the cell (Boczek et al., 2019; Krebs, 2022; Krick et al., 2021a). The *C. elegans* homolog MCA-3 (also known as CUP-7) is expressed in neurons, muscle cells and CCs (**Figure 7 – Figure supplement 1A**, **Table S3**; Bednarek et al. (2007); Taylor et al. (2021)). Interestingly, reducing the function of MCA-3 by mutation was shown to cause a similar defect in endocytosis of secreted GFP in CCs as the loss of FLWR-1 does (**Fig. 5A, B**; Bednarek et al. (2007)). We therefore wondered whether MCA-3 might be negatively affected in *flwr-1* mutants. To assess this, we used a mutant *mca-3(ok2048)* lacking part of the C-terminal, regulatory calmodulin-binding domain (Consortium, 2012; Kraev et al., 1999; Mantilla et al., 2023) **Fig. 7A**). Since *mca-3* loss-of-function (l.o.f.) mutants are lethal, it is likely that this represents a reduction-of-function (r.o.f.) mutation (Bednarek et al., 2007). As expected, *mca-3* mutants displayed increased Ca^{2+} influx (or net Ca^{2+} levels, representing the summed VGCC-mediated entry and MCA-3-mediated efflux) upon optogenetic stimulation of cholinergic motor neurons, similar to the effect of the *flwr-1* mutation (**Fig**. **7B, C**). Elevated Ca^{2+} levels were not further enhanced in a *flwr-1; mca-3* double mutant. Our data suggest that the two genes are acting in a common pathway. A partially different picture was observed in aldicarb assays, as reduction of MCA-3 function conveyed aldicarb

resistance that was, however, less pronounced than for *flwr-1* mutants (**Fig. 7D**). Nevertheless, since the double mutant showed no exacerbated phenotype compared to the *flwr-1* mutant, both proteins appear to function in the same pathway. If MCA-3 function was augmented by FLWR-1, then the loss of FLWR-1 may be overcome by higher MCA-3 expression. Since the main focus of FLWR-1 was the GABAergic NMJ (**Fig. 3D, E**), we analyzed aldicarb resistance in *flwr-1* mutants in which we overexpressed MCA-3 in GABAergic neurons (**Figure 7 – Figure supplement 1B**). Indeed, MCA-3 overexpression in GABAergic neurons efficiently rescued the *flwr-1* resistance to wild type levels.

FLWR-1 structure prediction does not imply Ca^{2+} conducting ability but $PI(4,5)P_2$ binding

We observed increased rather than decreased Ca^{2+} influx during stimulation, which contrasts findings from *D. melanogaster* Flower (Yao et al., 2017). Previously, an evolutionarily conserved glutamate residue (E78 in the *Drosophila* protein) within the transmembrane domain, which was found to be essential for *Drosophila* Flower function, was suggested to represent a Ca^{2+} selectivity filter because of similarities to $Ca_v1.2$ and TRP channels (Yao et al., 2009). This group proposed that Flower, like TRP channels, can form homo-tetramers to conduct Ca^{2+} (Hoenderop et al., 2003; Yao et al., 2009; Zhang et al., 2023). We therefore wondered whether loss of the conserved glutamate residue impacts FLWR-1 function in *C. elegans* (**Fig. 8A**). Expressing a mutant variant of FLWR-1 in which glutamate 74 is exchanged to glutamine (E74Q) significantly decreased the aldicarb resistance of the *flwr-1* mutant (**Fig. 8B**), yet did not fully rescue it. This suggests that the respective glutamate is not essential for *C. elegans* FLWR-1 function. To get more insight into the putative structure and oligomerization of FLWR-1, we used Alphafold 3 (AF3) predictions to estimate the approximate location of the conserved glutamate residue within a putative FLWR-1 homo-tetramer (Abramson et al., 2024; Evans et al., 2022). One of the predicted complexes indeed revealed a pore-like structure (**Figure 8 – Figure supplement 1A**). However, while conventional Ca^{2+}-channels contain a glutamate residue within their pore domain (Chen et al., 2023), E74 of FLWR-1 is not predicted to be part of pore-lining residues in the putative tetramer (**Figure 8 – Figure supplement 1B**).

Flower, like MCA-3, was also suggested to bind to phosphatidylinositol-4,5-bisphosphate ($PI(4,5)P_2$), an important regulator of endo/exocytosis and thus SV recycling, and to affect its levels within the PM (Bednarek et al., 2007; Li et al., 2020; Lopreiato et al., 2014). Binding of transmembrane proteins (including TRP channels) to $PI(4,5)P_2$ is generally mediated by positively charged amino acid residues (lysine and arginine) close to the intracellular side of the PM, which bind to the negatively charged phosphate residues (**Figure 8 – Figure supplement 1C;** (Duncan et al., 2020; Hansen et al., 2011; Ribalet et al., 2005; Rohacs, 2024). The predicted FLWR-1 structure similarly contains basic amino acids which are likely to be close to the intracellular PM leaflet (**Figure 8 – Figure supplement 1D**). We used *in silico* docking prediction to estimate how $PI(4,5)P_2$ may bind to FLWR-1. In the resulting structure, both phosphate residues are close to lysine 31 and arginine 27 (**Figure 8 – Figure supplement 1D**). A positive charge at this position is evolutionarily conserved, suggesting an important function (**Fig. 8A**). Moreover, these amino acids have been suggested to mediate $PI(4,5)P_2$ binding in *D. melanogaster* Flower (Li et al., 2020). Expression of a mutated version of FLWR-1 in which both residues were replaced by alanine only partially rescued aldicarb resistance (**Fig. 8B**), implying that FLWR-1 function may be facilitated by these residues and their potential interaction with $PI(4,5)P_2$. These findings implicate that the conserved E74 is not essential, yet still important for FLWR-1 activity. In addition, an interaction with $PI(4,5)P_2$ *via* basic amino acids also seems to be an important factor. However, we do note that FLWR-1 structural

models as depicted here rely on *in silico* predictions. The actual biological structure of FLWR-1, or its homologues, has yet to be determined using X-ray crystallography or cryo-EM.

The pleckstrin homology (PH) domain of phospholipase Cδ (PLCδ) fused to GFP can be used to estimate PI(4,5)P_2 levels within cells (Botelho et al., 2000; Chen et al., 2014; Stauffer et al., 1998). This was used to show that reduction of MCA-3 function induced decreased PH-PLCδ-GFP fluorescence levels in CCs (Bednarek et al., 2007). We thus used this assay to assess the role of FLWR-1 in endosomal PI(4,5)P_2 levels in CCs. Mutation of *flwr-1* reduced the observed GFP fluorescence suggesting that FLWR-1 positively affects PI(4,5)P_2 levels (**Fig. 8C, D**). We further asked if the putative PI(4,5)P_2 binding site mutations would affect binding of the reporter to the CC membrane. In fact, while expressing FLWR-1 specifically in CCs fully rescued the GFP levels at the CC membrane, expressing the FLWR-1(R27A/K31A) double mutant did not rescue the phenotype, while the E74Q mutant was not significantly different to wild type (**Fig. 8C, D**). These findings indicate that FLWR-1 function affects MCA-3 activity through an interaction via PI(4,5)P_2 and that FLWR-1 may have an influence on PI(4,5)P_2 levels.

A putative direct interaction of FLWR-1 and MCA-3 may increase MCA-3 function dynamically

Next, we asked how FLWR-1 may affect MCA-3 through PI(4,5)P_2, and whether this may involve proximity of the two proteins. To test this, we used Bimolecular Fluorescence Complementation (BiFC) *in vivo*. This assay uses two non-fluorescent fragments of mVenus (VN173 and VC155, respectively), which can recombine and complement each other to form a fluorescent protein, as long as they come into close proximity within the cell (Almedom et al., 2009; Chen et al., 2007; Hu et al., 2002). The fragments can be fused to putative interaction partners and fluorescence complementation (including a covalent bond formation in the reconstituted fluorophore) verifies interaction. We thus fused the VC155 fragment to the C- terminus of FLWR-1 and the VN173 fragment to the C-terminus of MCA-3, and co-expressed both proteins (FLWR-1 was expressed from its own promoter, while MCA-3 was expressed in BWM cells; **Fig. 9A**). Fluorescence could readily be observed at the PM of muscles cells, but not in other tissues that also express FLWR-1 (**Fig. 9B**). As a control, we used two other proteins for probing interactions with FLWR-1: First, the ER-membrane protein NRA-2, which is a homologue of mammalian Nicalin, a component of the translocon-associated Nicalin-TMEM147-NOMO complex that assists folding and assembly of multipass transmembrane proteins in the ER (McGilvray et al., 2020; Smalinskaitė et al., 2022). We previously showed interactions of Nicalin/NRA-2 and the NOMO homologue NRA-4 by BiFC (Almedom et al., 2009). We would expect that FLWR-1, as a multipass TM protein, would also get into close proximity with the NRA-2/Nicalin protein upon biogenesis. Indeed, a clear ER-localized signal was observed when probing FLWR-1::VC155 and NRA-2::VN173 interactions in muscle (**Fig. 9. B**). Second, to exclude that FLWR-1 would interact with any protein presented in the BiFC assay, we used the UNC-1 stomatin, that is associated with innexin gap junctions in neurons and muscles (Chen et al., 2007). Co-expressing FLWR-1::VC155 with UNC-1::VN173 in BWMs, however, did not lead to distinct GFP reconstitution, apart from some general dim fluorescence that was hardly above the level of autofluorescence (**Fig. 9B**). These findings indicate that FLWR-1 and MCA-3 may interact with each other in the PM. If this interaction is functional, linking the two proteins via BiFC may not have adverse effects on either protein. We thus tested the transgenic animals in swimming assays (**Figure 9 – Figure supplement 1**). Neither expression of FLWR-1 with MCA-3 or FLWR-1 with NRA-2 affected swimming locomotion, showing that there were no dominant negative effects. Note that wild type FLWR-1 and MCA-3 were present in these animals. However, as *mca-3* mutants have a significant reduction in swimming ability (**Figure 9 – Figure supplement 1**), the fact that FLWR-

1/MCA-3 BiFC had no adverse effects, indicates that the physical interaction of the two proteins is in line with their native function.

These observations indicate that MCA-3 and FLWR-1 may be interacting directly, and thus their function may jointly be responsible for the Ca^{2+}-induced recycling of SVs. Since the increased Ca^{2+} levels in neurons upon stimulation in *flwr-1* mutants may reflect altered MCA-3 abundance at synapses, we tested if FLWR-1 would affect localization of MCA-3 along neuronal membranes. We expressed MCA-3b::YFP in cholinergic neurons, which was observable along axonal membranes and was enriched in synaptic specializations (**Fig. 9C**). In *flwr-1* mutants, this synaptic fluorescence was not overall altered (**Fig. 9D**), however, when we compared the YFP signals within the synaptic specializations relative to the inter-synaptic axon shafts, this demonstrated a significantly reduced presence of MCA-3 in synaptic puncta and a relocation to the axonal membranes (**Fig. 9E**). This is in line with the idea that FLWR-1 function may stabilize / augment MCA-3 expression in the plasma membrane and / or its localization in synaptic puncta, to promote efficient synaptic function and SV recycling.

Discussion

Drosophila Flower was shown to affect SV recycling and to alter synaptic Ca^{2+} levels upon stimulation. It was suggested to form a Ca^{2+} channel that gets inserted into the plasma membrane upon SV fusion. Here, we showed that also in *C. elegans*, FLWR-1 affects synaptic Ca^{2+} levels following stimulation, that FLWR-1 is localized to SVs in neuronal cells, and that in its absence, endosomal structures with slowed acidification kinetics accumulate, suggesting defective recovery of SVs from recycling endosomes. FLWR-1 may affect SV recycling by stimulating the PMCA MCA-3, possibly by directly interacting with it, and *via* modulation of $PI(4,5)P_2$ levels, may affect the abundance of MCA-3 in the synaptic membrane. We found that loss of FLWR-1 conveyed increased Ca^{2+} influx in motor neurons, particularly GABAergic neurons, thus leading to more GABA release, an E/I imbalance at the NMJ, and leading to aldicarb resistance. The function of FLWR-1 appears to be ubiquitously involved in membrane trafficking and PM-endosomal recycling, as we found it to affect endocytosis and PM $PI(4,5)P_2$ levels also in coelomocytes. Our findings are summarized in a model in **Fig. 10**.

MCA-3 was shown to facilitate endocytosis in CCs (Bednarek et al., 2007), indicating that both, increased Ca^{2+} levels as well as defective endocytosis may be influenced by deregulation / lack of stimulation of MCA-3 in *flwr-1* mutants. Whether FLWR-1 directly modulates localization or activates function of MCA-3, or whether this is caused by a homeostatic change in the absence of FLWR-1, is unclear as yet. Our finding of a putative direct interaction of FLWR-1 with MCA-3 suggests that FLWR-1 could be inserted into the PM to stimulate activity of MCA-3 already present in the PM. Alternatively, MCA-3 may undergo dynamic PM insertion and endocytic recycling as part of SVs, along with FLWR-1 (mammalian PMCA was indeed found in purified SVs; (Takamori et al., 2006). In synapses, this would automatically happen upon SV fusion, such that local Ca^{2+} extrusion at release sites would ensure synapse functionality during intense activity. Such a function of PMCA was shown in *Drosophila*, where PMCA domains delineate areas of SV fusion from areas of SV endocytosis (Krick et al., 2021b). Thus, independent Ca^{2+} signaling in these two domains, *via* the P/Q type Ca^{2+} channel Ca_v2 (UNC-2 in *C. elegans*) and the L-type Ca_v1 (EGL-19 in *C. elegans*), mediating fusion and endocytosis, respectively, are facilitated by the PMCA. MCA-3 could be acutely regulated by FLWR-1, in addition to its regulation by phospholipids (Lopreiato et al., 2014).

Proof of a direct physical interaction will have to be confirmed by biochemical assays and a biological structure of the putative FLWR-1/MCA-3 complex.

Drosophila Flower was shown to increase neuronal PI(4,5)P_2 levels, driving ADBE during sustained transmission (Li et al., 2020). We could show that an involvement with PI(4,5)P_2 is likely conserved in nematodes, requiring the putative PI(4,5)P_2 binding site residues R27 and K31 of FLWR-1. Similarly, MCA-3 was important to maintain PI(4,5)P_2 in CCs (Bednarek et al., 2007). Thus, FLWR-1 and MCA-3 may have a shared role in regulating PI(4,5)P_2 levels, or FLWR-1 PM insertion stabilizes local PI(4,5)P_2. Recently, another SV protein, synaptotagmin1 (Syt1), it was shown to influence synaptic PI(4,5)P_2 levels following inserts fusion, by recruiting PIP kinase I gamma (PIPKIγ) (Bolz et al., 2023). Syt1 provides a binding site for PIPKIγ, involving R322 and K326, as part of the sequence **R**LKK**K**. In FLWR-1, R27 and K31 are part of the sequence **R**FLA**K**.

Our results indicate that MCA-3 may be functionally affected / not stimulated in *flwr-1* mutants, explaining increased Ca^{2+} levels during neuronal stimulation (Brini and Carafoli, 2011; Chamberland et al., 2019; Ono et al., 2019). The increased Ca^{2+} influx we observed was at first surprising, since work in *Drosophila* yielded opposite results during 40 Hz electrical stimulation in neuromuscular boutons of Flower mutants (Yao et al., 2017). Upon stimulation with 10 Hz, however, these animals showed an increased GCaMP signal compared to wild type, in line with our observations. Potentially, increased Ca^{2+} in *flwr-1* mutants is only observed with lower, more physiological stimulation. Stimulation by ChrimsonSA, which we used in the Ca^{2+} imaging assays, is not as vigorous, thus we are likely in a regime comparable to the 10 Hz stimulation in *Drosophila*. Using stronger stimulation *via* ChR2(H134R), as in the electrophysiological assays, led to a prominent rundown of evoked amplitudes. This may be a consequence of lower Ca^{2+} levels, and interference of MCA-3 with UNC-2 dependent Ca^{2+} microdomains required for exocytosis, leading to less fusion events. During intense stimulation, larger amounts of PMCA/MCA-3 may be inserted into the PM due to the high number of SVs fusing. Without FLWR-1, less PI(4,5)P_2 is generated and thus MCA-3 may not be effectively recycled from the PM, thus leading to reduced Ca^{2+} levels as observed in *Drosophila*.

Even though we observed increased instead of decreased Ca^{2+} influx in *flwr-1* mutants, in line with a stimulatory effect of FLWR-1 on MCA-3, we cannot exclude a possible Ca^{2+}-conductivity of FLWR-1. It was discussed that the kinetics of Ca^{2+} influx induced by Flower in *Drosophila* are too slow and the extent too little as to directly trigger known modes of endocytosis (Brose and Neher, 2009; Leitz and Kavalali, 2016; Xue et al., 2012), e.g. by activating the Ca^{2+} sensor calmodulin (Wu et al., 2009). To assess the possibility of FLWR-1 forming an ion channel we asked AlphaFold3 to model FLWR-1 as a tetramer. The putative pore lining residues were mostly hydrophobic or apolar, thus not in agreement with a function as an ion channel. The suggested similarity to the selectivity filter of VGCCs, including the sequence EGW or EAW (in FLWR-1 this is EAP; Yao et al. (2009) was not confirmed in the AF3 models: While glutamate faces the extracellular end of the VGCC pore in all four channel modules, $E74_{FLWR-1}$ pointed away from the pore. We thus think that FLWR-1 is unlikely to form an ion channel, and suggest that it facilitates SV recycling by stimulating MCA-3 activity.

Activating PMCAs *via* PI(4,5)P_2 (Berrocal et al., 2017) would remove Ca^{2+} and prevent sustained phospholipase C activity, thus protecting PI(4,5)P_2 at the PM from hydrolysis (Lopreiato et al., 2014; Penniston et al., 2014), and activating different forms of endocytosis (Blumrich et al., 2023; Bolz et al., 2023; Posor et al., 2015). Such interactions could further trigger a positive feedback loop leading to invagination of the PM (Yao et al., 2017). Both PMCAs and Flower were suggested to directly bind PI(4,5)P_2 using positively charged amino acid residues close to the membrane (Filoteo et al., 1992; Li et al., 2020). In line with this, the FLWR-1 structure model exhibits amino acids in suitable

positions. This could lead to a close arrangement of both proteins in PI(4,5)P_2 lipid microdomains (Katan and Cockcroft, 2020). Flower could also activate PMCAs in intracellular compartments. One PMCA variant was shown to mainly localize to recycling SVs and endosomes, and Ca^{2+} influx into these is an important factor in clearance from the pre-synapse (Ono et al., 2019). Overall, this may explain our finding of increased numbers of large endocytic structures in *flwr-1* synapses. Effects of *flwr-1* mutations on PI(4,5)P_2 at the PM may negatively affect ADBE, while effects on PI(4,5)P_2 in bulk endosomes may slow the breakdown of these structures (**Fig. 10**). Our ultrastructural analysis contrasts EM analyses in *Drosophila* which yielded fewer, rather than more, bulk endosomal structures in Flower mutants (Li et al., 2020; Yao et al., 2017). However, this was following prolonged (ten minute) stimulation, possibly resulting in different outcomes compared to our 30 s optogenetic stimulus. Alternatively, the subcellular localization of Flower function may differ between organisms.

Last, Flower could facilitate endocytosis through calcineurin (Yao et al., 2017), to stimulate bulk endosome formation. This Ca^{2+}- and calmodulin-dependent phosphatase dephosphorylates endocytic proteins to accelerate SV recycling (Cousin and Robinson, 2001; Kumashiro et al., 2005; Yamashita, 2012). How could the increased Ca^{2+} levels in the absence of FLWR-1 and the decreased rate of pHluorin decay fit to this idea? Possibly, increased activation of calcineurin shifts the endocytic mode from ultrafast endocytosis (UFE) (Watanabe et al., 2013) to ADBE (Kittelmann et al., 2013b; Yamashita, 2012). Structures formed by bulk endocytosis are acidified more slowly than small endocytic vesicles generated by UFE, which could explain the delayed decay of pHluorin fluorescence (Gross and von Gersdorff, 2016; Okamoto et al., 2016). More pronounced neurotransmission, due to increased SV fusion, causes an increase in bulk invaginations (Clayton et al., 2008), yet the endocytic structures formed this way are not efficiently disassembled. The *C. elegans* calcineurin TAX-6 is further involved in activity-dependent bulk endocytic processes, yet in a different context, i.e. reorganization of GABAergic synapses during development (Cuentas-Condori et al., 2023; Miller-Fleming et al., 2016). The remote possibility that FLWR-1 also takes part in this process could imply that developmental aspects of FLWR-1 function may influence E/I balance in adult NMJs.

In sum, our work confirms a conserved role of FLWR-1 in neurotransmission and SV recycling even though we observed differences to data from *Drosophila* NMJs. We found an unexpected upregulation of neurotransmission in *flwr-1* mutants which has not yet been observed in other animals, and which may result from FLWR-1 acting on PMCAs directly. The observed reduced Ca^{2+} levels in hyper-stimulated *Drosophila* synapses may instead result from ‘stranded’ PMCA in the PM, due to impaired recycling, thus increasing Ca^{2+} extrusion. Further investigations are required to confirm involvement of FLWR-1 in MCA-3 regulation and the nature of the relationship between these proteins.

Author Contributions

MS created plasmids. MS and NS generated strains. MS performed light microscopy, swimming assays, pharmacological assays and body length measurements. SS conducted aldicarb assays. JR and DR prepared EM samples and conducted EM experiments. JL performed electrophysiology. NR generated primary neuronal cell cultures. MS and AG designed and coordinated the study. MS and AG wrote the manuscript. AG and SE supervised the work and acquired funding. All authors read and approved the final manuscript.

Funding

This project was funded by Deutsche Forschungsgemeinschaft, Collaborative Research Centre 1080 project B02 (grants CRC1080/B2 and GO1011/13-2), as well as by core funding from Goethe University.

Acknowledgments

We are indebted to Katharina Kuhlmeier for expert technical assistance, and members of the Gottschalk group for critical comments regarding the manuscript. We further thank Martina Rudgalvyte from the Glauser Lab (Université de Fribourg) for helpful comments. We express our gratitude to members of the Zimmer Lab (University of Vienna) for providing advice and plasmids for GCaMP imaging, and to the Wang Lab (University of Connecticut), as well as the Zhen lab (University of Toronto) for providing plasmids. Some deletion mutations used in this work were provided by the International *C. elegans* Gene Knockout Consortium (*C. elegans* Gene Knockout Facility at the Oklahoma Medical Research Foundation, which is funded by the National Institutes of Health, and the *C. elegans* Reverse Genetics Core Facility at the University of British Columbia, which is funded by the Canadian Institute for Health Research, Genome Canada, Genome B.C., the Michael Smith Foundation, and the National Institutes of Health). Finally, we thank the *Caenorhabditis* Genetics Center (CGC), which is funded by the NIH Office of Research Infrastructure Programs (P40 OD010440), for providing strains.

References

Abramson, J., Adler, J., Dunger, J., Evans, R., Green, T., Pritzel, A., Ronneberger, O., Willmore, L., Ballard, A.J., Bambrick, J., *et al.* (2024). Accurate structure prediction of biomolecular interactions with AlphaFold 3. Nature *630*, 493-500.

Alabi, A.A., and Tsien, R.W. (2012). Synaptic vesicle pools and dynamics. Cold Spring Harb Perspect Biol *4*, a013680.

Almedom, R.B., Liewald, J.F., Hernando, G., Schultheis, C., Rayes, D., Pan, J., Schedletzky, T., Hutter, H., Bouzat, C., and Gottschalk, A. (2009). An ER-resident membrane protein complex regulates nicotinic acetylcholine receptor subunit composition at the synapse. EMBO J *28*, 2636-2649.

Aoki, I., Golinelli, L., Dunkel, E., Bhat, S., Bassam, E., Beets, I., and Gottschalk, A. (2024). Hierarchical regulation of functionally antagonistic neuropeptides expressed in a single neuron pair. Nat Commun *15*, 9504.

Bednarek, E.M., Schaheen, L., Gaubatz, J., Jorgensen, E.M., and Fares, H. (2007). The plasma membrane calcium ATPase MCA-3 is required for clathrin-mediated endocytosis in scavenger cells of Caenorhabditis elegans. Traffic *8*, 543-553.

Berrocal, M., Corbacho, I., Sepulveda, M.R., Gutierrez-Merino, C., and Mata, A.M. (2017). Phospholipids and calmodulin modulate the inhibition of PMCA activity by tau. Biochim Biophys Acta Mol Cell Res *1864*, 1028-1035.

Bhatla, N. (2012). Exon-Intron Graphic Maker. Available at http://wormweb.org/exonintron.

Blazie, S.M., and Jin, Y. (2018). Pharming for Genes in Neurotransmission: Combining Chemical and Genetic Approaches in Caenorhabditis elegans. ACS Chem Neurosci *9*, 1963-1974.

Blumrich, E.M., Nicholson-Fish, J.C., Pronot, M., Davenport, E.C., Kurian, D., Cole, A., Smillie, K.J., and Cousin, M.A. (2023). Phosphatidylinositol 4-kinase IIalpha is a glycogen synthase kinase 3-regulated interaction hub for activity-dependent bulk endocytosis. Cell reports *42*, 112633.

Boczek, T., Radzik, T., Ferenc, B., and Zylinska, L. (2019). The Puzzling Role of Neuron-Specific PMCA Isoforms in the Aging Process. Int J Mol Sci *20*.

Bolz, S., Kaempf, N., Puchkov, D., Krauss, M., Russo, G., Soykan, T., Schmied, C., Lehmann, M., Müller, R., Schultz, C., *et al.* (2023). Synaptotagmin 1-triggered lipid signaling facilitates coupling of exo- and endocytosis. Neuron *111*, 3765-3774.e3767.

Botelho, R.J., Teruel, M., Dierckman, R., Anderson, R., Wells, A., York, J.D., Meyer, T., and Grinstein, S. (2000). Localized biphasic changes in phosphatidylinositol-4,5-bisphosphate at sites of phagocytosis. J Cell Biol *151*, 1353-1368.

Brenner, S. (1974). The genetics of Caenorhabditis elegans. Genetics *77*, 71-94.

Brini, M., and Carafoli, E. (2011). The plasma membrane Ca(2)+ ATPase and the plasma membrane sodium calcium exchanger cooperate in the regulation of cell calcium. Cold Spring Harb Perspect Biol *3*.

Brose, N., and Neher, E. (2009). Flowers for synaptic endocytosis. Cell *138*, 836-837.

Calahorro, F., and Izquierdo, P.G. (2018). The presynaptic machinery at the synapse of C. elegans. Invert Neurosci *18*, 4.

Calhoun, A.J., Chalasani, S.H., and Sharpee, T.O. (2014). Maximally informative foraging by Caenorhabditis elegans. eLife *3*.

Camara, D.F., Machado, M.L., Arantes, L.P., Silva, T.C., Silveira, T.L., Leal, J.G., Dornelles, L., Stefanello, S.T., and Soares, F.A.A. (2019). MPMT-OX up-regulates GABAergic transmission and protects against seizure-like behavior in Caenorhabditis elegans. Neurotoxicology *74*, 272-281.

Chamberland, S., Zamora Moratalla, A., and Topolnik, L. (2019). Calcium extrusion mechanisms in dendrites of mouse hippocampal CA1 inhibitory interneurons. Cell Calcium *77*, 49-57.

Chanaday, N.L., Cousin, M.A., Milosevic, I., Watanabe, S., and Morgan, J.R. (2019). The Synaptic Vesicle Cycle Revisited: New Insights into the Modes and Mechanisms. The Journal of Neuroscience *39*, 8209-8216.

Chang, H.F., Mannebach, S., Beck, A., Ravichandran, K., Krause, E., Frohnweiler, K., Fecher-Trost, C., Schirra, C., Pattu, V., Flockerzi, V., *et al.* (2018). Cytotoxic granule endocytosis depends on the Flower protein. J Cell Biol *217*, 667-683.

Chen, B., Liu, Q., Ge, Q., Xie, J., and Wang, Z.W. (2007). UNC-1 regulates gap junctions important to locomotion in C. elegans. Curr Biol *17*, 1334-1339.

Chen, C.K., Bregere, C., Paluch, J., Lu, J.F., Dickman, D.K., and Chang, K.T. (2014). Activity-dependent facilitation of Synaptojanin and synaptic vesicle recycling by the Minibrain kinase. Nature communications *5*, 4246.

Chen, Z., Mondal, A., Abderemane-Ali, F., Jang, S., Niranjan, S., Montano, J.L., Zaro, B.W., and Minor, D.L., Jr. (2023). EMC chaperone-Ca(V) structure reveals an ion channel assembly intermediate. Nature *619*, 410-419.

Clayton, E.L., Evans, G.J., and Cousin, M.A. (2008). Bulk synaptic vesicle endocytosis is rapidly triggered during strong stimulation. J Neurosci *28*, 6627-6632.

Coelho, D.S., and Moreno, E. (2020). Neuronal Selection Based on Relative Fitness Comparison Detects and Eliminates Amyloid-beta-Induced Hyperactive Neurons in Drosophila. iScience *23*, 101468.

Cong, D., Ren, J., Zhou, Y., Wang, S., Liang, J., Ding, M., and Feng, W. (2021). Motor domain-mediated autoinhibition dictates axonal transport by the kinesin UNC-104/KIF1A. PLoS Genet *17*, e1009940.

Consortium, C.e.D.M. (2012). large-scale screening for targeted knockouts in the Caenorhabditis elegans genome. G3 (Bethesda) *2*, 1415-1425.

Costa-Rodrigues, C., Couceiro, J., and Moreno, E. (2021). Cell competition from development to neurodegeneration. Dis Model Mech *14*.

Cousin, M.A., and Robinson, P.J. (2001). The dephosphins: dephosphorylation by calcineurin triggers synaptic vesicle endocytosis. Trends Neurosci *24*, 659-665.

Cuentas-Condori, A., Chen, S., Krout, M., Gallik, K.L., Tipps, J., Gailey, C., Flautt, L., Kim, H., Mulcahy, B., Zhen, M., *et al.* (2023). The epithelial Na(+) channel UNC-8 promotes an endocytic mechanism that recycles presynaptic components to new boutons in remodeling neurons. Cell reports *42*, 113327.

Dai, Y., Taru, H., Deken, S.L., Grill, B., Ackley, B., Nonet, M.L., and Jin, Y. (2006). SYD-2 Liprin-alpha organizes presynaptic active zone formation through ELKS. Nat Neurosci *9*, 1479-1487.

Dittman, J.S., and Kaplan, J.M. (2006). Factors regulating the abundance and localization of synaptobrevin in the plasma membrane. Proc Natl Acad Sci U S A *103*, 11399-11404.

Duncan, A.L., Song, W., and Sansom, M.S.P. (2020). Lipid-Dependent Regulation of Ion Channels and G Protein-Coupled Receptors: Insights from Structures and Simulations. Annu Rev Pharmacol Toxicol *60*, 31-50.

Eberhardt, J., Santos-Martins, D., Tillack, A.F., and Forli, S. (2021). AutoDock Vina 1.2.0: New Docking Methods, Expanded Force Field, and Python Bindings. J Chem Inf Model *61*, 3891-3898.

Edelstein, A.D., Tsuchida, M.A., Amodaj, N., Pinkard, H., Vale, R.D., and Stuurman, N. (2014). Advanced methods of microscope control using muManager software. J Biol Methods *1*.

Evans, R., O'Neill, M., Pritzel, A., Antropova, N., Senior, A., Green, T., Žídek, A., Bates, R., Blackwell, S., Yim, J., *et al.* (2022). Protein complex prediction with AlphaFold-Multimer. bioRxiv, 2021.2010.2004.463034.

Fares, H., and Grant, B. (2002). Deciphering endocytosis in Caenorhabditis elegans. Traffic *3*, 11-19.

Fares, H., and Greenwald, I. (2001). Genetic analysis of endocytosis in Caenorhabditis elegans: coelomocyte uptake defective mutants. Genetics *159*, 133-145.

Filoteo, A.G., Enyedi, A., and Penniston, J.T. (1992). The lipid-binding peptide from the plasma membrane Ca2+ pump binds calmodulin, and the primary calmodulin-binding domain interacts with lipid. J Biol Chem *267*, 11800-11805.

Fire, A. (1986). Integrative transformation of Caenorhabditis elegans. EMBO J *5*, 2673-2680.

Fleming, J.T., Squire, M.D., Barnes, T.M., Tornoe, C., Matsuda, K., Ahnn, J., Fire, A., Sulston, J.E., Barnard, E.A., Sattelle, D.B., *et al.* (1997). Caenorhabditis elegans levamisole resistance genes lev-1, unc-29, and unc-38 encode functional nicotinic acetylcholine receptor subunits. J Neurosci *17*, 5843-5857.

Gally, C., and Bessereau, J.L. (2003). GABA is dispensable for the formation of junctional GABA receptor clusters in Caenorhabditis elegans. J Neurosci *23*, 2591-2599.

Gan, Q., and Watanabe, S. (2018). Synaptic Vesicle Endocytosis in Different Model Systems. Front Cell Neurosci *12*, 171.

Gottschalk, A., Almedom, R.B., Schedletzky, T., Anderson, S.D., Yates, J.R., 3rd, and Schafer, W.R. (2005). Identification and characterization of novel nicotinic receptor-associated proteins in Caenorhabditis elegans. EMBO J *24*, 2566-2578.

Gross, O.P., and von Gersdorff, H. (2016). Recycling at synapses. eLife *5*.

Hall, D.H., and Hedgecock, E.M. (1991). Kinesin-related gene unc-104 is required for axonal transport of synaptic vesicles in C. elegans. Cell *65*, 837-847.

Hallgren, J., Tsirigos, K.D., Pedersen, M.D., Almagro Armenteros, J.J., Marcatili, P., Nielsen, H., Krogh, A., and Winther, O. (2022). DeepTMHMM predicts alpha and beta transmembrane proteins using deep neural networks. bioRxiv, 2022.2004.2008.487609.

Hansen, S.B., Tao, X., and MacKinnon, R. (2011). Structural basis of PIP2 activation of the classical inward rectifier K+ channel Kir2.2. Nature *477*, 495-498.

Haucke, V., Neher, E., and Sigrist, S.J. (2011). Protein scaffolds in the coupling of synaptic exocytosis and endocytosis. Nat Rev Neurosci *12*, 127-138.

Hoenderop, J.G., Voets, T., Hoefs, S., Weidema, F., Prenen, J., Nilius, B., and Bindels, R.J. (2003). Homo- and heterotetrameric architecture of the epithelial Ca2+ channels TRPV5 and TRPV6. EMBO J *22*, 776-785.

Hu, C.D., Chinenov, Y., and Kerppola, T.K. (2002). Visualization of interactions among bZIP and Rel family proteins in living cells using bimolecular fluorescence complementation. Mol Cell *9*, 789-798.

Hu, Z., Hom, S., Kudze, T., Tong, X.-J., Choi, S., Aramuni, G., Zhang, W., and Kaplan, J.M. (2012). Neurexin and Neuroligin Mediate Retrograde Synaptic Inhibition in C. elegans. Science *337*, 980-984.

Janosi, B., Liewald, J.F., Seidenthal, M., Yu, S.C., Umbach, S., Redzovic, J., Rentsch, D., Alcantara, I.C., Bergs, A.C.F., Schneider, M.W., *et al.* (2024). RIM and RIM-Binding Protein Localize Synaptic CaV2 Channels to Differentially Regulate Transmission in Neuronal Circuits. J Neurosci *44*.

Katan, M., and Cockcroft, S. (2020). Phosphatidylinositol(4,5)bisphosphate: diverse functions at the plasma membrane. Essays Biochem *64*, 513-531.

Kittelmann, M., Hegermann, J., Goncharov, A., Taru, H., Ellisman, M.H., Richmond, J.E., Jin, Y., and Eimer, S. (2013a). Liprin-alpha/SYD-2 determines the size of dense projections in presynaptic active zones in C. elegans. J Cell Biol *203*, 849-863.

Kittelmann, M., Liewald, J.F., Hegermann, J., Schultheis, C., Brauner, M., Steuer Costa, W., Wabnig, S., Eimer, S., and Gottschalk, A. (2013b). In vivo synaptic recovery following optogenetic hyperstimulation. Proc Natl Acad Sci U S A *110*, E3007-3016.

Klopfenstein, D.R., and Vale, R.D. (2004). The lipid binding pleckstrin homology domain in UNC-104 kinesin is necessary for synaptic vesicle transport in Caenorhabditis elegans. Mol Biol Cell *15*, 3729-3739.

Kononenko, N.L., and Haucke, V. (2015). Molecular mechanisms of presynaptic membrane retrieval and synaptic vesicle reformation. Neuron *85*, 484-496.

Kraev, A., Kraev, N., and Carafoli, E. (1999). Identification and functional expression of the plasma membrane calcium ATPase gene family from Caenorhabditis elegans. J Biol Chem *274*, 4254-4258.

Krebs, J. (2022). Structure, Function and Regulation of the Plasma Membrane Calcium Pump in Health and Disease. Int J Mol Sci *23*.

Krick, N., Ryglewski, S., Pichler, A., Bikbaev, A., Gotz, T., Kobler, O., Heine, M., Thomas, U., and Duch, C. (2021a). Separation of presynaptic Ca(v)2 and Ca(v)1 channel function in synaptic vesicle exo- and endocytosis by the membrane anchored Ca(2+) pump PMCA. Proc Natl Acad Sci U S A *118*.

Krick, N., Ryglewski, S., Pichler, A., Bikbaev, A., Götz, T., Kobler, O., Heine, M., Thomas, U., and Duch, C. (2021b). Separation of presynaptic Ca_v2 and Ca_v1 channel function in synaptic vesicle exo- and endocytosis by the membrane anchored Ca²⁺ pump PMCA. Proceedings of the National Academy of Sciences *118*, e2106621118.

Kumashiro, S., Lu, Y.F., Tomizawa, K., Matsushita, M., Wei, F.Y., and Matsui, H. (2005). Regulation of synaptic vesicle recycling by calcineurin in different vesicle pools. Neurosci Res *51*, 435-443.

Larkin, M.A., Blackshields, G., Brown, N.P., Chenna, R., McGettigan, P.A., McWilliam, H., Valentin, F., Wallace, I.M., Wilm, A., Lopez, R., *et al.* (2007). Clustal W and Clustal X version 2.0. Bioinformatics *23*, 2947-2948.

Leitz, J., and Kavalali, E.T. (2016). Ca2+ Dependence of Synaptic Vesicle Endocytosis. Neuroscientist *22*, 464-476.

Li, T.N., Chen, Y.J., Lu, T.Y., Wang, Y.T., Lin, H.C., and Yao, C.K. (2020). A positive feedback loop between Flower and PI(4,5)P(2) at periactive zones controls bulk endocytosis in Drosophila. eLife *9*.

Liewald, J.F., Brauner, M., Stephens, G.J., Bouhours, M., Schultheis, C., Zhen, M., and Gottschalk, A. (2008). Optogenetic analysis of synaptic function. Nat Methods *5*, 895-902.

Liu, Q., Chen, B., Yankova, M., Morest, D.K., Maryon, E., Hand, A.R., Nonet, M.L., and Wang, Z.W. (2005). Presynaptic ryanodine receptors are required for normal quantal size at the Caenorhabditis elegans neuromuscular junction. J Neurosci *25*, 6745-6754.

Lopreiato, R., Giacomello, M., and Carafoli, E. (2014a). The plasma membrane calcium pump: new ways to look at an old enzyme. J Biol Chem *289*, 10261-10268.

Lou, X. (2018). Sensing Exocytosis and Triggering Endocytosis at Synapses: Synaptic Vesicle Exocytosis-Endocytosis Coupling. Front Cell Neurosci *12*, 66.

Lu, Y., Ahamed, T., Mulcahy, B., Meng, J., Witvliet, D., Guan, S.A., Holmyard, D., Hung, W., Wen, Q., Chisholm, A.D., *et al.* (2022). Extrasynaptic signaling enables an asymmetric juvenile motor circuit to produce symmetric undulation. Curr Biol *32*, 4631-4644 e4635.

Madan, E., Pelham, C.J., Nagane, M., Parker, T.M., Canas-Marques, R., Fazio, K., Shaik, K., Yuan, Y., Henriques, V., Galzerano, A., *et al.* (2019). Flower isoforms promote competitive growth in cancer. Nature *572*, 260-264.

Mahoney, T.R., Luo, S., and Nonet, M.L. (2006). Analysis of synaptic transmission in Caenorhabditis elegans using an aldicarb-sensitivity assay. Nat Protoc *1*, 1772-1777.

Mantilla, G., Perez-Gordones, M.C., Cisneros-Montufar, S., Benaim, G., Navarro, J.C., Mendoza, M., and Ramirez-Iglesias, J.R. (2023). Structural Analysis and Diversity of Calmodulin-Binding Domains in Membrane and Intracellular Ca(2+)-ATPases. J Membr Biol *256*, 159-174.

McGilvray, P.T., Anghel, S.A., Sundaram, A., Zhong, F., Trnka, M.J., Fuller, J.R., Hu, H., Burlingame, A.L., and Keenan, R.J. (2020). An ER translocon for multi-pass membrane protein biogenesis. eLife *9*, e56889.

Miller-Fleming, T.W., Petersen, S.C., Manning, L., Matthewman, C., Gornet, M., Beers, A., Hori, S., Mitani, S., Bianchi, L., Richmond, J., *et al.* (2016). The DEG/ENaC cation channel protein UNC-8 drives activity-dependent synapse removal in remodeling GABAergic neurons. eLife *5*.

Nagel, G., Brauner, M., Liewald, J.F., Adeishvili, N., Bamberg, E., and Gottschalk, A. (2005). Light activation of channelrhodopsin-2 in excitable cells of Caenorhabditis elegans triggers rapid behavioral responses. Curr Biol *15*, 2279-2284.

Nakai, J., Ohkura, M., and Imoto, K. (2001). A high signal-to-noise Ca(2+) probe composed of a single green fluorescent protein. Nat Biotechnol *19*, 137-141.

Nonet, M.L. (1999). Visualization of synaptic specializations in live C. elegans with synaptic vesicle protein-GFP fusions. J Neurosci Methods *89*, 33-40.

Nussbaum-Krammer, C.I., Neto, M.F., Brielmann, R.M., Pedersen, J.S., and Morimoto, R.I. (2015). Investigating the spreading and toxicity of prion-like proteins using the metazoan model organism C. elegans. Journal of visualized experiments : JoVE, 52321.

Oda, K., Vierock, J., Oishi, S., Rodriguez-Rozada, S., Taniguchi, R., Yamashita, K., Wiegert, J.S., Nishizawa, T., Hegemann, P., and Nureki, O. (2018). Crystal structure of the red light-activated channelrhodopsin Chrimson. Nature communications *9*, 3949.

Okamoto, Y., Lipstein, N., Hua, Y., Lin, K.H., Brose, N., Sakaba, T., and Midorikawa, M. (2016). Distinct modes of endocytotic presynaptic membrane and protein uptake at the calyx of Held terminal of rats and mice. eLife *5*.

Ono, Y., Mori, Y., Egashira, Y., Sumiyama, K., and Takamori, S. (2019). Expression of plasma membrane calcium ATPases confers Ca(2+)/H(+) exchange in rodent synaptic vesicles. Scientific reports *9*, 4289.

Penniston, J.T., Padanyi, R., Paszty, K., Varga, K., Hegedus, L., and Enyedi, A. (2014). Apart from its known function, the plasma membrane Ca(2)(+)ATPase can regulate Ca(2)(+) signaling by controlling phosphatidylinositol 4,5-bisphosphate levels. J Cell Sci *127*, 72-84.

Petrova, E., Lopez-Gay, J.M., Rhiner, C., and Moreno, E. (2012). Flower-deficient mice have reduced susceptibility to skin papilloma formation. Dis Model Mech *5*, 553-561.

Posor, Y., Eichhorn-Grunig, M., and Haucke, V. (2015). Phosphoinositides in endocytosis. Biochim Biophys Acta *1851*, 794-804.

Rhiner, C., Lopez-Gay, J.M., Soldini, D., Casas-Tinto, S., Martin, F.A., Lombardia, L., and Moreno, E. (2010). Flower forms an extracellular code that reveals the fitness of a cell to its neighbors in Drosophila. Dev Cell *18*, 985-998.

Ribalet, B., John, S.A., Xie, L.H., and Weiss, J.N. (2005). Regulation of the ATP-sensitive K channel Kir6.2 by ATP and PIP(2). Journal of molecular and cellular cardiology *39*, 71-77.

Richmond, J.E., and Jorgensen, E.M. (1999). One GABA and two acetylcholine receptors function at the C. elegans neuromuscular junction. Nat Neurosci *2*, 791-797.

Rizzoli, S.O. (2014). Synaptic vesicle recycling: steps and principles. EMBO J *33*, 788-822.

Rohacs, T. (2024). Phosphoinositide Regulation of TRP Channels: A Functional Overview in the Structural Era. Annu Rev Physiol *86*, 329-355.

Rosignoli, S., and Paiardini, A. (2022). DockingPie: a consensus docking plugin for PyMOL. Bioinformatics *38*, 4233-4234.

Rudd, J.C., Maity, S., Grunkemeyer, J.A., Snyder, J.C., Lovas, S., and Hansen, L.A. (2023). Membrane structure and internalization dynamics of human Flower isoforms hFWE3 and hFWE4 indicate a conserved endocytic role for hFWE4. J Biol Chem *299*, 104945.

Saheki, Y., and De Camilli, P. (2012). Synaptic vesicle endocytosis. Cold Spring Harb Perspect Biol *4*, a005645.

Salcini, A.E., Hilliard, M.A., Croce, A., Arbucci, S., Luzzi, P., Tacchetti, C., Daniell, L., De Camilli, P., Pelicci, P.G., Di Fiore, P.P., *et al.* (2001). The Eps15 C. elegans homologue EHS-1 is implicated in synaptic vesicle recycling. Nat Cell Biol *3*, 755-760.

Sankaranarayanan, S., De Angelis, D., Rothman, J.E., and Ryan, T.A. (2000). The use of pHluorins for optical measurements of presynaptic activity. Biophys J *79*, 2199-2208.

Sattelle, D.B., Culetto, E., Grauso, M., Raymond, V., Franks, C.J., and Towers, P. (2002). Functional genomics of ionotropic acetylcholine receptors in Caenorhabditis elegans and Drosophila melanogaster. Novartis Found Symp *245*, 240-257; discussion 257-260, 261-244.

Schultheis, C., Brauner, M., Liewald, J.F., and Gottschalk, A. (2011). Optogenetic analysis of GABAB receptor signaling in Caenorhabditis elegans motor neurons. J Neurophysiol *106*, 817-827.

Schuske, K.R., Richmond, J.E., Matthies, D.S., Davis, W.S., Runz, S., Rube, D.A., van der Bliek, A.M., and Jorgensen, E.M. (2003). Endophilin is required for synaptic vesicle endocytosis by localizing synaptojanin. Neuron *40*, 749-762.

Seidenthal, M., Janosi, B., Rosenkranz, N., Schuh, N., Elvers, N., Willoughby, M., Zhao, X., and Gottschalk, A. (2023). pOpsicle: An all-optical reporter system for synaptic vesicle recycling combining pH-sensitive fluorescent proteins with optogenetic manipulation of neuronal activity. Front Cell Neurosci *17*, 1120651.

Seidenthal, M., Vettkotter, D., and Gottschalk, A. (2022). WormRuler: A software to track body length used to characterize a super red-shifted channelrhodopsin in Caenorhabditis elegans. MicroPubl Biol *2022*.

Simon, D.J., Madison, J.M., Conery, A.L., Thompson-Peer, K.L., Soskis, M., Ruvkun, G.B., Kaplan, J.M., and Kim, J.K. (2008). The MicroRNA miR-1 Regulates a MEF-2-Dependent Retrograde Signal at Neuromuscular Junctions. Cell *133*, 903-915.

Smalinskaitė, L., Kim, M.K., Lewis, A.J.O., Keenan, R.J., and Hegde, R.S. (2022). Mechanism of an intramembrane chaperone for multipass membrane proteins. Nature *611*, 161-166.

Stauffer, T.P., Ahn, S., and Meyer, T. (1998). Receptor-induced transient reduction in plasma membrane PtdIns(4,5)P2 concentration monitored in living cells. Curr Biol *8*, 343-346.

Swierczek, N.A., Giles, A.C., Rankin, C.H., and Kerr, R.A. (2011). High-throughput behavioral analysis in C. elegans. Nat Methods *8*, 592-598.

Takamori, S., Holt, M., Stenius, K., Lemke, E.A., Gronborg, M., Riedel, D., Urlaub, H., Schenck, S., Brugger, B., Ringler, P., *et al.* (2006). Molecular anatomy of a trafficking organelle. Cell *127*, 831-846.

Taylor, S.R., Santpere, G., Weinreb, A., Barrett, A., Reilly, M.B., Xu, C., Varol, E., Oikonomou, P., Glenwinkel, L., McWhirter, R., *et al.* (2021). Molecular topography of an entire nervous system. Cell *184*, 4329-4347 e4323.

Tong, X.J., Lopez-Soto, E.J., Li, L., Liu, H., Nedelcu, D., Lipscombe, D., Hu, Z., and Kaplan, J.M. (2017). Retrograde Synaptic Inhibition Is Mediated by alpha-Neurexin Binding to the alpha2delta Subunits of N-Type Calcium Channels. Neuron *95*, 326-340 e325.

Vashlishan, A.B., Madison, J.M., Dybbs, M., Bai, J., Sieburth, D., Ch'ng, Q., Tavazoie, M., and Kaplan, J.M. (2008). An RNAi screen identifies genes that regulate GABA synapses. Neuron *58*, 346-361.

Vettkotter, D., Schneider, M., Goulden, B.D., Dill, H., Liewald, J., Zeiler, S., Guldan, J., Ates, Y.A., Watanabe, S., and Gottschalk, A. (2022). Rapid and reversible optogenetic silencing of synaptic transmission by clustering of synaptic vesicles. Nature communications *13*, 7827.

Ward, S., Thomson, N., White, J.G., and Brenner, S. (1975). Electron microscopical reconstruction of the anterior sensory anatomy of the nematode Caenorhabditis elegans. J Comp Neurol *160*, 313-337.

Watanabe, S., Davis, M.W., Kusick, G.F., Iwasa, J., and Jorgensen, E.M. (2020). SynapsEM: Computer-Assisted Synapse Morphometry. Front Synaptic Neurosci *12*, 584549.

Watanabe, S., Liu, Q., Davis, M.W., Hollopeter, G., Thomas, N., Jorgensen, N.B., and Jorgensen, E.M. (2013). Ultrafast endocytosis at Caenorhabditis elegans neuromuscular junctions. eLife *2*, e00723.

Watanabe, S., Trimbuch, T., Camacho-Perez, M., Rost, B.R., Brokowski, B., Sohl-Kielczynski, B., Felies, A., Davis, M.W., Rosenmund, C., and Jorgensen, E.M. (2014). Clathrin regenerates synaptic vesicles from endosomes. Nature *515*, 228-233.

Weimer, R.M. (2006). Preservation of C. elegans tissue via high-pressure freezing and freeze-substitution for ultrastructural analysis and immunocytochemistry. Methods Mol Biol *351*, 203-221.

Weissenberger, S., Schultheis, C., Liewald, J.F., Erbguth, K., Nagel, G., and Gottschalk, A. (2011). PACalpha--an optogenetic tool for in vivo manipulation of cellular cAMP levels, neurotransmitter release, and behavior in Caenorhabditis elegans. J Neurochem *116*, 616-625.

Wu, L.G., and Betz, W.J. (1998). Kinetics of synaptic depression and vesicle recycling after tetanic stimulation of frog motor nerve terminals. Biophys J *74*, 3003-3009.

Wu, X.S., McNeil, B.D., Xu, J., Fan, J., Xue, L., Melicoff, E., Adachi, R., Bai, L., and Wu, L.G. (2009). Ca(2+) and calmodulin initiate all forms of endocytosis during depolarization at a nerve terminal. Nat Neurosci *12*, 1003-1010.

Wu, Y., O'Toole, E.T., Girard, M., Ritter, B., Messa, M., Liu, X., McPherson, P.S., Ferguson, S.M., and De Camilli, P. (2014). A dynamin 1-, dynamin 3- and clathrin-independent pathway of synaptic vesicle recycling mediated by bulk endocytosis. eLife *3*, e01621.

Xue, L., Zhang, Z., McNeil, B.D., Luo, F., Wu, X.S., Sheng, J., Shin, W., and Wu, L.G. (2012). Voltage-dependent calcium channels at the plasma membrane, but not vesicular channels, couple exocytosis to endocytosis. Cell reports *1*, 632-638.

Yamashita, T. (2012). Ca2+-dependent regulation of synaptic vesicle endocytosis. Neurosci Res *73*, 1-7.

Yao, C.K., Lin, Y.Q., Ly, C.V., Ohyama, T., Haueter, C.M., Moiseenkova-Bell, V.Y., Wensel, T.G., and Bellen, H.J. (2009). A synaptic vesicle-associated Ca2+ channel promotes endocytosis and couples exocytosis to endocytosis. Cell *138*, 947-960.

Yao, C.K., Liu, Y.T., Lee, I.C., Wang, Y.T., and Wu, P.Y. (2017). A Ca2+ channel differentially regulates Clathrin-mediated and activity-dependent bulk endocytosis. PLoS Biol *15*, e2000931.

Yu, S.C., Janosi, B., Liewald, J.F., Wabnig, S., and Gottschalk, A. (2018). Endophilin A and B Join Forces With Clathrin to Mediate Synaptic Vesicle Recycling in Caenorhabditis elegans. Frontiers in molecular neuroscience *11*, 196.

Zhang, M., Ma, Y., Ye, X., Zhang, N., Pan, L., and Wang, B. (2023). TRP (transient receptor potential) ion channel family: structures, biological functions and therapeutic interventions for diseases. Signal Transduct Target Ther *8*, 261.

FIGURE LEGENDS

Fig. 1. Loss of FLWR-1 induces defects in neurotransmission following intense stimulation.

(A) Alignment of the amino acid sequences of FLWR-1 to hFwe4 (*Homo sapiens*) and Fwe-Ubi (*Drosophila melanogaster*). Shading depicts evolutionary conservation of amino acid residues (identity – black; homology – grey). Position of TM helices indicated in red refers to the FLWR-1 sequence. **(B)** Schematic representation of the *flwr-1*/F20D1.1 gene locus and the size of the *ok3128* deletion. Bars represent exons and connecting lines introns. **(C)** Mean (± SEM) swimming cycles of animals expressing ChR2(H134R) in cholinergic motor neurons (*unc-17* promoter). All animals were treated with ATR. A 90 s light pulse (470 nm, 1 mW/mm^2) was applied after 30 s as indicated by the blue shade. Number of animals accumulated from N = 3 biological replicates: wild type = 80 – 88, *flwr-1* = 80 – 91, FLWR-1 rescue = 62 – 75. **(D)** Statistical analysis of swimming speed at different time points as depicted in (C). Mean (± SEM). Each dot represents a single animal. Mixed-effects model analysis with Tukey's correction. Only statistically significant differences are depicted. **$p < 0.01$, *** $p < 0.001$. **(E)** Mean (± SEM) fraction of moving animals after exposure to 1.5 mM aldicarb. N = 4 biological replicates. Two-way ANOVA with Tukey's correction. ns not significant $p > 0.05$, *** $p < 0.001$.

Fig. 2. FLWR-1 is expressed in neurons and localizes to synaptic vesicles and the plasma membrane.

(A - D) Confocal micrographs (maximum projection of z-stacks or single plane) of animals co-expressing *pflwr-1::GFP::FLWR-1* and *psnb-1::mCherry::SNB-1*. **(A)** Overview of GFP::FLWR-1 expression. Arrows indicate dorsal and ventral nerve cords (DNC and VNC, respectively). Scale bar, 100 µm. **(B)** GFP::FLWR-1 in head neurons and pharynx. Scale bar, 20 µm. **(C)** Animal depicted in (B), single plane showing neck muscle cells. Arrows indicate GFP::FLWR-1 localization to the plasma membrane. Scale bar, 20 µm. **(D)** GFP and mCherry fluorescence in the DNC. Scale bar, 10 µm. **(E)** Line scan analysis of colocalization of GFP::FLWR-1 and mCherry::SNB-1 along the DNC as represented in (D). R^2 as determined by Pearson correlation. a.u. = arbitrary units of fluorescence intensity. **(F)** Micrograph depicting GFP::FLWR-1 and mCherry::SNB-1 fluorescence in sublateral nerve cords and commissures. Arrowheads indicate synaptic puncta. Arrow points towards SV precursor travelling along commissure as shown in Supplementary Movie 1. Scale bar, 10 µm. **(G)** Kymograph representing the SV precursor indicated in (F) travelling along commissures. Scale bar, 2 µm. **(H)** Comparison of the ratio of DNC to VNC fluorescence of GFP::FLWR-1 and mCherry::SNB-1 in wild type and *unc-104(e1265)* mutant background. Mean (± SEM). Each dot represents a single animal. Two-way ANOVA with Šídák's correction. *** $p < 0.001$. Number of animals imaged in N = 3 biological replicates: wild type = 33, *unc-104* = 29.

Fig. 3. GABAergic signaling is increased in *flwr-1* knockout mutants.

(A) Representative confocal micrographs of an animal co-expressing *pflwr-1::GFP::FLWR-1* and *TagRFP::ELKS-1* in cholinergic motor neurons (*unc-17(short)* promoter). The region in the DNC used to acquire images shown in **B** and **C** is indicated; this position is posterior to the vulva, anterior is left. Scale bar, 10 µm. **(B, C)** DNCs in animals co-expressing *pflwr-1::GFP::FLWR-1* and *TagRFP::ELKS-1* in cholinergic motor neurons (*unc-17(short)* promoter), or in GABAergic neurons (*unc-47* promoter; C), respectively. Scale bar, 5 µm. Examples of fluorescent puncta which contain either both, FLWR-1 and ELKS-1 (blue arrowheads), or FLWR-1 only (red arrowheads) are indicated. The same puncta are indicated in the respective analysis of signal density along the DNC in **Figure 3 – Figure supplement 1A, B**. **(D)** Mean (± SEM) fraction of moving animals after exposure to 1.5 mM aldicarb with cholinergic (*punc-17*) and GABAergic (*punc-47*) expression of FLWR-1 in *flwr-1(ok3128)* mutant background. N = 3 - 8 biological replicates. **(E)** Mean (± SEM) fraction of moving animals after exposure to 1.5 mM aldicarb with *unc-47(e307)* and *unc-47(e307)/flwr-1(ok3128)* double mutants. N = 3 biological replicates. Two-way ANOVA with Tukey's correction in D, E. ns not significant, *** $p < 0.001$.

Fig. 4. Loss of FLWR-1 leads to increased Ca^{2+} levels during stimulation.

(A) Mean (± SEM) normalized fluorescence in synaptic puncta of the DNC of animals expressing GCaMP3 and ChrimsonSA in GABAergic neurons (*unc-25* promoter). All animals were supplemented with ATR. A 10 s light pulse (590 nm, 40 µW/mm^2) was applied after 5 s as indicated by the red shade. **(B)** Mean (± SEM) normalized fluorescence during stimulation (seconds 6 to 14) as depicted in (A). Each dot indicates a single animal. Unpaired t-test. ** $p < 0.01$. **(A + B)** Number of animals imaged in N = 5 biological replicates: wild type = 40, *flwr-1* = 41. Outliers were removed from both datasets as detected by the iterative Grubb's method (GraphPad Prism). **(C)** Mean (± SEM) body length of

animals expressing ChR2(H134R) in GABAergic neurons (*unc-47* promoter) in the *unc-29(e1072)* mutant background, normalized to the average before stimulation. All animals were supplemented with ATR. A 20 s light pulse (470 nm, 100 µW/mm^2) was applied after 5 s as indicated by the blue shade. **(D)** Mean (± SEM) relative body length during stimulation (seconds 6 to 24) as depicted in (C). Each dot indicates a single animal. Unpaired t-test. * $p < 0.05$. Number of animals measured in N = 4 biological replicates: wild type = 51, *flwr-1* = 49. **(E)** Mean (± SEM) normalized fluorescence in synaptic puncta of the DNC of animals expressing GCaMP6f and ChrimsonSA in cholinergic motor neurons (*unc-17b* promoter). All animals were supplemented with ATR. A 10 s light pulse (590 nm, 40 µW/mm^2) was applied after 5 s as indicated by red shade. **(F)** Median (with IQR) normalized fluorescence during stimulation (seconds 6 to 14) as depicted in (E). Each dot indicates a single animal. Kruskal-Wallis test. Only statistically significant differences are depicted. * $p < 0.05$, ** $p < 0.01$. **(E + F)** Number of animals imaged in N = 5 biological replicates: wild type = 40, *flwr-1* = 38, cholinergic rescue = 39, muscle rescue = 36. No outliers were detected by the iterative Grubb's method. **(G)** Schematic representation of motor neuron innervation of BWMs. Arrows indicate the putatively increased (green) or decreased (red) neurotransmission/excitation of the involved cell types in *flwr-1* mutants compared to wildtype.

Fig. 5. FLWR-1 facilitates endocytosis in non-neuronal and neuronal cells.

(A) Exemplary images of the coelomocytes (CCs) in wild type, *flwr-1(ok3128)* and in *flwr-1* mutants expressing FLWR-1 in CCs (*unc-122* promoter). GFP containing a secretion signal sequence (ssGFP) was expressed in BWMs (*myo-3* promoter). Scale bar, 10 µm. **(B)** Median (with IQR) normalized fluorescence of CCs. Each dot indicates a single CC. Kruskal-Wallis test. ** $p < 0.001$*** $p < 0.001$. Number of CCs imaged in N = 3 biological replicates: wild type = 158, *flwr-1* = 185, rescue = 113. **(C)** Mean (± SEM) normalized DNC fluorescence of animals expressing SNG-1::pHluorin and ChrimsonSA in cholinergic neurons (*unc-17* promoter). All animals were supplemented with ATR. A 30 s light pulse (590 nm, 40 µW/mm^2) was applied after 10 s as indicated by the red shade. **(D)** Mean (± SEM) pHluorin fluorescence as depicted in (C) but additionally normalized to the maximum value of each dataset. **(E)** Mean (± SEM) normalized fluorescence during stimulation (seconds 15 to 35) as depicted in (C). Each dot indicates a single animal. Unpaired t-test. **(F)** Mean (± SEM) calculated exponential decay constants of fluorescence decline after stimulation. Each dot indicates a single animal. Unpaired t-test. **(C – F)** Number of animals imaged in N = 5 biological replicates: wild type = 27, *flwr-1* = 32. * $p < 0.05$. **(G)** Representative voltage-clamp recordings of currents in BWMs. Animals expressing ChR2(H134R) in cholinergic motor neurons (*unc-17* promoter, transgene *zxIs6*) were treated with ATR. A 30 s light stimulus (470 nm, 8 mW/mm^2) was applied as indicated by blue bars. **(H)** Normalized mPSC frequency in BWMs. All animals were treated with ATR. A 30 s light pulse (470 nm, 8 mW/mm^2) was applied as indicated by the blue shade. Dashed lines indicate one-phase exponential regression analysis fitted to the mean mPSC frequencies during stimulation. Calculated time constants of decay are shown. Two-way ANOVA with Šidák's correction. All significant differences to wild type are depicted. **(I)** mPSC amplitude in BWMs of animals measured in (G + H). **(J)** Mean (± SEM) mPSC amplitude during light stimulation as indicated in (I). Unpaired t-test. * $p < 0.05$. (G - J) Number of animals: wild type = 9, *flwr-1* = 8.

Fig. 6. Ultra-structural analysis reveals defective recycling of SVs after stimulation in *flwr-1* mutants.

(A) Representative TEM micrographs of cholinergic *en-passant* synapses in wild type and *flwr-1(ok3128)* animals expressing ChR2(H134R) in cholinergic neurons (*unc-17* promoter). Animals were optionally treated with ATR as indicated. Dense projections (DP), endosomes (E), dense core vesicles (blue arrows), SVs (black arrowheads), docked vesicles (white arrowheads) and large vesicles (LV) are indicated. Scale bars, 100 nm. **(B)** Violin plot depicting the number of SVs counted per synaptic profile. **(C)** Violin plot depicting the number of large endcytic vesicels and 'endosomes' per synapse. **(D)** Violin plot depicting the number of docked vesicles observed per synaptic profile. **(B - D)** Bold line represents the median, and the dashed lines the IQR. Kruskal-Wallis test. Only statistically significant differences are depicted. * $p < 0.05$,** $p < 0.01$, *** $p < 0.001$. Number of synaptic profiles imaged: wild type (-ATR) = 56, wild type (-ATR) = 51, *flwr-1* (-ATR) = 55, *flwr-1* (+ATR) = 59.

Fig. 7. Increased Ca^{2+} levels in *flwr-1* mutants may be caused by negative regulation of MCA-3.

(A) Schematic representation of the *mca-3* gene locus including exon/intron structure of isoforms *mca-3a* and *mca-3b*. Bars represent exons and connecting lines introns. The size of the *ok2048* deletion as well as the putative calmodulin-binding domain are indicated. **(B)** Mean (± SEM) normalized fluorescence in synaptic puncta of the DNC of animals expressing GCaMP6f and ChrimsonSA in cholinergic motor neurons (*unc-17b* promoter). All animals were supplemented with ATR. A 10 s light pulse (590 nm, 40 µW/mm^2) was applied after 5 s as indicated by the red shade. **(C)** Median (with IQR) normalized fluorescence during stimulation (seconds 6 to 14) as depicted in (B). Each dot indicates a single animal. Kruskal-Wallis test. Only statistically significant differences are depicted. ** $p < 0.01$, *** $p < 0.001$. Number of animals imaged in (B + C): wild type = 83, *flwr-1* = 58, *mca-3* = 50, *mca-3; flwr-1* = 44. Outliers were removed from all datasets

as detected by iterative Grubb's method (GraphPad Prism). **(D)** Mean (± SEM) fraction of moving animals after exposure to 1.5 mM aldicarb. Two-way ANOVA with Tukey's correction. ns not significant, *** $p < 0.001$.

Fig. 8. Basic amino acid residues on the intracellular surface of FLWR-1 may be involved in PI(4,5)P_2 lipid binding.

(A) Partial alignment of the amino acid sequences of FLWR-1, hFwe4 (*Homo sapiens*), and Fwe-Ubi (*Drosophila melanogaster*). Shading depicts evolutionary conservation of amino acid residues (black – identity; grey - homology). **(B)** Mean (± SEM) fraction of moving animals after exposure to 1.5 mM aldicarb. Two-way ANOVA with Tukey's correction. Selected comparisons are depicted. N = 3 biological replicates. *** $p < 0.001$. **(C)** Exemplary images of CCs in wild type and *flwr-1(ok3128)* animals expressing GFP fused to the PH-domain of PLCδin CCs. Scale bar, 10 µm. **(D)** Mean (± SEM) corrected GFP fluorescence. Membrane fluorescence was estimated by measuring the perimeter of CCs and subtracting the fluorescence in the interior of cells. Each dot indicates a single CC. a.u. = arbitrary units of fluorescence intensity. Kruskal-Wallis test. Only statistically significant differences are depicted. * $p < 0.05$, ** $p < 0.01$, *** $p < 0.001$. Number of animals imaged in N = 3 biological replicates: wild type = 27, *flwr-1* = 25.

Fig. 9. FLWR-1 is physically close to MCA-3 in the plasma membrane of BWMs and promotes synaptic localization of MCA-3.

(A) Schematic representation of the BiFC assay. **(B)** Representative micrographs of animals expressing FLWR-1 fused to one fragment of mVenus (VN173) and either MCA-3b, NRA-2/Nicalin or UNC-1 stomatin, interacting with gap junctions, respectively, fused to the other fragment of mVenus (VC155). Scale bar, 10 µm. **(C)** Representative micrographs of the DNC of animals expressing MCA-3b::YFP in cholinergic neurons (*unc-17* promoter). Scale bar, 5 µm. **(D, E)** Analysis of MCA-3b::YFP fluorescence (mean ± SEM) along the nerve cord (D) and as the ratio of fluorescence in synaptic puncta over fluorescence in the inter-puncta regions (E). Each dot represents a single animal. Number of animals imaged in N = 3 biological replicates: wild type = 35, *flwr-1* = 35. Unpaired t-test. ** $p < 0.001$.

Fig. 10. Model summarizing findings made in this study.

For details, see discussion.

SUPPLEMENTAL MATERIAL

Figure 1 – Figure supplement 1. Loss of FLWR-1 does not change body length or locomotion speed but reduces the number of living progeny.

(A) Mean (± SEM) body length of wild type and *flwr-1(ok3128)* mutants in mm. Unpaired t-test. ns not significant. Number of animals accumulated from N = 4 biological replicates: wild type = 29, *flwr-1* = 27. **(B)** Mean (± SEM) number of living progeny per animal. Unpaired t-test. ** $p < 0.01$. Number of animals accumulated from N = 4 biological replicates: wild type = 20, *flwr-1* = 18. **(C)** Mean (± SEM) crawling speed. N = 2 biological replicates.

Figure 1 – Figure supplement 2. FLWR-1 is predicted to be a tetraspan transmembrane protein and is transported by UNC-104 kinesin.

(A) Graphical representation of the results of DeepTMHMM prediction of membrane orientation of the FLWR-1 protein based on its amino acid sequence. The red shapes indicate the presence of four transmembrane domains. **(B)** Alphafold3 prediction of FLWR-1 protein structure. The coloring represents the calculated predicted local distance difference test (plDDT) as shown below the structure. Higher plDDT values indicate a higher confidence of correct prediction. **(C)** Heatmap plot depicting *flwr-1(F20D1.1)* single-cell RNAseq data generated by the CeNGEN database. Coloring indicates transcripts per million (TPM) per tissue normalized to the average expression as indicated in the legend. The size of the dots represents the percentage of cells of this cell type expressing the gene. **(D)** Mean (± SEM) swimming cycles of animals expressing ChR2(H134R) in cholinergic motor neurons (*unc-17* promoter). All animals were treated with ATR. A 90 s light pulse (470 nm, 1 mW/mm^2) was applied after 30 s as indicated by the blue shade. Number of animals accumulated from N = 2 biological replicates: wild type = 63 – 99, *flwr-1* = 48 – 66, GFP::FLWR-1 rescue = 37 – 52. **(E)** Statistical analysis of swimming speed at different time points as depicted in (D). Mean (± SEM). Each dot represents a single animal. Mixed-effects model analysis with Tukey's correction. Only statistically significant differences are depicted. *** $p < 0.001$. **(F)** Example images depicting GFP::FLWR-1 fluorescence in nerve ring and nerve cords in wild type and *unc-104(e1265)* mutants. Scale bar, 20 µm.

Figure 1 – Figure supplement 3. FLWR-1 expression in body wall muscle cells partially rescues aldicarb resistance of *flwr-1* mutants, but aldicarb resistance is not affected through AChRs.

(A) Mean (± SEM) fraction of moving animals after exposure to 0.25 mM levamisole. N = 3 biological replicates. Two-way ANOVAs with Tukey's correction. No significant differences were found. **(B)** Mean (± SEM) fraction of moving animals after exposure to 1.5 mM aldicarb. FLWR-1 is optionally expressed in BWMs (*pmyo-3*) only or combined with expression in cholinergic (*punc-17*) or GABAergic (*punc-47*) neurons in a *flwr-1(ok3128)* mutant background. N = 3 - 8 biological replicates. Two-way ANOVAs with Tukey's correction. Only non-significant differences are depicted. For all other comparisons $p < 0.001$. (**C)** Mean (± SEM) fraction of moving animals after exposure to 0.5 mM aldicarb, compared in wild type, *flwr-1(ok3128)*, *acr-16(ok789)* and *flwr-1; acr-16* double mutants. N = 3 biological replicates. Two-way ANOVAs with Tukey's correction. **(D)** Loss of GABAergic transmission conveys aldicarb hypersensitivity in *flwr-1* mutants. Mean (± SEM) fraction of moving animals after exposure to 0.1 mM aldicarb. N = 3 biological replicates.

Figure 3 – Figure supplement 1. FLWR-1 localizes to cholinergic and GABAergic active zones.

(A) Line scan analysis of colocalization of GFP::FLWR-1 and TagRFP::ELKS-1 along the DNC as represented in the same order in **Fig. 3B**. R^2 as determined by Pearson correlation. a.u. = arbitrary units of fluorescence intensity. **(B)** Line scan analysis of colocalization of GFP::FLWR-1 and TagRFP::ELKS-1 along the DNC as represented in the micrographs in the same order in **Fig. 3C**. R^2 as determined by Pearson correlation. a.u. = arbitrary units of fluorescence intensity. **(A + B)** Examples for fluorescent puncta which contain either both, FLWR-1 and ELKS-1 (blue arrowheads), or only FLWR-1 (red arrowheads) are indicated. The same puncta are indicated in the respective micrographs in Fig. 3B + C. **(C)** Comparison of Pearson correlation coefficients of line scans along DNCs represented in **Fig. 3**. Mean (± SEM). Unpaired t-test.

Figure 4 – Figure supplement 1. Basal SNG-1::pHluorin fluorescence and cell surface fraction are unchanged in *flwr-1* mutants.

(A) Mean (± SEM) pHluorin fluorescence before stimulation as depicted in Fig. 5. Number of animals imaged in N = 5 biological replicates: wild type = 27, *flwr-1* = 32. Unpaired t-test. ns not significant $p > 0.05$. **(B)** Representative images of a primary neuronal cell expressing SNG-1::pHluorin when exposed to different buffers as indicated. Scale bar, 5 µm.

(C) Number of cells imaged in N = 2 biological replicates: wild type = 29, *flwr-1* = 23. Unpaired t-test. ns not significant $p > 0.05$.

Figure 5 – Figure supplement 1. *flwr-1* mutants show defecting cholinergic neurotransmission only during continuous stimulation.

(A, B) Mean (± SEM) mPSC frequency and amplitude, respectively, before stimulation. Unpaired t-test. ns not significant. Number of animals: wild type = 16, *flwr-1* = 14. **(C)** Mean (± SEM) inward currents of BWMs recordings induced by 10 ms light pulses (470 nm, 8 mW/mm^2) applied every 2 s (0.5 Hz). Two-way ANOVA with Šidák's correction for multiple comparisons. ns not significant. Number of animals: wild type = 9, *flwr-1* = 8. **(D)** As in (C), but 2Hz stimulation. ns not significant. Number of animals: wild type = 7, *flwr-1* = 7. **(E)** Representative voltage-clamp recording of currents detected in BWMs. This wild type animal expresses ChR2(H134R) in cholinergic motor neurons (*unc-17* promoter) and has been treated with ATR. A 30 s light stimulus (470 nm, 8 mW/mm^2) as well as a 10 ms pulse after a 15 s inter-stimulus interval (ISI) were applied as indicated by blue bars. **(F)** Mean (± SEM) mPSC frequency in BWMs of animals expressing ChR2(H134R) in cholinergic motor neurons (*unc-17* promoter). All animals have been treated with ATR. A 30 s light pulse (470 nm, 8 mW/mm^2) was applied as indicated by blue shade. **(G)** Mean (± SEM) mPSC frequency during 30 s stimulation. Unpaired t-test. ** $p < 0.01$. **(H)** Analysis of the amplitude of the first peak during 30 s photostimulation and the second peak after 15 s ISI as indicated in (E). Two-way ANOVA with Tukey's correction for multiple comparisons. ns not significant, *** $p < 0.001$. (F - H) Number of animals: wild type = 9, *flwr-1* = 8.

Figure 6 – Figure supplement 1. *flwr-1* mutants have a normal numbers of dense core vesicles before and after stimulation.

Violin plot depicting the number of dense core vesicles counted per synaptic profile. Bold line represents the median and the dashed lines the IQR. Kruskal-Wallis test. ns not significant. Number of synaptic profiles imaged: wild type (-ATR) = 56, wild type (-ATR) = 51, *flwr-1* (-ATR) = 55, *flwr-1* (+ATR) = 59.

Figure 7 – Figure supplement 1. Comparison of *flwr-1* and *mca-3* expression by single-cell RNAseq data.

(A) Heatmap plot depicting *flwr-1(F20D1.1)* and *mca-3* single-cell RNAseq data generated by the CeNGEN database (https://cengen.shinyapps.io/CengenApp/). Coloring indicates transcripts per million (TPM) per tissue normalized to the average expression as indicated in the legend. The size of the dots represents the percentage of cells of this cell type expressing the gene. Coelomocyte data is highlighted by the blue box. **(B)** Mean (± SEM) fraction of moving animals after exposure to 1.5 mM aldicarb. MCA-3b is expressed in GABAergic neurons of *flwr-1(ok3128)* mutant animals (*unc-47* promoter). Two-way ANOVA with Tukey's correction. N = 3 biological replicates. ns not significant $p > 0.05$, *** $p < 0.001$.

Figure 8 – Figure supplement 1. Structural analysis of important amino acid residues in FLWR-1 and other proteins.

(A) Top view of an Alphafold3 prediction of a tetrameric FLWR-1 structure. Glutamate 74 is indicated as colored spheres in each monomer. **(B)** Cryo-EM structure of the human L-type voltage-gated calcium channel $Ca_v1.2$ (PDB: 8EOG) (Chen et al., 2023). Glutamate residues in the central pore are indicated as spheres. Ca^{2+} ions within the pore are depicted as turquoise spheres. **(C)** X-Ray structure of the Kir2.2 potassium channel in a complex with $PI(4,5)P_2$ (PDB: 3SPI) (Hansen et al., 2011). Basic amino acid residues in the proximity of $PI(4,5)P_2$ are depicted as sticks. **(D)** $PI(4,5)P_2$ was docked to the Alphafold3 structure of FLWR-1 using AutoDock Vina (Eberhardt et al., 2021). Basic amino acid residues in the proximity of $PI(4,5)P_2$ are depicted as sticks. Arginine 27 and lysine 31 are indicated.

Figure 9 – Figure supplement 1. Expression of FLWR-1 and MCA-3b for BiFC does not affect locomotion behavior: Mean (± SEM) swimming cycles of animals analyzed by BiFC as depicted in Fig. 8B. N2 wild type animals were used as a control strain, as well as *flwr-1(ok3128)* and *mca-3(ok2048)* mutants. Number of animals accumulated from N = 4 (wild type) or N = 2 (all other strains) biological replicates: wild type = 90, FLWR-1/MCA-3b = 16, FLWR-1/NRA-2 = 29, *flwr-1* = 40, *mca-3* = 42 . One-way ANOVA with Tukey's correction. ns not significant $p > 0.05$, *** $p < 0.001$.

Additional Files

Table S1: Plasmids used in this study.

Table S2: Strains used in this study.

Table S3: CeNGEN expression data of *flwr-1/F20D1.1* and *mca-3*

Single-cell RNAseq data as described in Taylor et al. (2021). The threshold was set to "All Cells Unfiltered". Cell types were sorted alphabetically. Where CeNGEN did not produce any results, cells were left blank.

Movie S1.
Time series of a particle containing GFP::FLWR-1 and mCherry::SNB-1 travelling along commissures. Scale bar, 2 µm.

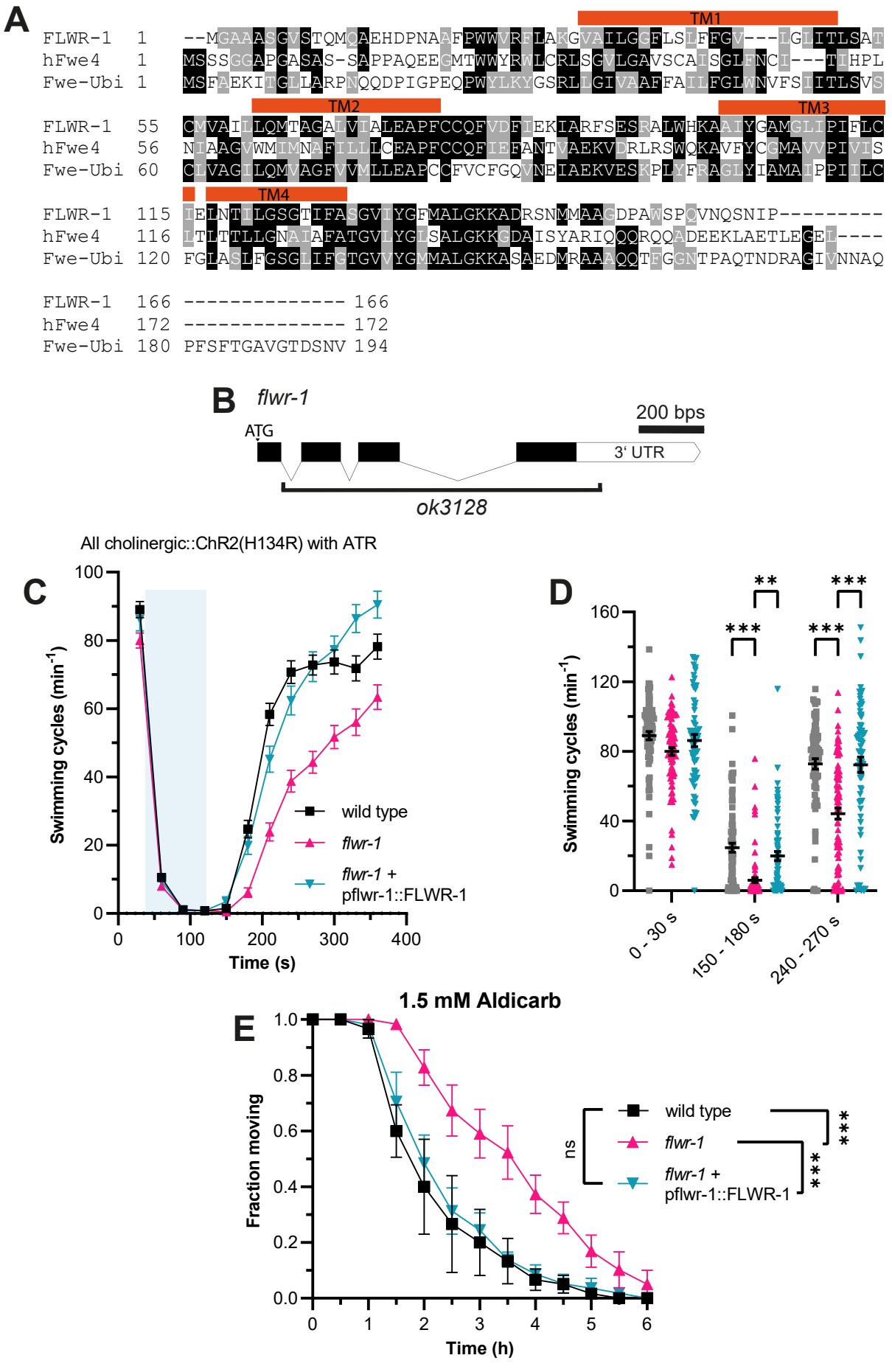
A
TM1
FLWR-1 1 --MGAAASGVSTQMQAEHDPNAAFPWWVRFLAKGVAILGGFLSLFFGV---LGLITLSAT
hFwe4 1 MSSSGGAPGASAS-SAPPAQEEGMTWWYRWLCRLSGVLGAVSCAISGLFNCI---TIHPL
Fwe-Ubi 1 MSFAEKITGLLARPNQQDPIGPEQPWYLKYGSRLIGIVAAFFAILFGLWNVFSIITLSVS
TM2
TM3
FLWR-1 55 CMVAILLQMTAGALVIALEAPFCCQFVDFIEKIARFSESRALWHKAAIYGAMGLIPIFLC
hFwe4 56 NIAAGVWMIMNAFILLLCEAPFCCQFIEFANTVAEKVDRLRSWQKAVFYCGMAVVPIVIS
Fwe-Ubi 60 CLVAGILQMVAGFVVMLLEAPCCFVCFGQVNEIAEKVESKPLYFRAGLYIAMAIPPIILC
TM4
FLWR-1 115 IELNTILGSGTIFASGVIYGFMALGKKADRSNMMAAGDPAWSPQVNQSNIP---------
hFwe4 116 LTLTTLLGNAIAFATGVLYGLSALGKKGDAISYARIQQQRQQADEEKLAETLEGEL----
Fwe-Ubi 120 FGLASLFGSGLIFGTGVVYGMMALGKKASAEDMRAAAQQTFGGNTPAQTNDRAGIVNNAQ
FLWR-1 166 ---------- 166
hFwe4 172 ---------- 172
Fwe-Ubi 180 PFSFTGAVGTDSNV 194
B
flwr-1
200 bps
ATG
3' UTR
ok3128
All cholinergic::ChR2(H134R) with ATR
C
Swimming cycles (min-1)
Time (s)
wild type
flwr-1
flwr-1 +
pflwr-1::FLWR-1
D
Swimming cycles (min-1)
0 - 30 s
150 - 180 s
240 - 270 s
1.5 mM Aldicarb
E
Fraction moving
Time (h)
wild type
flwr-1
flwr-1 +
pflwr-1::FLWR-1
ns

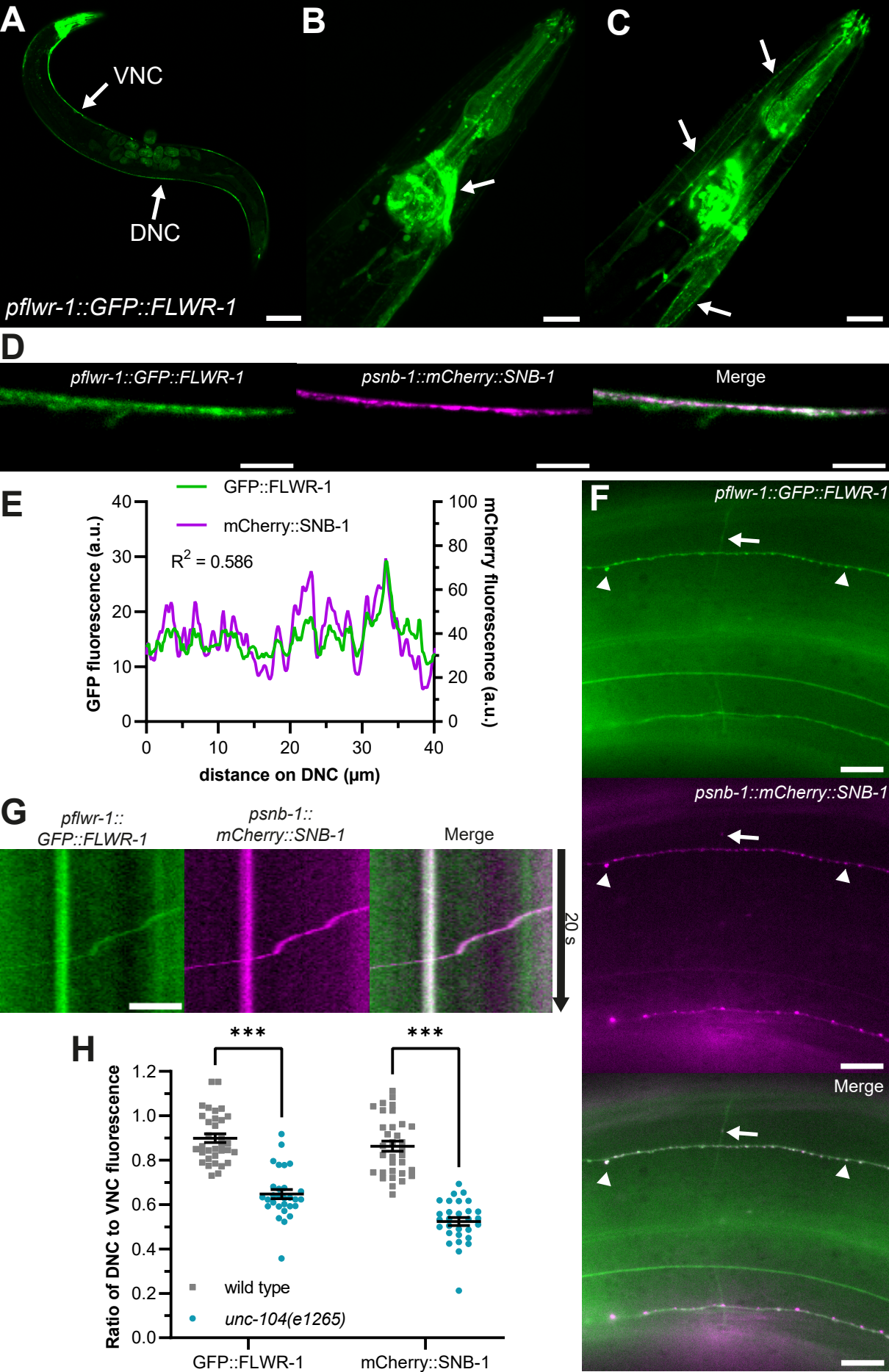
A
VNC
DNC
pflwr-1::GFP::FLWR-1
B
C
D
pflwr-1::GFP::FLWR-1
psnb-1::mCherry::SNB-1
Merge
E
GFP::FLWR-1
mCherry::SNB-1
R2 = 0.586
GFP fluorescence (a.u.)
mCherry fluorescence (a.u.)
distance on DNC (µm)
F
pflwr-1::GFP::FLWR-1
psnb-1::mCherry::SNB-1
Merge
G
pflwr-1::
GFP::FLWR-1
psnb-1::
mCherry::SNB-1
Merge
20 s
H
***
***
Ratio of DNC to VNC fluorescence
wild type
unc-104(e1265)
GFP::FLWR-1
mCherry::SNB-1

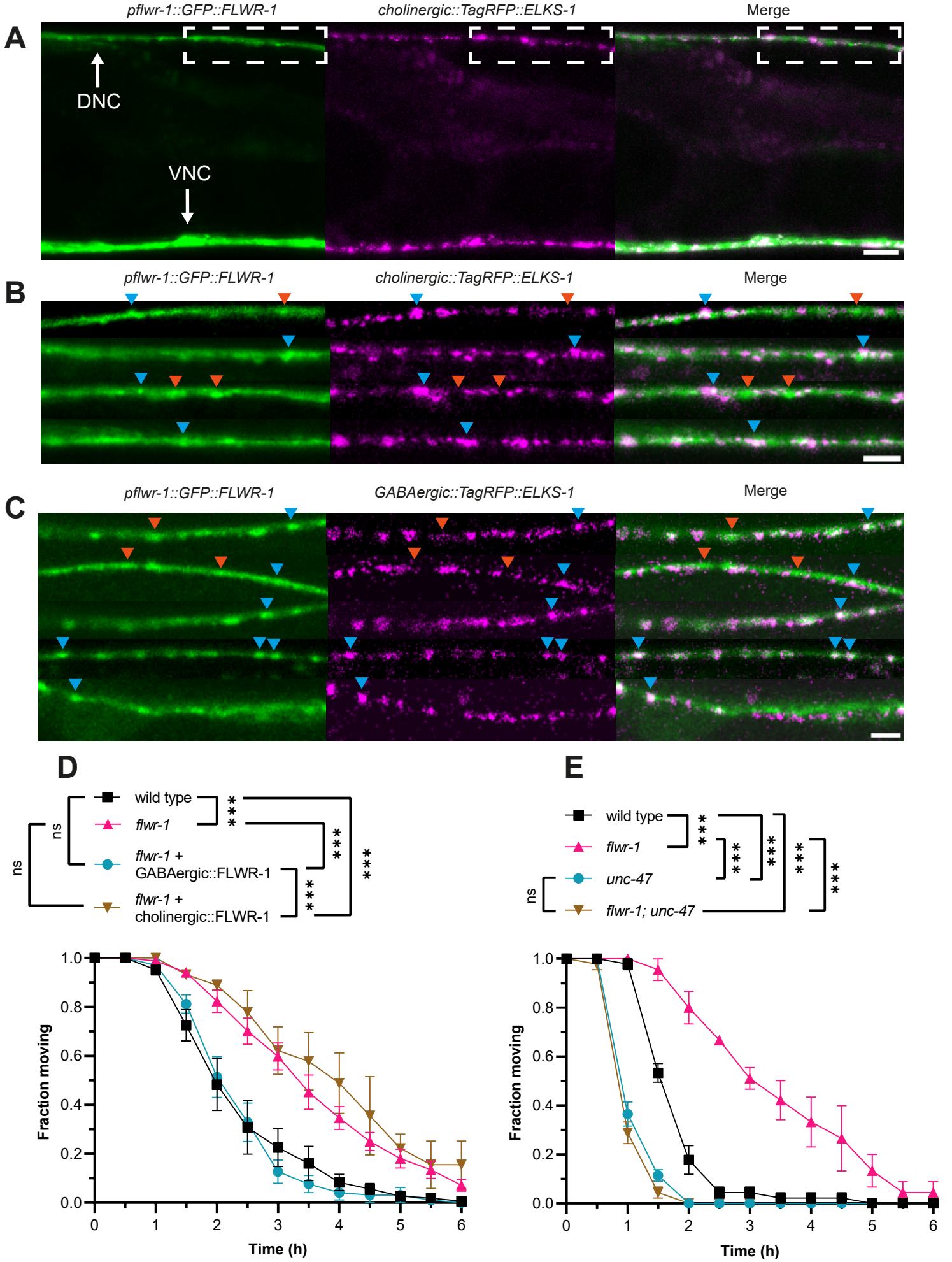
A
pflwr-1::GFP::FLWR-1
cholinergic::TagRFP::ELKS-1
Merge
DNC
VNC
B
pflwr-1::GFP::FLWR-1
cholinergic::TagRFP::ELKS-1
Merge
C
pflwr-1::GFP::FLWR-1
GABAergic::TagRFP::ELKS-1
Merge
D
wild type
flwr-1
flwr-1 + GABAergic::FLWR-1
flwr-1 + cholinergic::FLWR-1
ns
***
Fraction moving
Time (h)
E
wild type
flwr-1
unc-47
flwr-1; unc-47
ns
***
Fraction moving
Time (h)

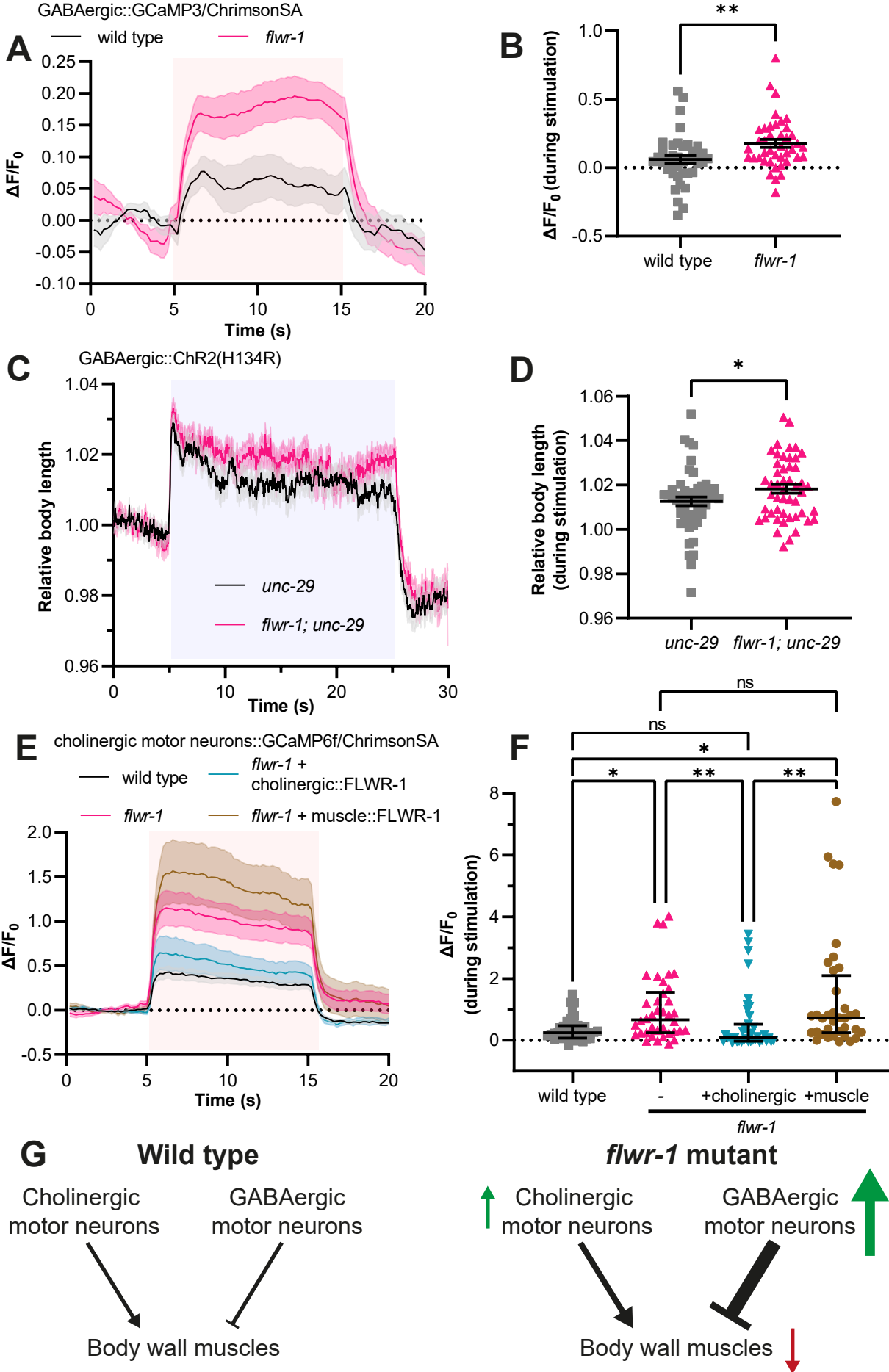
A
GABAergic::GCaMP3/ChrimsonSA
wild type
flwr-1
ΔF/F0
Time (s)
B
**
ΔF/F0 (during stimulation)
wild type
flwr-1
C
GABAergic::ChR2(H134R)
Relative body length
unc-29
flwr-1; unc-29
Time (s)
D
*
Relative body length (during stimulation)
unc-29
flwr-1; unc-29
E
cholinergic motor neurons::GCaMP6f/ChrimsonSA
wild type
flwr-1
flwr-1 + cholinergic::FLWR-1
flwr-1 + muscle::FLWR-1
ΔF/F0
Time (s)
F
ns
ns
*
*
**
**
ΔF/F0 (during stimulation)
wild type
-
+cholinergic
+muscle
flwr-1
G
Wild type
Cholinergic motor neurons
GABAergic motor neurons
Body wall muscles
flwr-1 mutant
Cholinergic motor neurons
GABAergic motor neurons
Body wall muscles

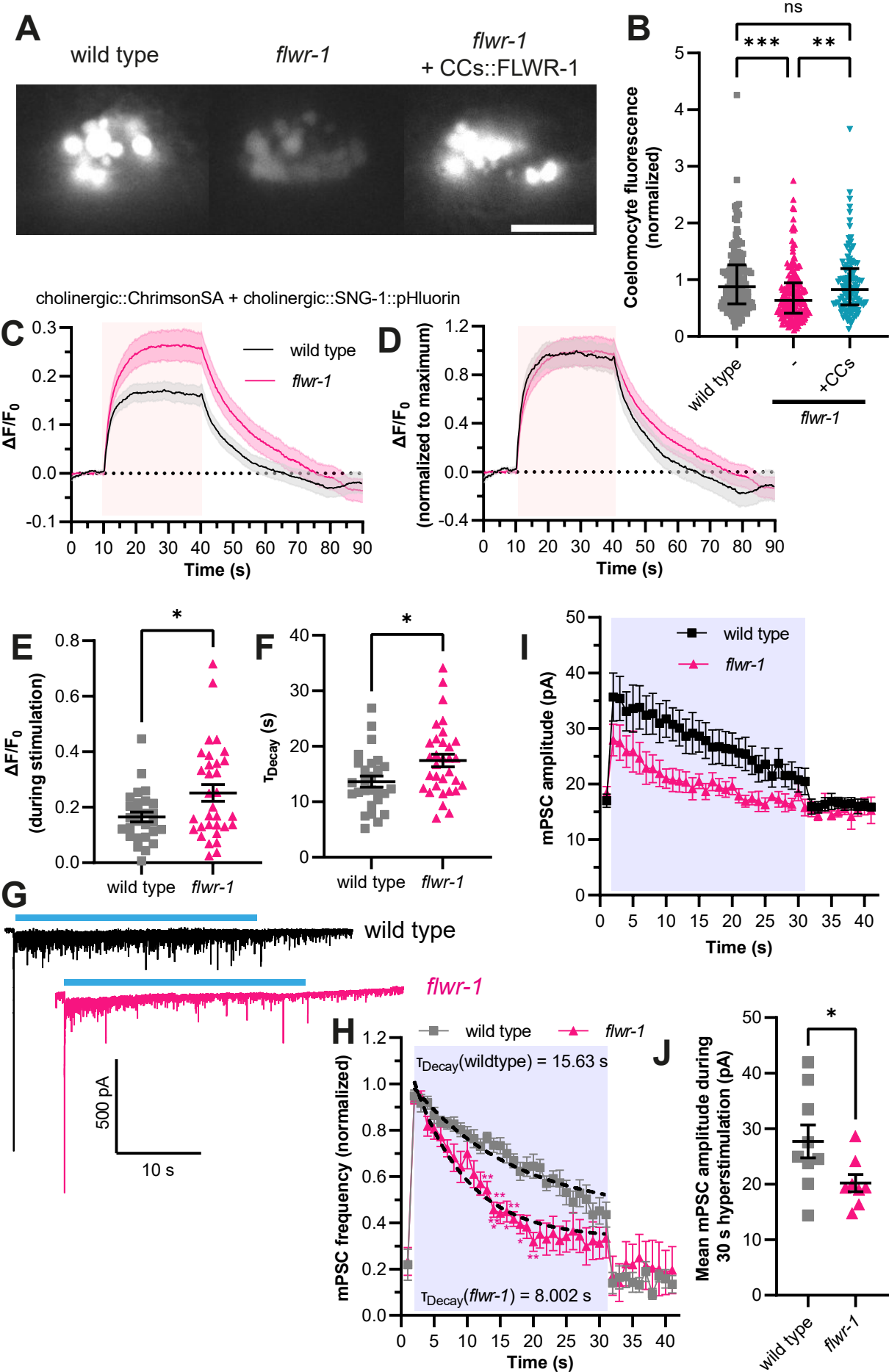
A
wild type
flwr-1
flwr-1
+ CCs::FLWR-1
B
ns
***
**
Coelomocyte fluorescence (normalized)
wild type
-
+CCs
flwr-1
cholinergic::ChrimsonSA + cholinergic::SNG-1::pHluorin
C
wild type
flwr-1
ΔF/F0
Time (s)
D
ΔF/F0 (normalized to maximum)
Time (s)
E
*
ΔF/F0 (during stimulation)
wild type
flwr-1
F
*
τDecay (s)
wild type
flwr-1
I
wild type
flwr-1
mPSC amplitude (pA)
Time (s)
G
wild type
flwr-1
500 pA
10 s
H
wild type
flwr-1
τDecay(wildtype) = 15.63 s
τDecay(flwr-1) = 8.002 s
mPSC frequency (normalized)
Time (s)
J
*
Mean mPSC amplitude during 30 s hyperstimulation (pA)
wild type
flwr-1

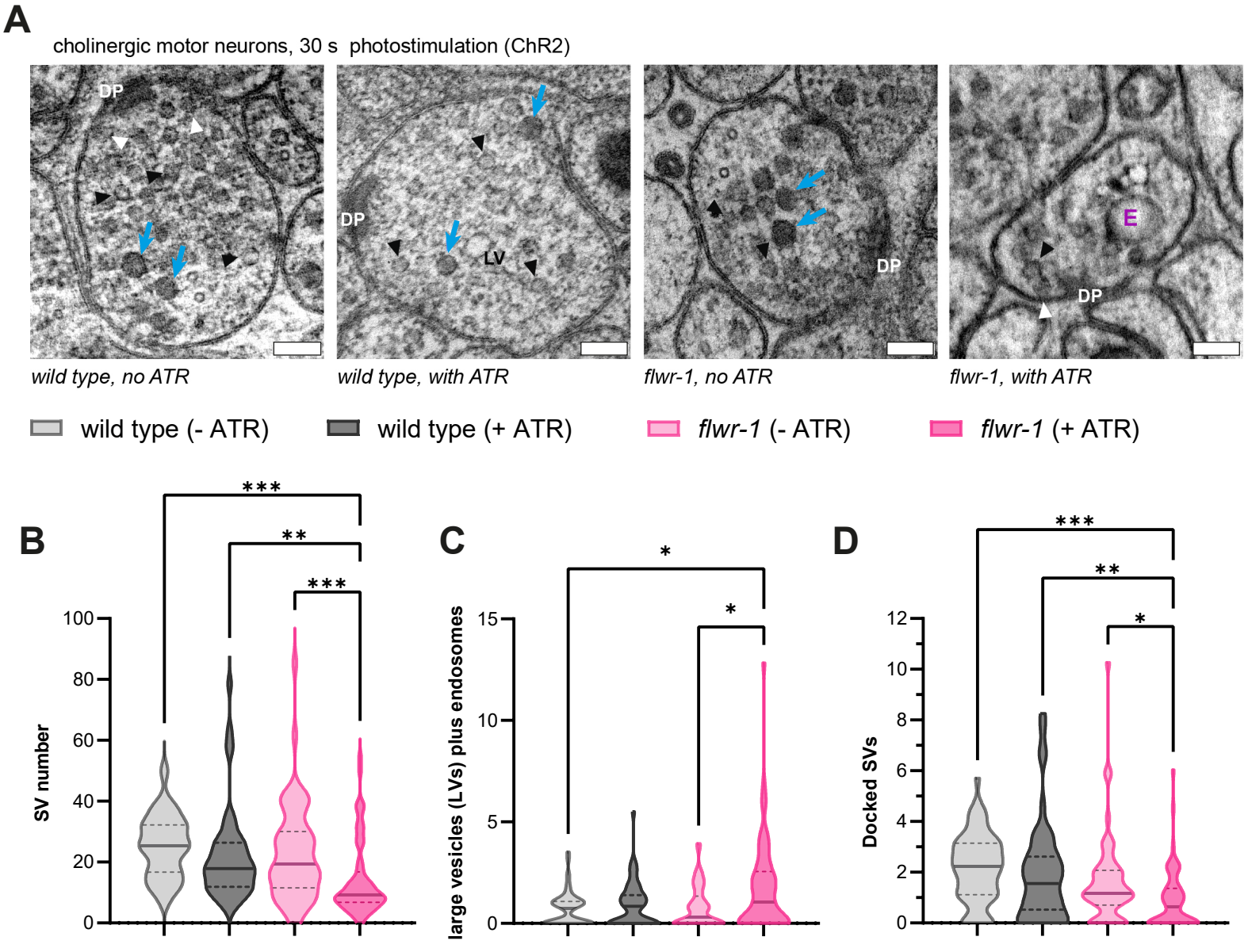
A
cholinergic motor neurons, 30 s photostimulation (ChR2)
DP
DP
LV
DP
E
DP
wild type, no ATR
wild type, with ATR
flwr-1, no ATR
flwr-1, with ATR
wild type (- ATR)
wild type (+ ATR)
flwr-1 (- ATR)
flwr-1 (+ ATR)
B
SV number
C
large vesicles (LVs) plus endosomes
D
Docked SVs

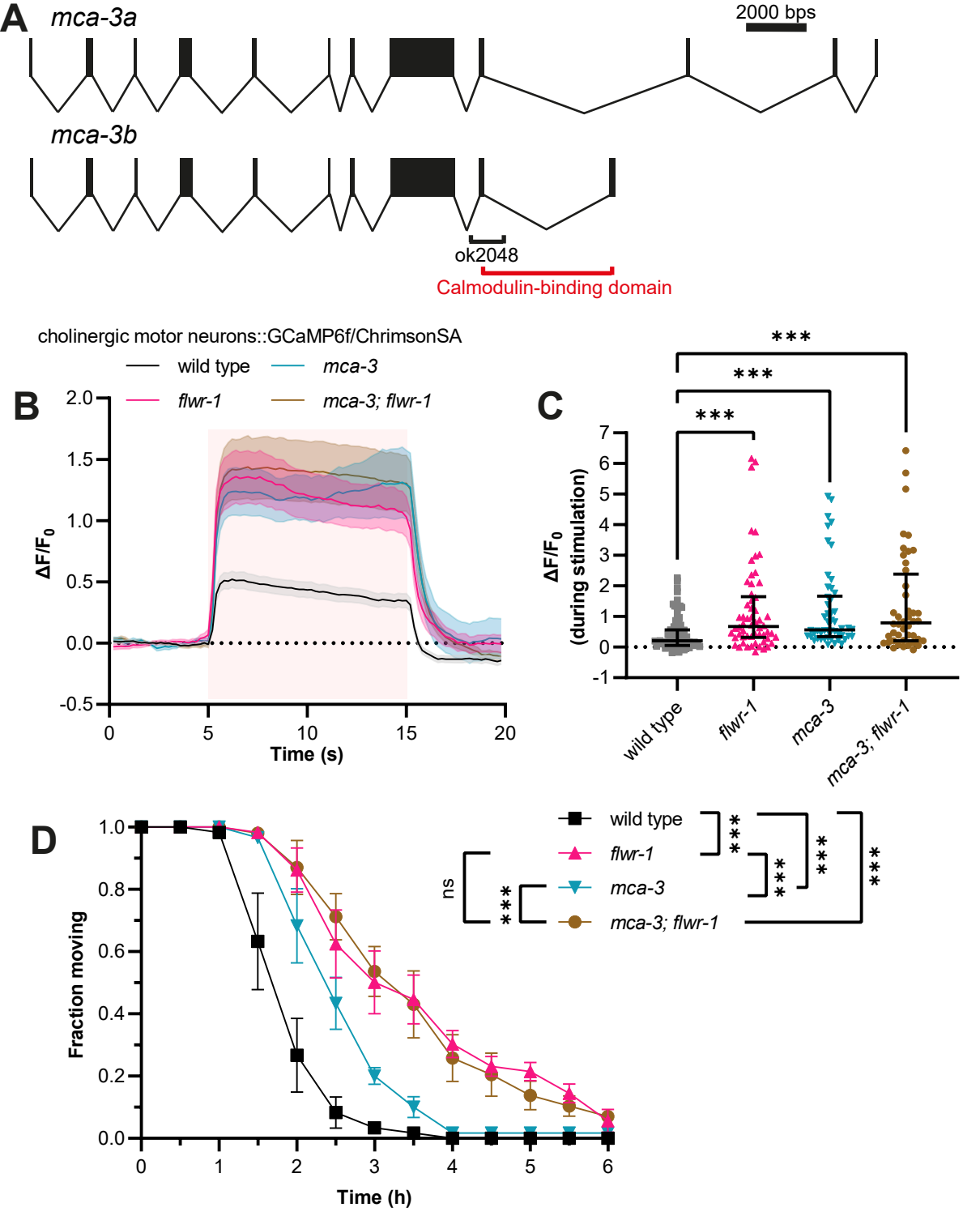
A
mca-3a
2000 bps
mca-3b
ok2048
Calmodulin-binding domain
cholinergic motor neurons::GCaMP6f/ChrimsonSA
wild type
mca-3
flwr-1
mca-3; flwr-1
B
ΔF/F0
Time (s)
C
ΔF/F0 (during stimulation)
***
wild type
flwr-1
mca-3
mca-3; flwr-1
D
Fraction moving
Time (h)
ns
***

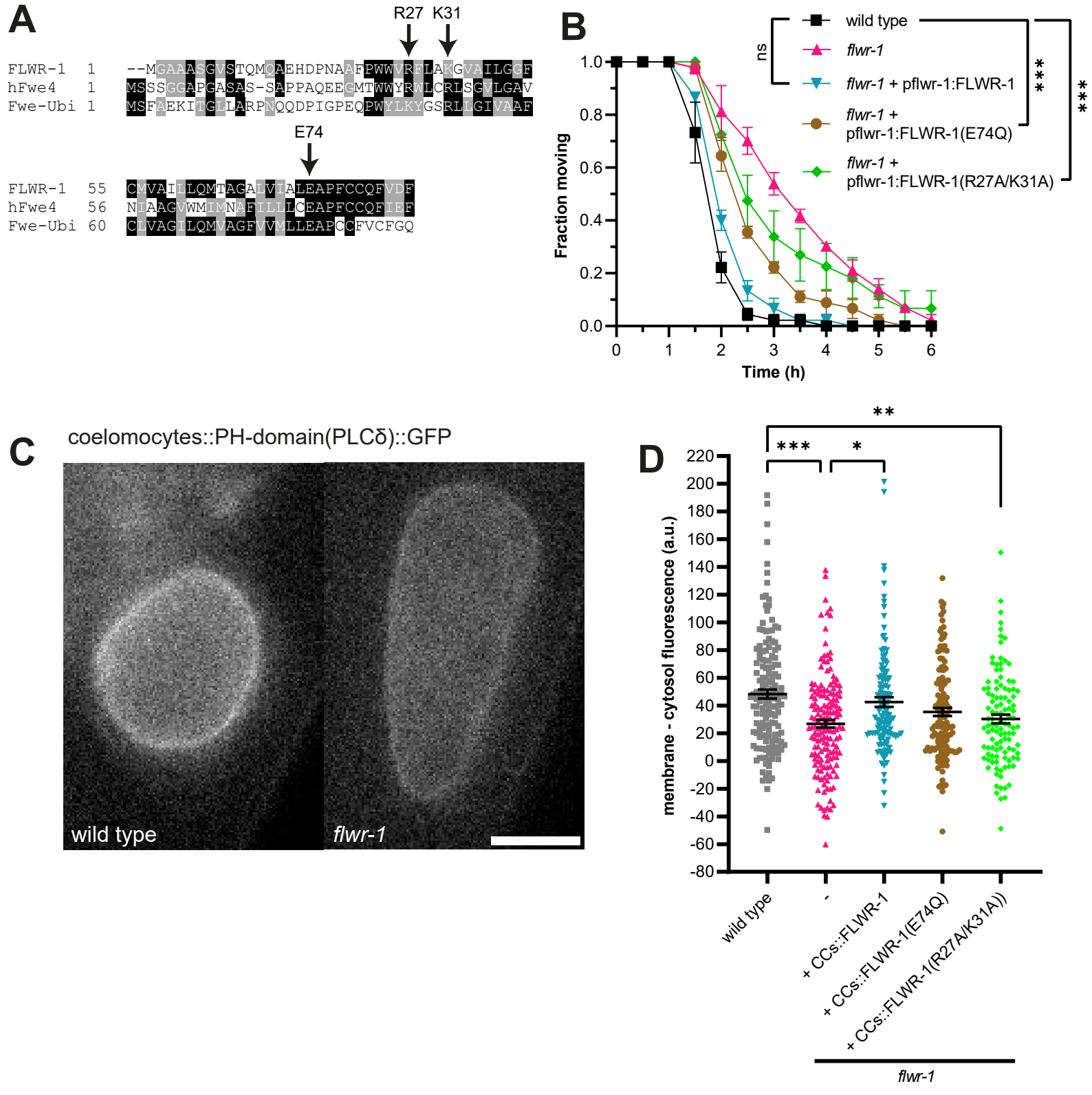
A
R27
K31
FLWR-1 1 --MGAAASGVSTQMQAEHDPNAAFPWWVRFLAKGVAILGGF
hFwe4 1 MSSSGGAPGASAS-SAPPAQEEGMTWWYRWLCRLSGVLGAV
Fwe-Ubi 1 MSFAEKIIGILARPNQQDPIGPEQPWYLKYGSRLLGIVAAF
E74
FLWR-1 55 CMVAIILQMTAGATVIALEAPFCCQFVDF
hFwe4 56 NIAAGVWMINNAFILLLCEAPFCCQFIEF
Fwe-Ubi 60 CLVAGILQMVAGFVVMLLEAPCCFVCFGQ
B
wild type
flwr-1
flwr-1 + pflwr-1:FLWR-1
flwr-1 + pflwr-1:FLWR-1(E74Q)
flwr-1 + pflwr-1:FLWR-1(R27A/K31A)
ns
***
***
Fraction moving
Time (h)
C
coelomocytes::PH-domain(PLCδ)::GFP
wild type
flwr-1
D
**
***
*
membrane - cytosol fluorescence (a.u.)
wild type
-
+ CCs::FLWR-1
+ CCs::FLWR-1(E74Q)
+ CCs::FLWR-1(R27A/K31A))
flwr-1

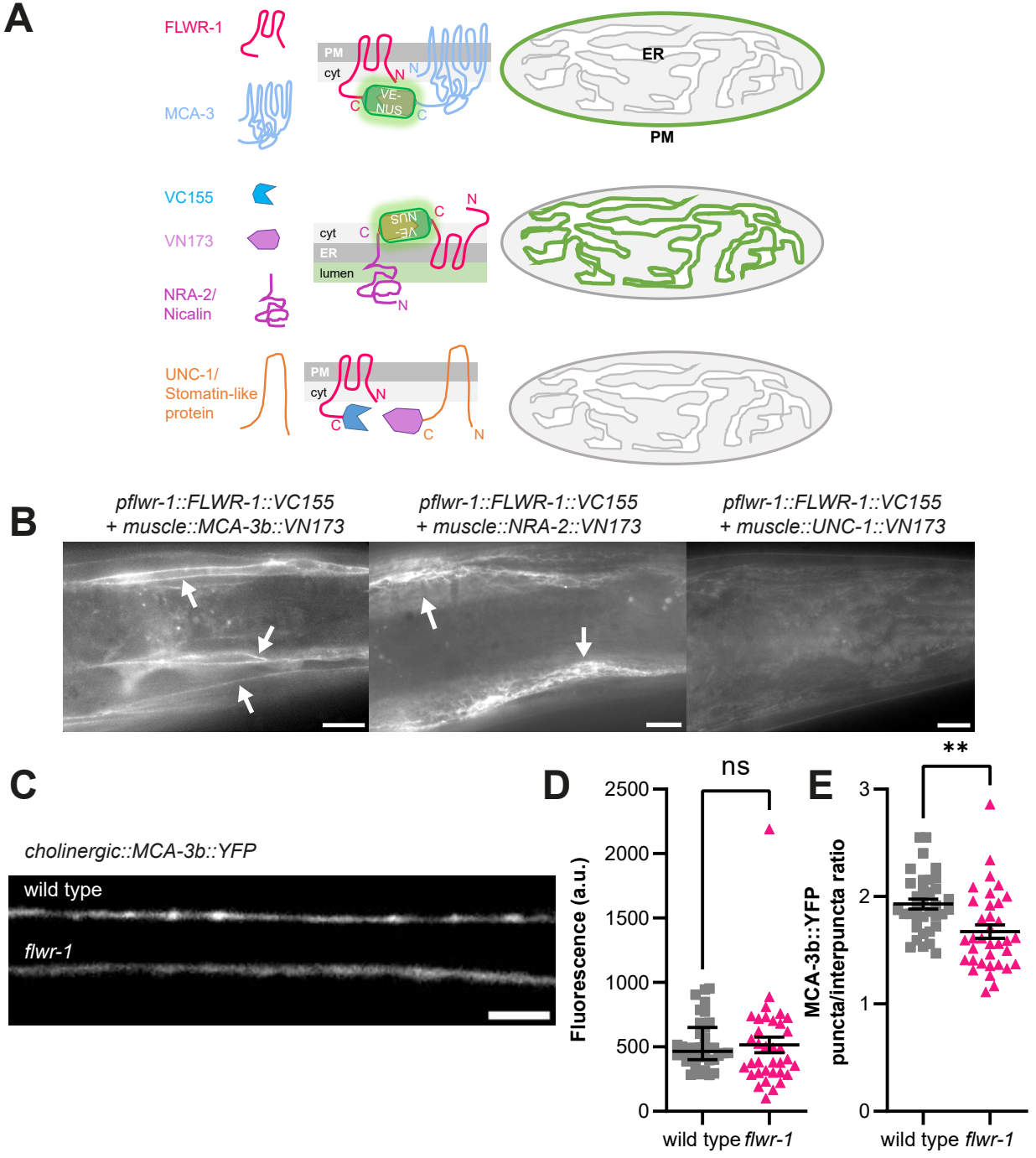
A
FLWR-1
MCA-3
PM
cyt
N
C
VE-
NUS
ER
PM
VC155
VN173
cyt
ER
lumen
NRA-2/
Nicalin
UNC-1/
Stomatin-like
protein
B
pflwr-1::FLWR-1::VC155
+ muscle::MCA-3b::VN173
pflwr-1::FLWR-1::VC155
+ muscle::NRA-2::VN173
pflwr-1::FLWR-1::VC155
+ muscle::UNC-1::VN173
C
cholinergic::MCA-3b::YFP
wild type
flwr-1
D
ns
Fluorescence (a.u.)
2500
2000
1500
1000
500
0
wild type
flwr-1
E
**
MCA-3b::YFP
puncta/interpuncta ratio
3
2
1
0
wild type
flwr-1

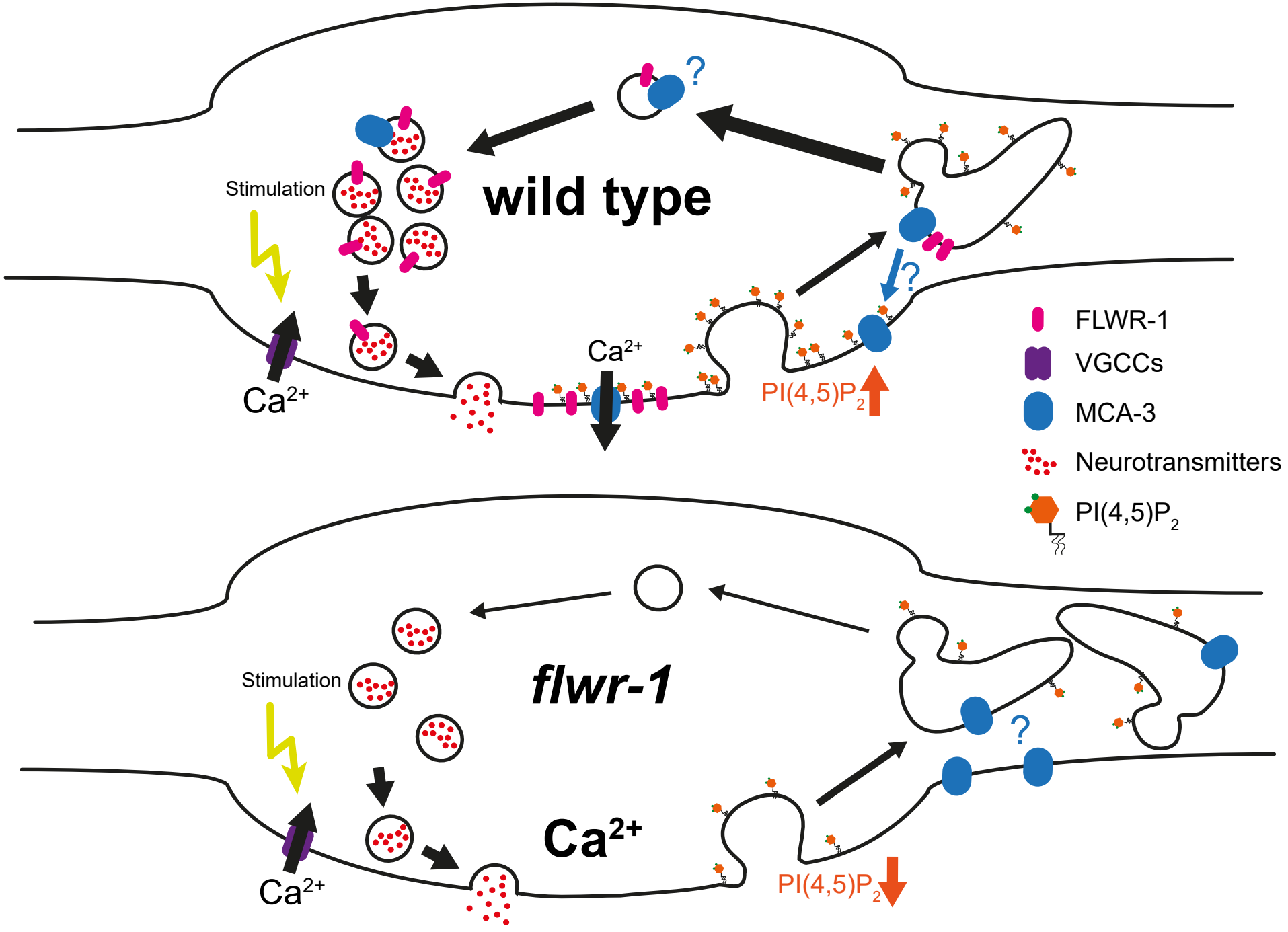
wild type
Stimulation
Ca2+
Ca2+
PI(4,5)P2
?
?
FLWR-1
VGCCs
MCA-3
Neurotransmitters
PI(4,5)P2
flwr-1
Stimulation
Ca2+
Ca2+
PI(4,5)P2
?

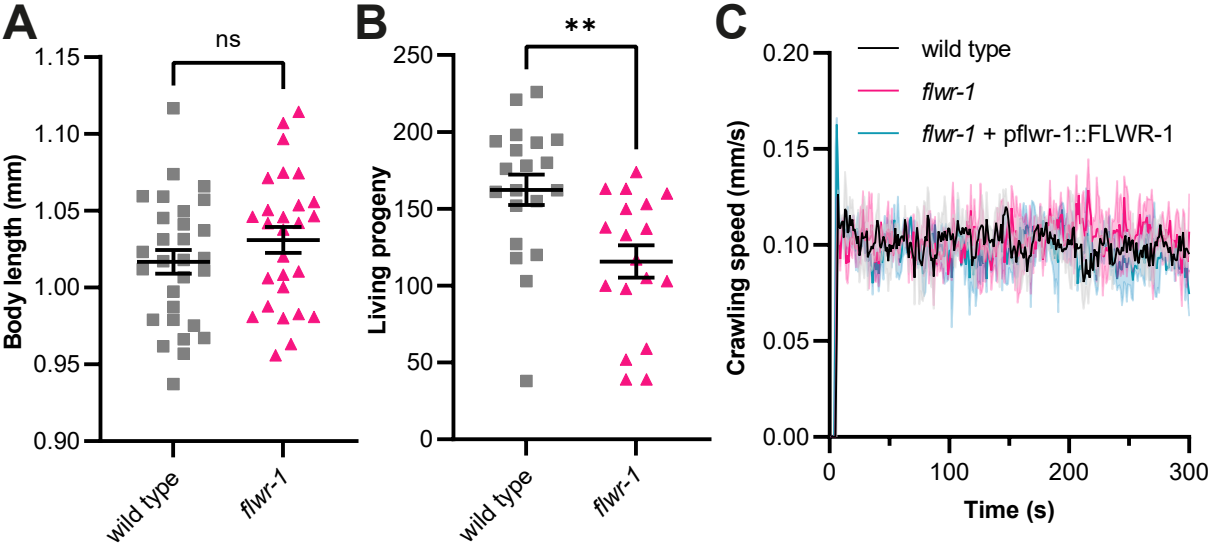
A
ns
Body length (mm)
1.15
1.10
1.05
1.00
0.95
0.90
wild type
flwr-1
B
**
Living progeny
250
200
150
100
50
0
wild type
flwr-1
C
wild type
flwr-1
flwr-1 + pflwr-1::FLWR-1
Crawling speed (mm/s)
0.20
0.15
0.10
0.05
0.00
0
100
200
300
Time (s)

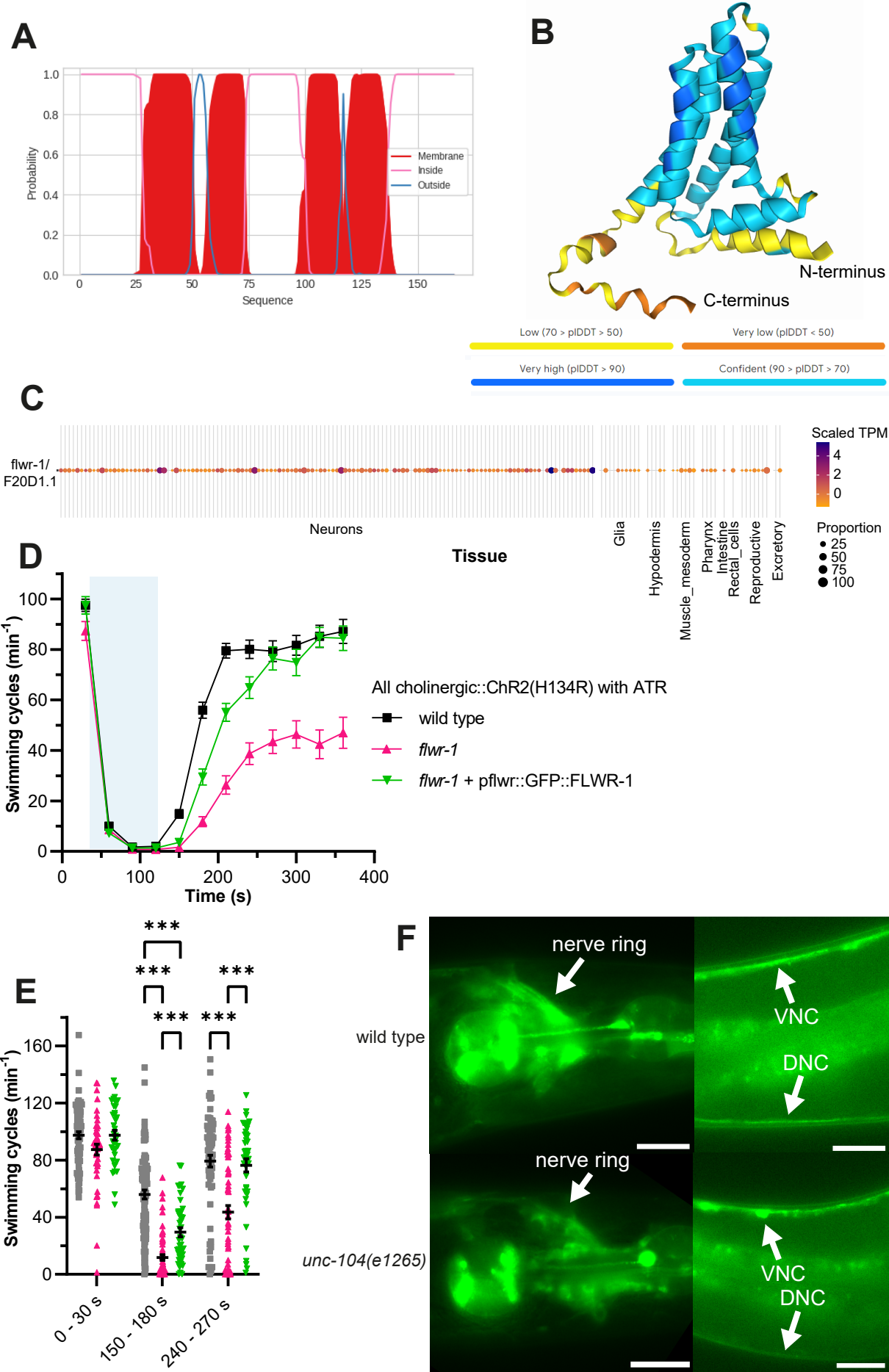
A
Probability
Sequence
Membrane
Inside
Outside
B
N-terminus
C-terminus
Low (70 > pIDDT > 50)
Very low (pIDDT < 50)
Very high (pIDDT > 90)
Confident (90 > pIDDT > 70)
C
flwr-1/
F20D1.1
Scaled TPM
Proportion
Neurons
Glia
Hypodermis
Muscle_mesoderm
Pharynx
Intestine
Rectal_cells
Reproductive
Excretory
Tissue
D
Swimming cycles (min-1)
Time (s)
All cholinergic::ChR2(H134R) with ATR
wild type
flwr-1
flwr-1 + pflwr::GFP::FLWR-1
E
Swimming cycles (min-1)
0 - 30 s
150 - 180 s
240 - 270 s
F
wild type
unc-104(e1265)
nerve ring
VNC
DNC

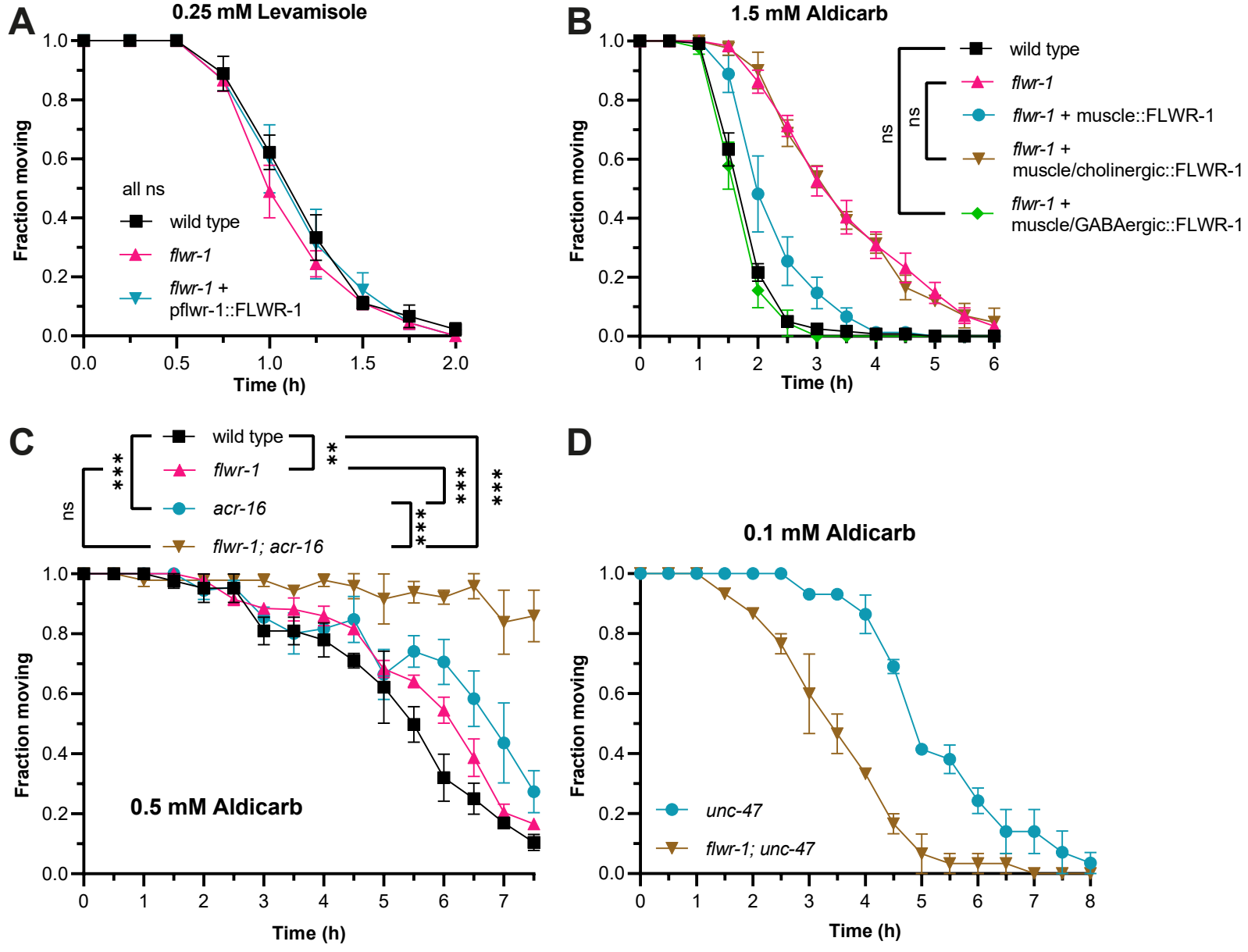
A
0.25 mM Levamisole
Fraction moving
Time (h)
all ns
wild type
flwr-1
flwr-1 +
pflwr-1::FLWR-1
B
1.5 mM Aldicarb
Fraction moving
Time (h)
ns
ns
wild type
flwr-1
flwr-1 + muscle::FLWR-1
flwr-1 +
muscle/cholinergic::FLWR-1
flwr-1 +
muscle/GABAergic::FLWR-1
C
wild type
flwr-1
acr-16
flwr-1; acr-16
ns
***
**
***
***
***
0.5 mM Aldicarb
Fraction moving
Time (h)
D
0.1 mM Aldicarb
Fraction moving
Time (h)
unc-47
flwr-1; unc-47

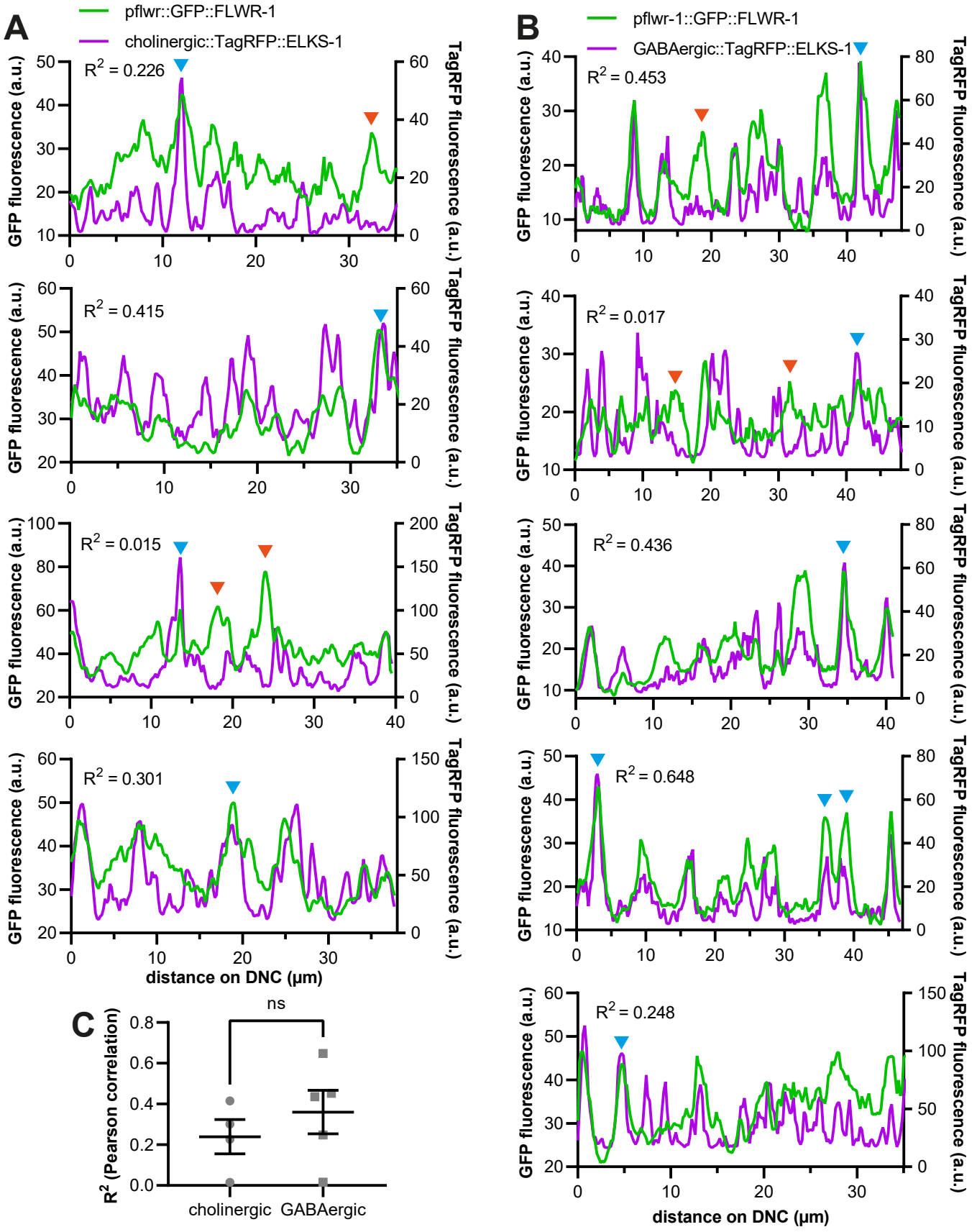
A
pflwr::GFP::FLWR-1
cholinergic::TagRFP::ELKS-1
R2 = 0.226
R2 = 0.415
R2 = 0.015
R2 = 0.301
GFP fluorescence (a.u.)
TagRFP fluorescence (a.u.)
distance on DNC (µm)
B
pflwr-1::GFP::FLWR-1
GABAergic::TagRFP::ELKS-1
R2 = 0.453
R2 = 0.017
R2 = 0.436
R2 = 0.648
R2 = 0.248
GFP fluorescence (a.u.)
TagRFP fluorescence (a.u.)
distance on DNC (µm)
C
ns
R2 (Pearson correlation)
cholinergic
GABAergic

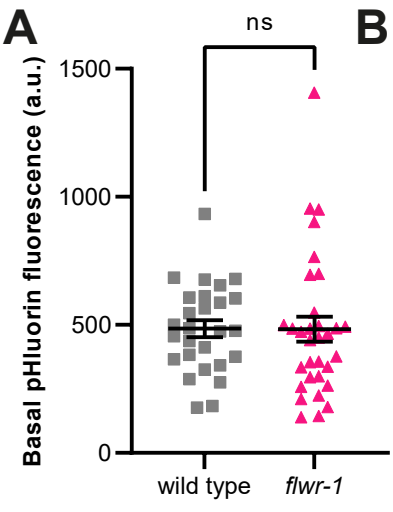

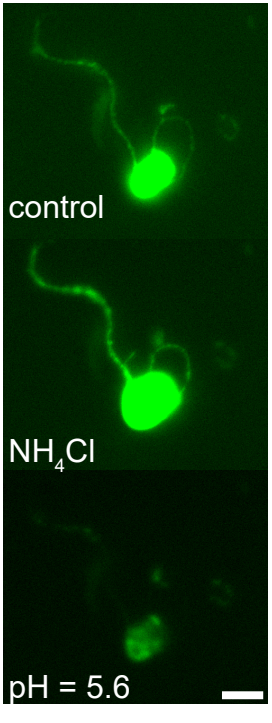

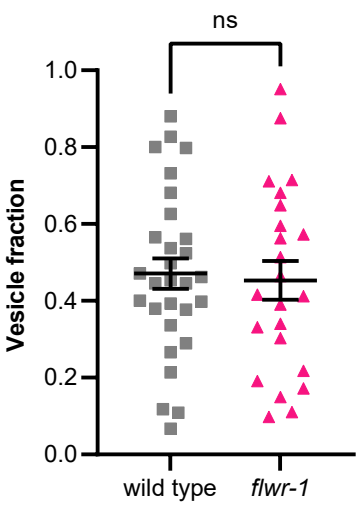

$$\text{Vesicle fraction} = \frac{F_{NH_4Cl} - F_0}{F_{NH_4Cl} - F_{pH = 5.6}}$$

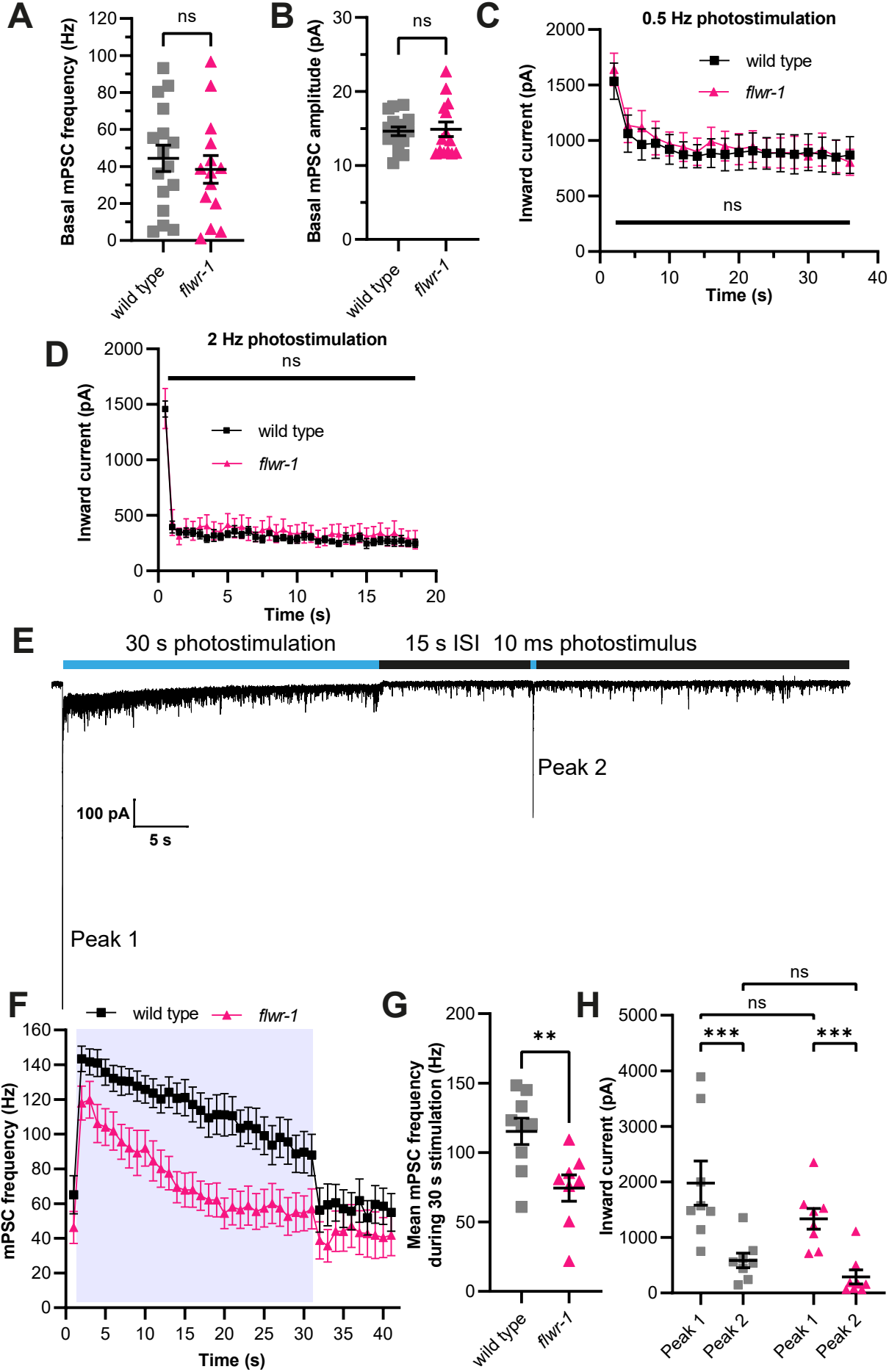
A
Basal mPSC frequency (Hz)
ns
wild type
flwr-1
B
Basal mPSC amplitude (pA)
ns
wild type
flwr-1
C
0.5 Hz photostimulation
Inward current (pA)
wild type
flwr-1
ns
Time (s)
D
2 Hz photostimulation
ns
Inward current (pA)
wild type
flwr-1
Time (s)
E
30 s photostimulation
15 s ISI
10 ms photostimulus
Peak 2
100 pA
5 s
Peak 1
F
wild type
flwr-1
mPSC frequency (Hz)
Time (s)
G
Mean mPSC frequency during 30 s stimulation (Hz)
**
wild type
flwr-1
H
ns
ns
***
***
Inward current (pA)
Peak 1
Peak 2
Peak 1
Peak 2

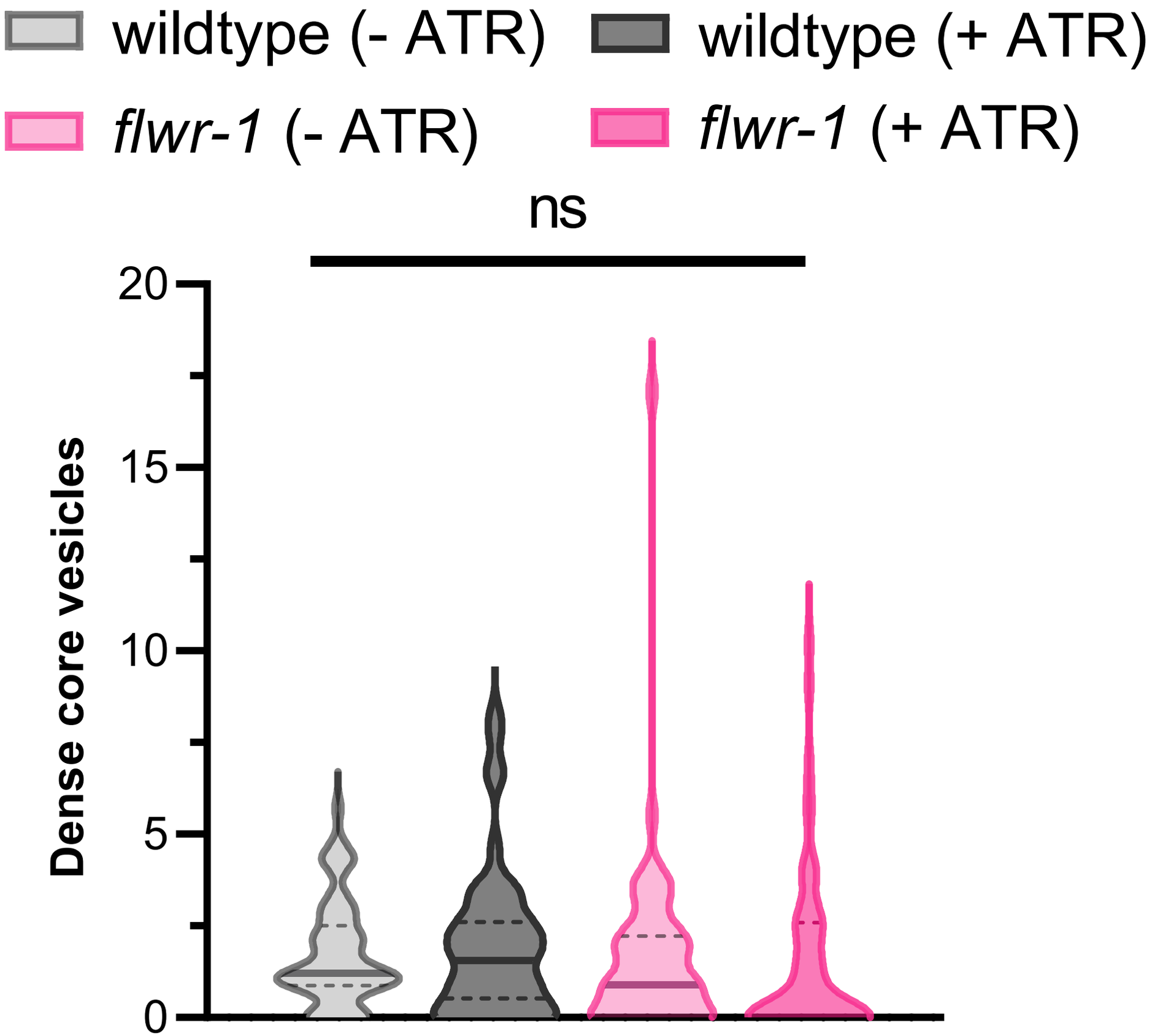
wildtype (- ATR)
wildtype (+ ATR)
flwr-1 (- ATR)
flwr-1 (+ ATR)
ns
Dense core vesicles
20
15
10
5
0

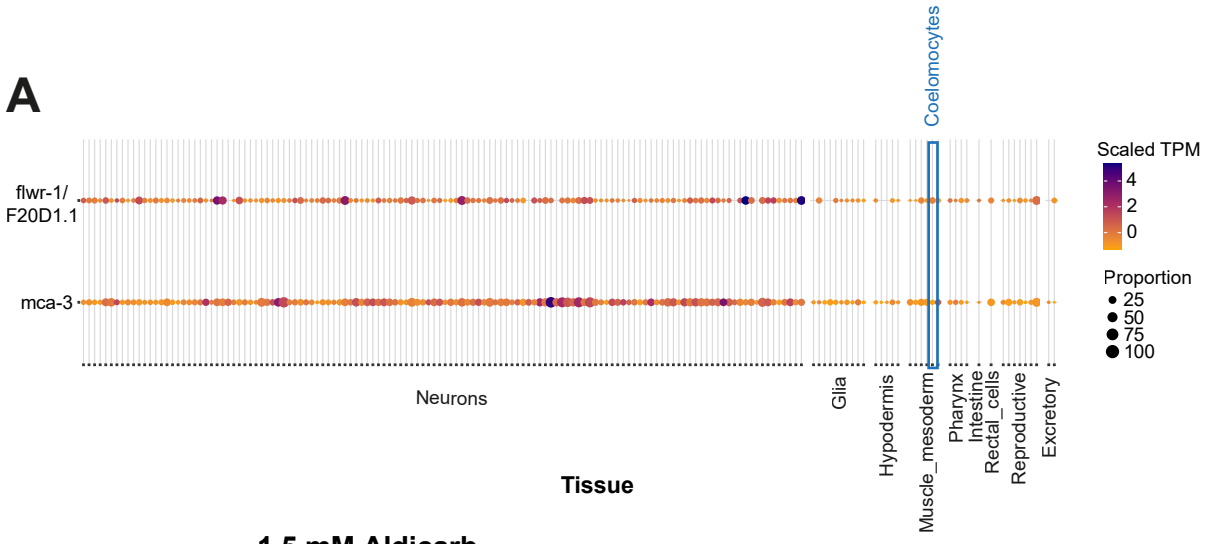
A
Coelomocytes
flwr-1/
F20D1.1
mca-3
Scaled TPM
4
2
0
Proportion
25
50
75
100
Neurons
Glia
Hypodermis
Muscle_mesoderm
Pharynx
Intestine
Rectal_cells
Reproductive
Excretory
Tissue

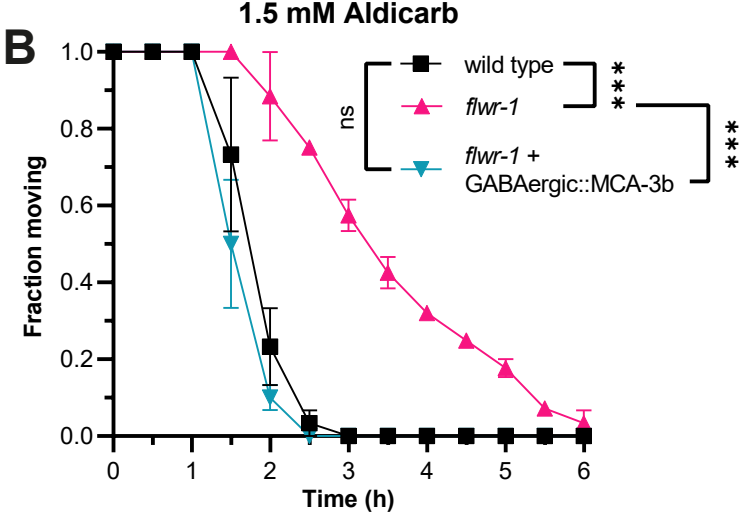
1.5 mM Aldicarb
B
wild type
flwr-1
flwr-1 +
GABAergic::MCA-3b
ns
***
***
Fraction moving
1.0
0.8
0.6
0.4
0.2
0.0
0
1
2
3
4
5
6
Time (h)

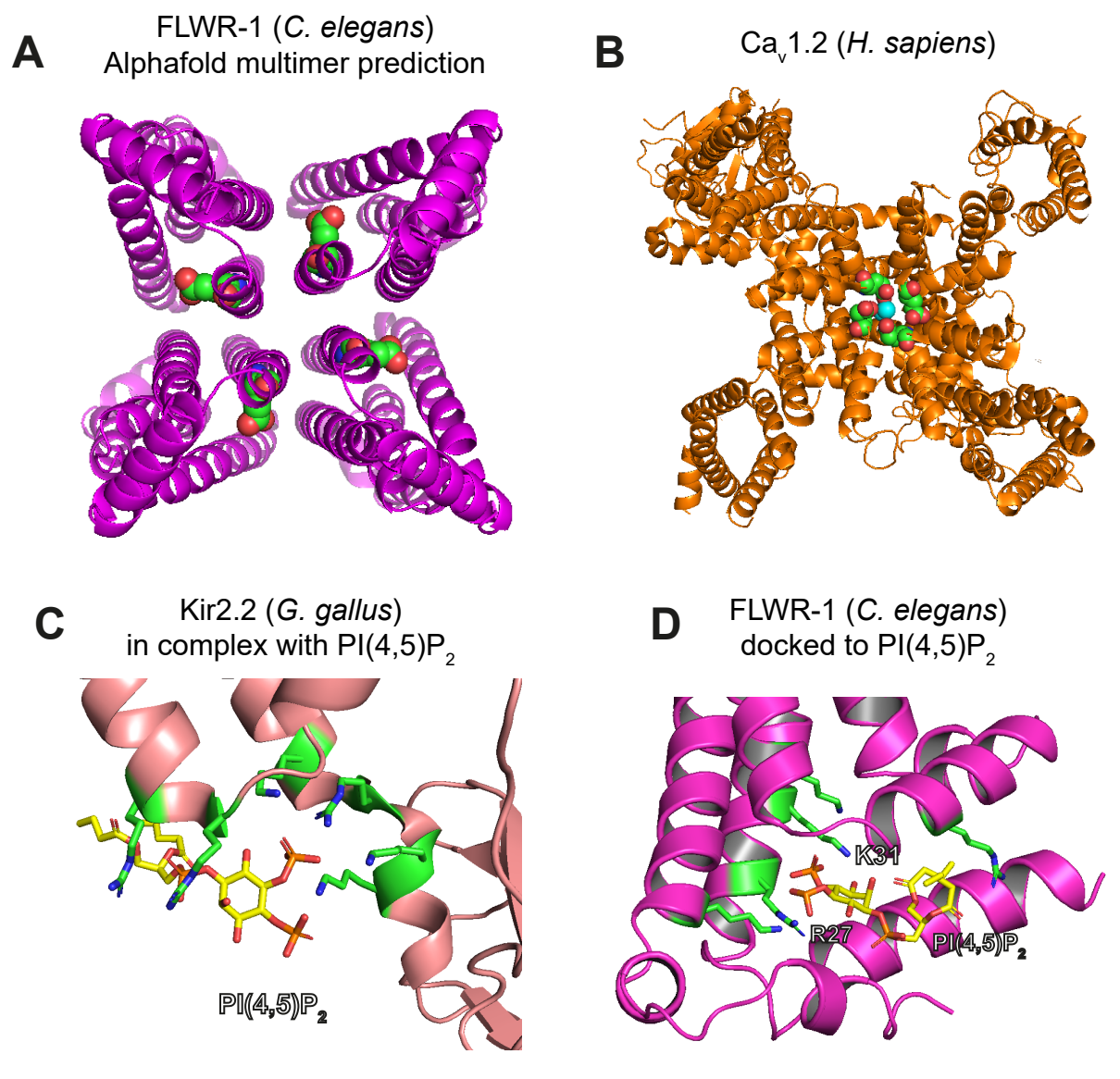
A
FLWR-1 (C. elegans)
Alphafold multimer prediction
B
Cav1.2 (H. sapiens)
C
Kir2.2 (G. gallus)
in complex with PI(4,5)P2
PI(4,5)P2
D
FLWR-1 (C. elegans)
docked to PI(4,5)P2
K31
R27
PI(4,5)P2

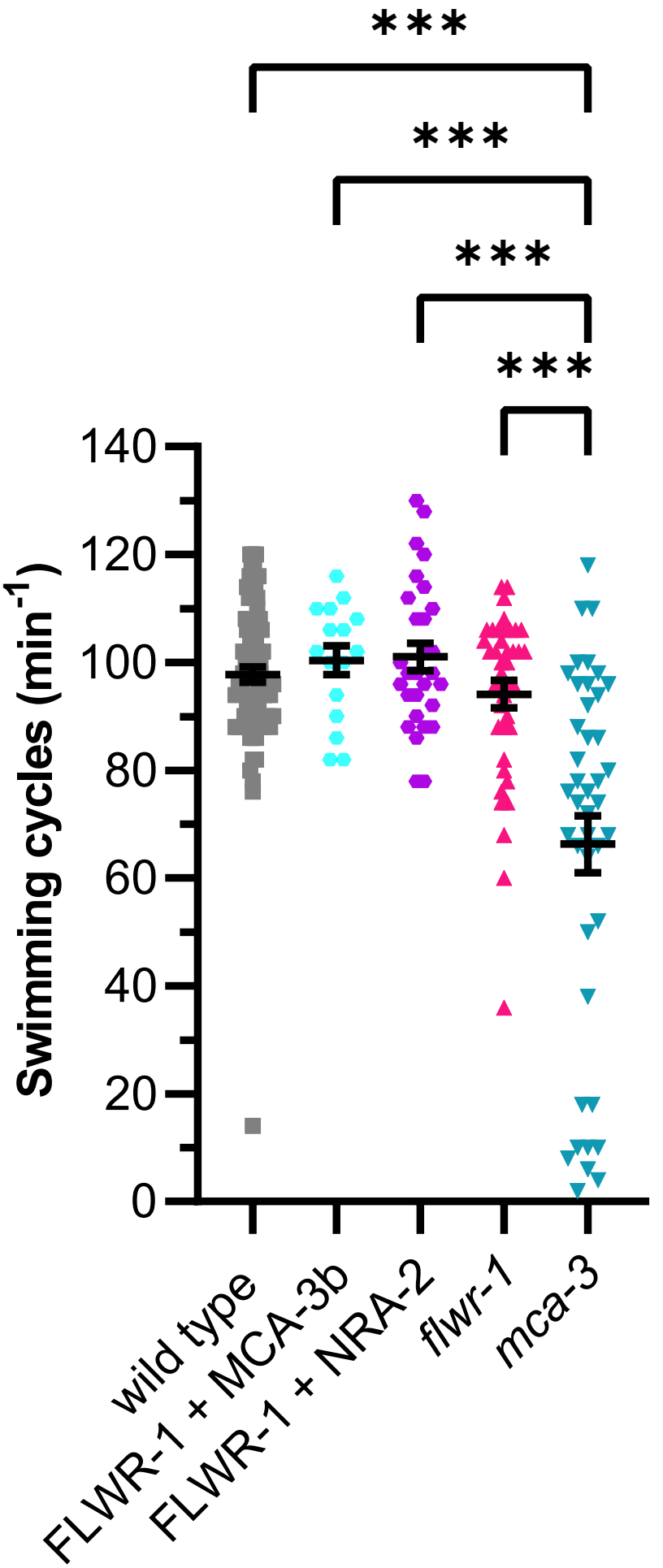
***
***
***
***
140
120
100
80
60
40
20
0
Swimming cycles (min-1)
wild type
FLWR-1 + MCA-3b
FLWR-1 + NRA-2
flwr-1
mca-3